1-1-2016

Investigation of the Role of the Nephila clavipes Major Ampullate Spidroin 1A N-Terminal Domain in Spider Silk Formation

James Hisao Atkison
Medical University of South Carolina

Recommended Citation

Atkison, James Hisao, "Investigation of the Role of the Nephila clavipes Major Ampullate Spidroin 1A N-Terminal Domain in Spider Silk Formation" (2016). *MUSC Theses and Dissertations*. 897.
https://medica-musc.researchcommons.org/theses/897

INVESTIGATION OF THE ROLE OF THE *NEPHILA CLAVIPES* MAJOR AMPULLATE SPIDROIN 1A N-TERMINAL DOMAIN IN SPIDER SILK FORMATION

James Hisao Atkison

A dissertation submitted to the faculty of the Medical University of South Carolina in partial fulfillment of the requirements for the degree of Doctor of Philosophy in the College of Graduate Studies.

Department of Biochemistry and Molecular Biology

2016

Approved by:
Chairman, Advisory Committee

[Shaun Olsen]

[Daniel Bearden]

[Joe Blumer]

[Christopher Davies]

[Tilman Heise]

ACKNOWLEDGEMENTS

Dr. Shaun Olsen	You took me into your lab as an orphaned graduate student, and I will always be grateful for everything that you have taught me. I know that I am a better scientist because of you.
Dr. Mirko Hennig and Dr. Daniella Ishimaru	You inspired me and provided valuable insight in the early development of this project
Katelyn Williams, Dr. Zongyang Lyu, Dr. Lingmin Yuan	Your help, ideas, and feedback have been priceless additions to the work I accomplished during my time in this lab
Dr. Christopher Davies, Dr. Stuart Parnham, Dr. Dan Bearden, Dr. Joe Blumer, Dr. Tilman Heise	Thank you for serving on my Dissertation Committee. I am grateful for all of guidance you have given me during the course of my time here at MUSC.
Mom, Dad, Cam, Aunt Kathy, Shaka, Kekoa, and Tuma	Thank you for all of your love, support, and patience. I would not be where I am today without all of you in my life. I love you!

TABLE OF CONTENTS

LIST OF TABLES

LIST OF FIGURES

KEY TO ABBREVIATIONS

Abbreviation	**Meaning**
MaSp	major ampullate spidroin
MiSp	minor ampullate spidroin
NTD	N-terminal domain
Rn	repeat region
CTD	C-terminal domain
^{Nc}NTD	*Nephila clavipes* major ampullate spidroin 1A NTD
^{Ea}NTD	*Euprosthenops australis* major ampullate spidroin 1 NTD

ABSTRACT

Spider dragline silk is a naturally occurring polymer that has the potential to be used in many biomaterials such as skin graft scaffolds and cartilage repair matrices due to its elasticity, high tensile strength, and biocompatibility. However, natural large scale production of spider silk is unfeasible due to the cannibalistic nature of spiders in captivity. A viable alternative is artificial silk production, which requires an understanding of the in vivo mechanisms spiders use to spin silk. The conversion of highly concentrated proteins, called spidroins, into insoluble fibers requires the dimerization of the spidroin N-terminal domain (NTD). This process is regulated by decreases in both salt concentration and pH; however, the specific mechanisms involved are still not completely known. To gain a more detailed understanding of these processes, I solved the crystal structure of the *Nephila clavipes* major ampullate spidroin 1A (^{Nc}NTD). The structure contains unique intermolecular contacts including key salt bridges that grant a degree of plasticity at the dimer interface. Additionally, I observed a novel intramolecular handshake interaction between highly conserved acidic residues D17 and D53. Interestingly, the D17A mutant favored dimer formation of the NTD; thus, I also solved its crystal structure for comparison with wild type. Additionally, I used NMR-based experiments to probe the dynamics of the ^{Nc}NTD in solution. While these experiments are not yet fully complete, they reveal interesting information regarding differences in the monomer-to-dimer transition between the WT and D17A mutant. Based on these analyses, I propose that the presence or absence of the D17-D53 handshake alters the topology of the NTD monomer subunit, which increases the

heterogeneity of the possible conformers the NTD subunits can adopt. This variability contributes to the model of conformational selectivity, in which the NTD subunits populate many conformations that are in dynamic equilibrium and dimerize when a monomer subunit selects a partner with the complementary binding interface. The intermolecular salt bridges at either end of the dimer interface serve to properly align the subunits, and the plasticity they impart allows for the various combinations of subunit pairs to form dimers. This dissertation contributes to the understanding of the detailed mechanisms that govern the spidroin NTD dimerization process that is critical to spider silk formation.

Chapter 1: Background

Introduction

Spider silk is a naturally occurring polymer that has high elasticity, high tensile strength, and biodegradable nature (Vollrath and Knight 2001, Kubik 2002). These characteristics make spider silk a desirable component in the design of many biomedical applications. However, there are many challenges in the large-scale production of usable quantities of both natural and synthetic silks. To overcome these challenges, a deeper understanding of the *in vivo* mechanisms that control the production of spider silk is necessary. The data presented in this dissertation focus on a key component of spider silk and contribute to the understanding of the role it plays in the silk spinning process.

Spider Silk in Biomedical Applications

Spider Silk as a Biomaterial

Humans long ago recognized the amazing potential of spider silk. It has been used for sutures and wound healing for centuries (Newman and Newman 1995), and silks have even been incorporated into body armor as early as 1200 AD (Turnbull 2003). More recently, biomedical applications for spider silk include skin grafts (Wendt, Hillmer et al. 2011), neuron regeneration (Allmeling, Jokuszies et al. 2008), and cartilage repair (Gellynck, Verdonk et al. 2008), among many others.

The skin is one of the most important organs in the human body, as it provides the first line of defense against infection (Madison 2003). However, injuries to the skin are very common, including cuts and burns (Sen, Gordillo et al. 2009). According to the American Burn Association, there are 486,000 burn victims per year receiving medical treatment in the United States (Krichbaum 2016). The most common treatment for skin burns is to receive skin grafts designed to repair the affected area, and there is a growing demand for novel materials to provide more effective methods of skin repair. Recently, grafts that incorporate spider silk into the material design have been developed. Wendt et al. have used spider silk woven across a steel scaffold for seeding fibroblasts and keratinocytes. The spider silk provides a proteinaceous matrix to allow the cells to grow and proliferate, and multiple layers of silk matrix can provide the desired growth conditions to optimize cell viability. In this manner, large areas of skin can be "grown" to be used to treat burn victims. The keratinocytes can be harvested from unaffected areas of the patient's body to reduce the risk of rejection upon implantation of the new spider silk-matrix skin, and the silk eventually degrades to leave newly grown tissue in the injured area (Wendt, Hillmer et al. 2011).

Spider silk has also been used in neuron regeneration. Peripheral neuron ligation due to injury is more common than spinal cord injury (Chen, Zhang et al. 2006), and the consequences of these injuries include decreased functionality of the limbs affected, long-term disability, and decreased standard of living. Current methods of axonal repair are limited to short distances and the use of autologous nerve grafts; these factors severely lower the effectiveness of neuron repair and the likelihood of regaining full function. Thus, new options for aiding neuron regeneration are in demand, especially those that incorporate readily-available, biocompatible materials. These materials must be able to promote migration of the supporting Schwann cells (critical to neuron health and activity) (Nectow, Marra et al. 2012), and synthetic materials of this nature include micropatterned poly(d,l-lactic acid) films (Miller, Jeftinija et al. 2002) and polydioxanone filaments (Shen, Berger et al. 2001). However, these synthetic materials increase the risk of immune rejection, prompting the need for more biocompatible fibers. One such biomaterial is spider dragline silk, which lacks sericin glue-like proteins and therefore, decreases immune response upon implantation (Altman, Diaz et al. 2003). Allmeling et al. used spider silk fibers as guidelines for neuron regeneration in rats. The sciatic nerve was ligated, and spider silk fibers were compared with established isogenic nerve grafts for neuron regeneration, Schwann cell proliferation, and functionality of the affected muscle. Their results indicated that spider silk provided a viable guide for Schwann cell migration and a suitable long-distance model for axonal re-growth (Allmeling, Jokuszies et al. 2008).

Over 10% of knee and other joint medical problems are a result of significant cartilage injury (Arøen, Løken et al. 2004). However, joint cartilage has historically shown a limited ability to self-repair (Buckwalter and Mankin 1998). As such, development of new tissue engineering strategies could provide the necessary avenue for alleviating these issues. Chondrocytes are responsible for cartilage repair, but they rely on a specific set of conditions for proper function (Ferruzzi, Calderoni et al. 2004). Replicating these *in vivo* conditions is critical to initiating proper cartilage repair, but several challenges have arisen. Synthetic materials such as polyglycolic acid (PGA) and polylactic acid (PLA) have been used as matrices for seeding autologous chondrocytes; however, the chondrocytes tend to dedifferentiate prior to full cartilage repair due to lack of appropriate growth factors (Ma, Gao et al. 2005). Modifying these matrices to incorporate these growth factors often leads to premature biodegradation upon implantation (Moran, Pazzano et al. 2003). Thus, biomaterials that satisfy these stringent demands are highly sought after; spider silk is one such material that has proven to be useful in these applications as it has a relatively slow degradation rate (Horan, Antle et al. 2005). Gellynck et al. created scaffolds using native *Bombyx mori* (silk worm) and *Araneus diadematus* (European garden spider) to compare the properties of these silks to synthetic scaffolds. The porosity, shape, and compression of the scaffolds could be controlled by salt-leaching the silk scaffolds and the chondrocytes were able to successfully adhere and proliferate to the point of displaying the typical physical markers of cartilage cells. It is believed that silk-based scaffolds will prove to be even more effective than current methods for stimulating and regulating cartilage repair (Gellynck, Verdonk et al. 2008).

In summary, spider silks possess remarkable qualities, including extreme strength, elasticity, and contractility, and they are also biodegradable and biocompatible due to their chemical composition. This combination of desirable physical and biochemical properties has made spider silk the target of many studies aimed at harvesting this natural polymer for biomedical uses. However, the transition from prey-catching webs to novel biomaterials is not without several hurdles.

Challenges of Large Scale Silk Production

There are two main challenges with regards to using silk for industrial-level biomaterial applications. First, there is the issue of quantity. The studies mentioned above all relied on natively harvested spider silk for testing its suitability in the described biomaterial applications. While the specific methods vary, the general principal involves stimulating a captured spider to spin silk, which is usually collected on a rotor or netting (Allmeling, Jokuszies et al. 2008, Gaines and Marcotte 2008, Gellynck, Verdonk et al. 2008), as shown in Figure 1.1. Native silk is appropriate for testing and development purposes but is ill-suited for obtaining the quantities of silk needed for industrial-level production. Unfortunately, each individual spider does not produce large enough quantities of silk, and spider “farms” are difficult to maintain due to the cannibalistic nature of many species of spider kept in close captivity (Knight and Vollrath 1999).

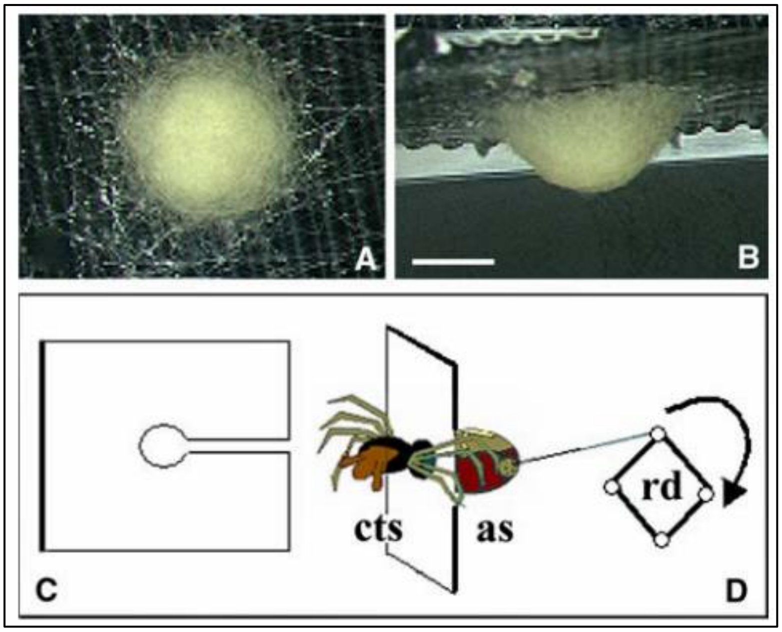

Figure 1.1, Harvesting natural spider silk. Front (a) and side (b) view (scale bar 1 cm) of *Araneus diadematus* spider egg sac attached on corrugated cardboard. (c) Pillory-like plastic construct used to keep the spider legs away from the abdomen and spinnerets during dragline reeling. (d) Side view of cephalothorax-side (cts) and abdomen-side (as) plus reeling device (rd). The reeling device rotates to collect newly spun silk from the spider. Image taken from Gellynck et al. 2008 (Gellynck, Verdonk et al. 2008).

The second challenge in large scale silk production involves the composition of the silk itself. Native spider silk can vary in its consistency with regards to fiber composition and modification. As will be discussed below, spider silks are made up of proteins, glycoproteins, lipids, and other components (Sponner, Vater et al. 2007). This complexity imparts a degree of variability that will most likely not be consistent enough for industrial standards (Madsen, Shao et al. 1999); the uniformity of implantable materials derived from native spider silk will be much lower compared to those manufactured in a more regulated manner.

Large-scale Production of Spider Silks for Biomaterials Applications

A variety of strategies have been developed to address the aforementioned challenges. Small portions of the spider silk proteins (termed spidroins) can be expressed and purified recombinantly using bacteria (Askarieh, Hedhammar et al. 2010, Gaines, Sehorn et al. 2010, Kronqvist, Otikovs et al. 2014). However, full-length spidroins are much larger and contain multiple domains and repeat regions (to be discussed below), which prevents them from being properly synthesized in *E. coli* (Baneyx and Mujacic 2004). These repeat regions are very glycine and alanine rich, which leads to rapid depletion of the corresponding tRNAs for these residues in cell expression systems. Attempts at synthesizing the full length proteins have resulted in deletions or mutations (Fahnestock SR 1997), but this issue has been partially resolved by over-expressing the tRNAs for the Gly codons through the over-expression of a Gly biosynthesis gene (Xia, Qian et al. 2010).

The optimized cell expression systems described above are not sufficient for producing the mass quantities of silk needed for biomedical applications. Thus, other methods of recombinant protein expression have been explored. For example, the mammary glands of goats have been shown to be excellent bioreactors, and transgenic goats can be generated to recombinantly express large proteins, including those with post-translational modifications. The proteins of interest are produced in the goats' milk, which can be harvested daily, and from which large quantities can be purified easily (Moura, Melo et al. 2011). Alternatively, there has been an increased emphasis on producing pharmaceutical-grade proteins in bulk quantities using genetically modified plants. Large fields of these plants can be grown quickly and relatively cheaply, and the protein of interest is purified from the leaves (Fuqua, Hamorsky et al. 2015). Recently, spider silk-like proteins were recombinantly expressed in transgenic tobacco plants (Peng, Russo et al. 2016). These methods could provide an avenue for similar large-scale production of the full-length spider proteins.

Regardless of the manner of its synthesis, it is important to understand the molecular mechanisms that impart the desirable properties of spider silk. The ability to replicate the processes of silk synthesis for biomedical use relies on understanding the contributions of two interconnected factors: (1) the physiology of the spider's silk glands and spinning ducts and (2) the structure of the individual components of spider silk. Each of these factors will be discussed below, with emphasis on the structural features of spider silk.

Overview of the Silk Spinning Process

Key Features of Spider Silk Production Physiology

Detailed dissections of the silk production glands, ducts, and spinning organs have contributed to the overall understanding of the silk formation process. Several biological studies have focused on the dragline silk production pathway of the *N. clavipes* spider (Xu and Lewis 1990, Vollrath and Knight 1999, Knight and Vollrath 2001, Vollrath and Knight 2001). Dragline silk is derived from the major ampullate gland and almost completely comprised of proteins, termed major ampullate spidroins (MaSp) (Lewis 2006). The journey of these spidroins from synthesis to maturation and use in web construction is representative of the general silk production process (Knight and Vollrath 1999).

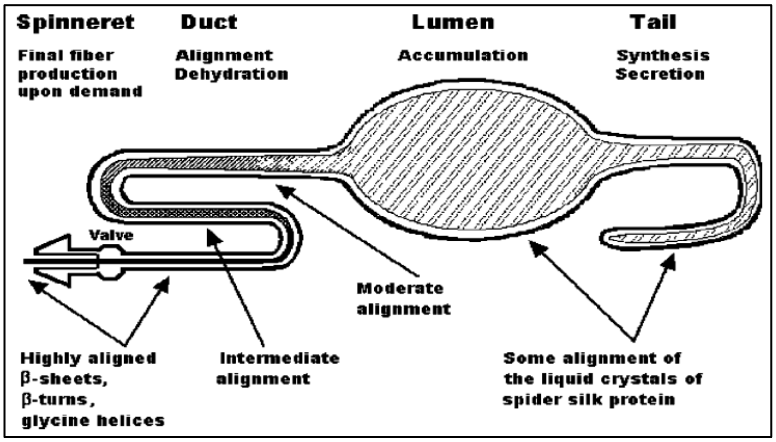

Figure 1.2, General anatomy of the major ampullate gland. The major ampullate gland consists of the tail (for spidroin synthesis and secretion), lumen (for spidroin accumulation and storage), and duct (for spidroin alignment and maturation into fiber). The spinneret connects the gland to the exterior of the spider and draws the silk out of

the gland for use in web construction. The general structure of the spidroins is indicated below each section of the pathway. Image taken from Lewis 2006 (Lewis 2006).

The major ampullate gland is divided into three compartments: the tail, the ampulle (or lumen), and the duct (Vollrath and Knight 1999, Knight and Vollrath 2001, Lewis 2006, Andersson, Holm et al. 2013), as shown in Figure 1.2, and the glands are present in pairs within the spider (Adrianos, Teulé et al. 2013). Spidroins are primarily synthesized in the tail region (Bell and Peakall 1969, Sponner, Schlott et al. 2005), which contains specialized epithelial cells with extensive endoplasmic reticulum to accommodate the burden of robust protein production (Knight and Vollrath 2001, Casem, Tran et al. 2002).

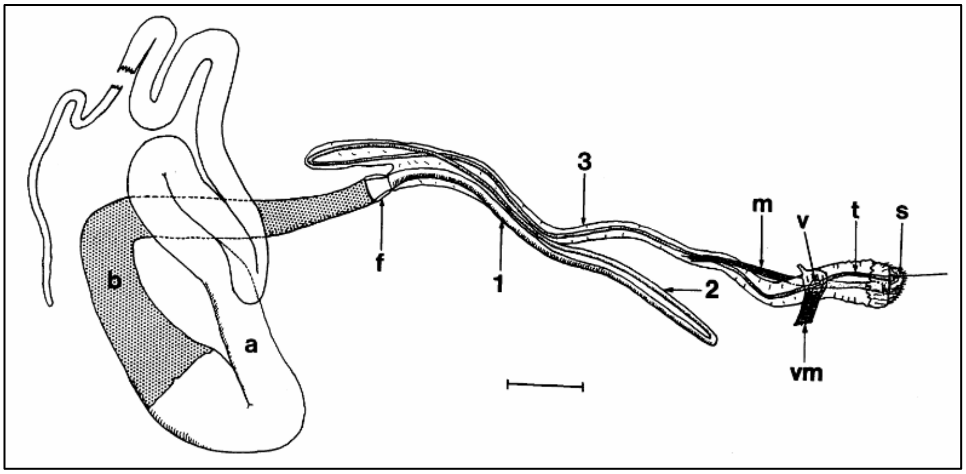

Figure 1.3, Detailed anatomy of the spinning duct of the spider *Nephila edulis*. Drawing of the major ampullate gland and associated duct (scale bar 1 mm) containing Zone A (a), Zone B (b), funnel (f), limbs of duct 1, 2, 3, muscle (m), valve (v), valve muscle (vm), terminal tubule (t), and spigot (s). Image taken from Knight and Vollrath 2001 (Knight and Vollrath 2001).

The ampulle, which is primarily used for storage of newly synthesized spidroins prior to spinning, is divided into the A and B zones (Figure 1.3). Analysis of the A-zone revealed the presence of droplets containing freshly synthesized spidroins surrounded by a solution of water and various salt ions, and this mixture is collectively termed the spinning dope. The spidroins are stored at extremely high concentrations around 30-50% (w/v) (Chen, Knight et al. 2002), but there is some disagreement about both the secondary and tertiary structures that stored spidroins assume. Spidroins harvested directly from the ampullate gland were examined using circular dichroism (CD) and observed to contain α-helices, β-turns, and β-sheets (Dicko, Knight et al. 2004), while nuclear magnetic resonance (NMR) studies of the spinning dope revealed mostly random coils with some α-helical regions (Hijirida, Do et al. 1996). These discrepancies in secondary structure could be explained by how the dope was extracted (from the A or B zone) and/or storage conditions. Thus, Lefevre et al. performed *in situ* Raman spectromicroscopy on ampullate gland material, which revealed mostly unfolded protein with some α-helices (Lefèvre, Leclerc et al. 2007). As this finding is in agreement with most other studies of pre-spun spidroins, it is generally accepted that they are mostly disordered at this stage.

The pre-spun dope droplets increase in size as they coalesce together on their journey through the B-zone (Vollrath and Knight 1999, Sponner, Vater et al. 2007). The ampulle feeds into funnel region of the duct, which rapidly decreases the diameter of the lumen (from approximately 120 µm to less than 10 µm) (Knight and Vollrath 1999). The tapered geometry of the spinning duct increases the flow velocity of the spinning dope and causes the individual droplets to elongate and approach the shape of the mature fiber as they are forced down the ever narrowing first, second, and third limbs (Lefèvre, Leclerc et al. 2007). Additionally, it has been found that the viscosity of the spinning dope decreases as the shear forces acting upon it increase, which is known as 'shear-thinning' (Chen, Knight et al. 2002). The thin lining of the limbs is thought to act as a dialysis membrane, with a decrease in water and sodium chloride concentration and an increase in a surfactant thought to act as a lubricant to prevent fiber damage from the increased shear forces (Vollrath and Knight 2001). The decrease in sodium chloride concentration has been shown to be particularly important for fiber formation (Gaines, Sehorn et al. 2010, Gronau, Qin et al. 2013) and will be discussed below.

Perhaps most importantly, the spidroins experience a decrease in pH during their journey down the spinning duct. Proton pumps in the epithelium of the limb regions (Andersson, Chen et al. 2014) are thought to facilitate the decrease in pH from 7.2 in the ampullate gland to 6.3 in the middle of the spinning duct (Dicko, Vollrath et al. 2004) to below 5.7 near the end of the duct (Andersson, Chen et al. 2014). The effects of this pH decrease will be discussed in detail below, as this aspect of the spinning process is the underlying force driving the mechanisms discussed in this dissertation. As the maturing fiber reaches the exit of the spinning duct, the spidroins receive glycoprotein and lipid coatings (described below) (Schulz 2001). Finally, the mature fibers are drawn out of the final duct through the spigot by spinnerets and used for web construction or as the dragline (Vollrath and Knight 1999).

In summary, major ampullate gland anatomy reveals mechanisms by which nascent spidroins experience decreases in pH and salt concentration and an increase in shear force, which act together to spin the spidroins into mature, usable silk. These general aspects of the silk spinning process are well-characterized, but their effects on the specific molecular mechanisms involved in silk production are less understood. Thus, analysis of the structural components of spidroins is crucial to furthering the detailed understanding of silk synthesis.

Types of Spider Silk

Spider silk is the target for all of the aforementioned biomaterial applications due to the key physical and biochemical properties it possesses. Up to this point, the term "spider silk" has been used as a catch-all term for the many different types of silk that spiders can produce. The types of webs spun by each species of spider vary, but many of the same structural motifs are conserved (Vollrath 2000). All spiders have a variety of glands responsible for producing silk with specific properties (Figure 1.4) and these silks display a wide range of physical and biochemical properties (Gosline JM 1999).

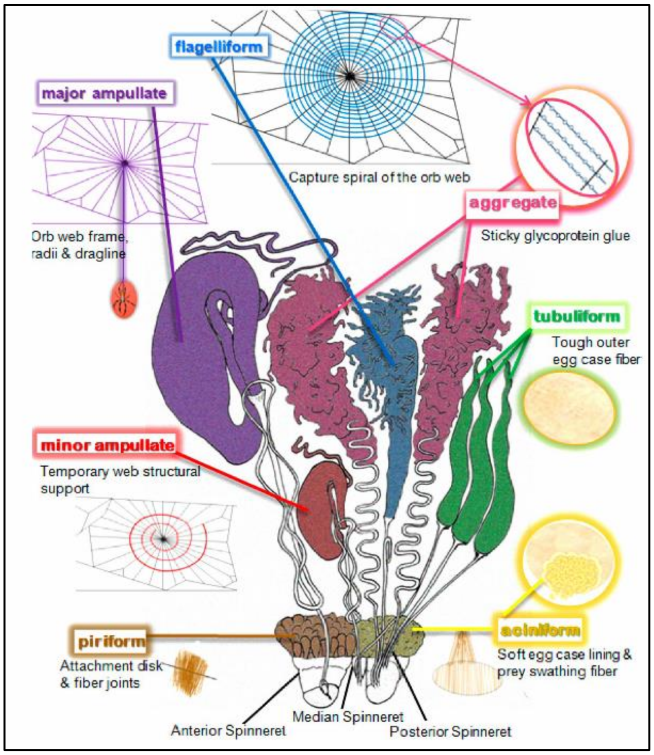

Figure 1.4, Abdominal silk glands and silks of *Nephila clavipes*. One half of the bilateral pair of the abdominal spider silk glands of *Nephila clavipes* are shown attached via detailed ductwork to their corresponding spinnerets. Pictorial representations of the gland products are illustrated in the margins. Image taken from Adrianos et. al. 2013 (Adrianos, Teulé et al. 2013).

The abdominal silk glands of the *Nephila clavipes* spider have been dissected and characterized based on the type silk they each produce (Adrianos, Teulé et al. 2013). For example, when an insect flies into a spider's web, it is trapped by the capture spiral, which consists of silk made from the flagelliform gland. The adhesiveness stems from specific glycoproteins that coat the main protein core (Sponner, Schlott et al. 2005). Spiders use dragline silk, which is formed in the major ampullate gland, for the web frame and general-purpose anchoring (Adrianos, Teulé et al. 2013). This type of silk has a tensile strength of 1.1 GPa, which is comparable to steel wire (1.3 GPa) (Vincent 1982); however, it is 1.3 times less dense, and therefore, a stronger material by weight (Vollrath 2000). Interestingly, as shown Figure 1.5, the dragline silks from various spider species have demonstrated diverse levels of elasticity, contractility, and tensile strength, most likely due to differences in their chemical composition (Madsen, Shao et al. 1999). Dragline silk is one of the strongest types of silk (Gosline JM 1999) and is therefore the focus of most spider silk studies, including this one.

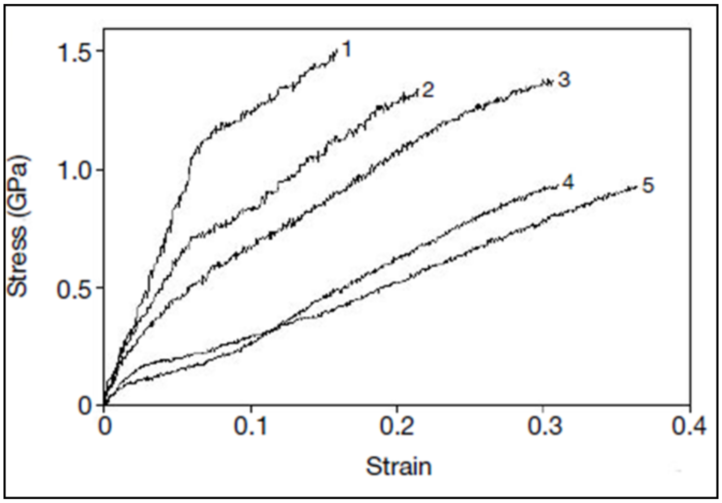

Figure 1.5, Stress-strain characteristics of dragline silk reeled from different web building spiders. Stress-strain curves for *Euprosthenop*s *australis* (Pisauridae) (1), *Cyrtophora citricola* (Araneidae) (2), *Latrodectus mactans* (Theridiidae) (3), *Araneus diadematus* (Araneidae) (4) and *Nephila edulis* (Tetragnathidae) (5). The data were collected under comparable conditions by artificial reeling. They show that the silk of *Euprosthenops* (1) is stiffer and requires more force to break it but is much less elastic and thus takes up less energy than the comparable silk of *Nephila* (5); the characteristics of the other species lie in between. Image taken from Vollrath and Knight 2001 (Vollrath and Knight 2001).

Layered Components of Dragline Silk

Analysis of natively harvested dragline silk has revealed it to contain several layers, each of which serve a distinct purpose. As shown in Figure 1.6, the inner-most layers consist of two cores of proteins, termed major ampullate spidroins (MaSp) (Xu and Lewis 1990). These will be discussed in great detail below, and their synthesis and organization are the major aspects of silk production. This protein layer is surrounded by a rigid skin layer composed of unknown high molecular weight proteins (Sponner, Vater et al. 2007). The skin is the most rigid layer and displays a high degree of molecular orientation within the silk fiber (Rousseau, Hernández Cruz et al. 2007), but its function is unknown.

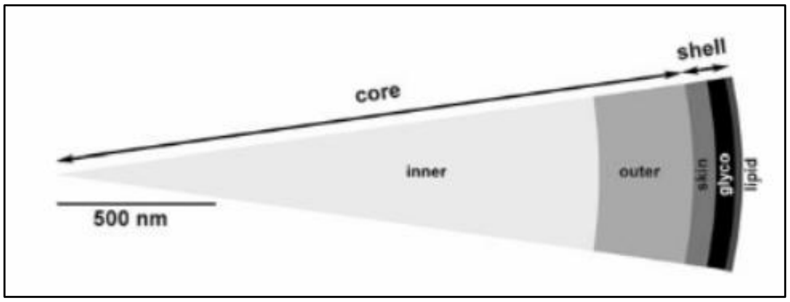

Figure 1.6, Model of the multilayer organization of dragline silk. Dragline silk can be divided into a shell and ore with five major layers of different material composite (from interior to exterior): inner core, outer core, skin, glyco coat, and lipid coat. The approximate relative thicknesses of each layer are indicated. Image taken from Sponner et al. 2007 (Sponner, Vater et al. 2007).

A protective shell, composed of a glycoprotein layer and lipid coating, surrounds the protein core and skin layer. Surrounding the skin layer is the glycoprotein layer, which is suspected to provide anti-microbial resistance to the silk and also may be involved in maintaining proper water balance in the protein core (Römer and Scheibel 2008). The glycoprotein layer is surrounded by a lipid coating. This layer is composed of a variety of branched lipids and is thought to repel water and/or to provide a smooth surface to aid in the rapid fiber spinning process (Schulz 2001). Additionally, the lipid coating is thought to carry specific sex pheromones important for mating (Gaskett 2007, Scott, McCann et al. 2015). Compared to the protein core, the shell is relatively thin and is not suspected to contribute to the mechanical strength of the fiber (Augsten, Mühlig et al. 2000).

In addition to the protein core and shell layers described above, water is a major component of spider silk. Water composes over 66% of the stored spidroin solution in the ampullate gland and 20% of the newly spun fiber’s mass (Chen, Knight et al. 2002). Harvested silk fibers undergo ‘super-contraction’ when submerged in water, in which fiber length can shrink by as much as 40%. Thus, the decrease in water composition from the storage gland to the mature fiber is likely a mechanism by which large amounts of silk can be stored in the supercontracted form before being elongated during the spinning process (Eles and Michal 2004, Li, Eles et al. 2009).

The main components of the fiber (protein core, protective shell, and water content) have been well established and are intrinsically linked to the functions of spider silk. As mentioned above, formation and organization of the silk's protein core are critical parts of the silk spinning process, and these proteins provide the desirable mechanical and biochemical properties of the silk. Thus, analysis of the individual elements that comprise the spidroins of the core is necessary for accurate replication of the complex *in vivo* mechanisms on an industrial scale.

Major Ampullate Spidroin Structural Elements

Major Ampullate Spidroins

As mentioned above, dragline silk is one of the strongest of types of silk (Madsen, Shao et al. 1999), and it consists mainly of major ampullate spidroins. Typically, spiders produce two forms of MaSp (1 and 2) (Xu and Lewis 1990), but the ratio of MaSp1 to MaSp2 varies from spider to spider (Sponner, Schlott et al. 2005). For example, in *Nephila clavipes* (commonly known as the golden orb-weaver), the estimated ratio is 81% MaSp1 and 19% MaSp2 (Brooks, Steinkraus et al. 2005), while in *Latrodectus hesperus* (western black widow), the estimated ratio is 71% MaSp1 and 29% MaSp2 (Ayoub and Hayashi 2008). MaSp2 typically has higher proline content than MaSp1, which causes it to be more elastic due to a higher β-turn frequency conferred by this residue (Liu, Shao et al. 2008, Liu, Sponner et al. 2008). Thus, the ratio of MaSp1 to MaSp2 has a direct effect on the physical properties of the dragline silk. The two types of major ampullate spidroin are otherwise very similar (Gaines, Sehorn et al. 2010) and both contain the same general domain architecture: highly conserved N-terminal and C-terminal domains (NTD and CTD, respectively) that flank a middle region of repeating motifs. Each of these domains imparts a specific function for the spidroin (Figure 1.7), and will be discussed below.

Figure 1.7, General major ampullate spidroin domain architecture. Major ampullate spidroins consist of an N-terminal domain (NTD, blue circle), repeat region (Rn, green blocks), and C-terminal domain (CTD, red triangle). In this figure, the relative sizes of each domain are increased (for the NTD and CTD) or decreased (for the repeat region) for clarity. For the spidroins studied, the repeat region is ~100 times larger than either terminal domain.

MaSp Repeat Region Structure and Function

The repeat region (Rn) consists of 3000-4000 residues organized into 30-40 residue-long, conserved repeating blocks. These blocks contain two main patterns: short, glycine rich regions (GGX motifs, where X could be A, Q, or Y) followed by stretches of multiple alanines (poly-A) (Gatesy, Hayashi et al. 2001). X-ray diffraction and NMR analysis of naturally harvested silk reveal that the GGX motifs are hydrophilic and impart α-helix secondary structure, while the hydrophobic poly-A structures form β-sheets and provide the high tensile strength of the fiber (Simmons, Michal et al. 1996, Parkhe, Seeley et al. 1997); the importance of these secondary structure motifs will be discussed below. As shown in Figure 1.8, in the spinning duct, multiple strands are arranged parallel to each other, further adding to the strength of the silk (van Beek, Hess et al. 2002).

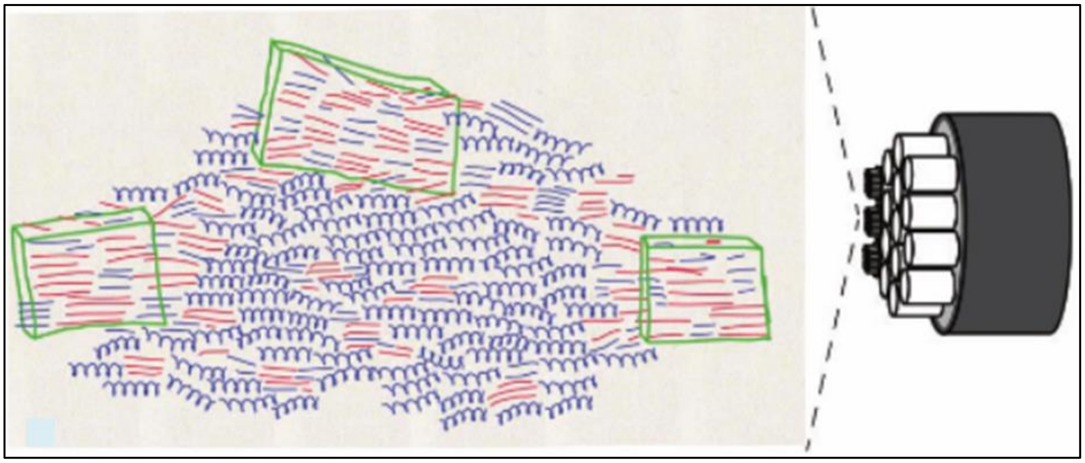

Figure 1.8, Proposed model for spider dragline silk. The molecular structure consists of β-sheet regions, containing alanine (red lines) and glycine (blue lines), interleafed with predominantly α-helical parts (blue curls), which do not contain alanine. The green boxes indicate domains identified as crystalline. Multiple individual strands are arranged parallel to each other (white cylinders) within the fiber (gray cylinder). Image adapted from van Beek et al. 2002 (van Beek, Hess et al. 2002).

Several studies have investigated the effects of the established *in vivo* mechanisms of increased shear forces and decreased salt concentration and pH have on recombinantly expressed miniature versions of the Rn. Protein constructs of shortened versions of the Rn from the *Euprosthenops australis* MaSp1 and from *Araneus diadematus* ADF3 and ADF4 (homologous to MaSp1 and MaSp2) irreversibly assemble into aggregates after exposing the protein to shear forces (either by shaking or rotating the solutions for extended periods of time). CD spectra from before and after the shear force treatment revealed that the secondary structures of the aggregates transformed from being α-helix rich to predominantly β-sheets. This result was confirmed by Fourier Transform Infrared Spectroscopy (FTIR) on the aggregates after the shear forces were applied (Dicko, Knight et al. 2004, Exler, Hümmerich et al. 2007, Stark, Grip et al. 2007, Askarieh, Hedhammar et al. 2010, Eisoldt, Hardy et al. 2010, Hagn, Eisoldt et al. 2010). These observations agree with those of naturally harvested spider silks, which show that pre-spun spidroins taken from the proximal limbs of the spinning duct contain mostly α-helices, while spidroins taken from the distal part of the duct, as well as mature fibers, are β-sheet rich (Xu and Lewis 1990, Gosline JM 1999, Sponner, Schlott et al. 2005, Hedhammar, Rising et al. 2008, Liu, Sponner et al. 2008, Adrianos, Teulé et al. 2013). Thus, it was concluded that shear forces act to strain the α-helices and disrupt the hydrogen bonds that order the secondary structure of the Rn. This action promotes a more extended conformation in which β-sheets can form (Berg J 2002). Reversion to α-helix would be unlikely since β-sheets are more thermodynamically stable (Kenney, Knight et al. 2002).

The effects of salt concentration and pH on the repeat region are less understood. Recombinantly expressed Rn constructs aggregated in the presence of 200-300 mM potassium phosphate, but the aggregation took over 1 hour (Eisoldt, Hardy et al. 2010, Hagn, Eisoldt et al. 2010). While the exact phosphate concentrations in the spinning duct are unknown, they are probably less than 300 mM (Knight and Vollrath 2001). Additionally, the spidroins pass through the regions of the spinning duct in a matter of seconds (Vollrath and Knight 1999); thus, the observed effects of salt concentration on Rn aggregation are most likely not physiologically relevant. Similarly, the repeat regions are relatively unaltered by changes in pH. Repeat region constructs from both *N. clavipes* and *E. australis* MaSp1s displayed minimal alteration in secondary or tertiary structure in the pH range 4 to 8, which includes the pH range measured in the spinning duct (Fahnestock SR 1997, Hedhammar, Rising et al. 2008). Together, these studies suggest that *in vivo*, the decreases in salt concentration and pH have little effect on the Rn. Instead, as will be discussed below, these forces exert their effects on the terminal regions of the spidroins. While the repeat region contains the bulk of the spidroin and contributes the aforementioned desirable physical and biological attributes associated with spider silk, it cannot function alone in the creation of mature, usable silk (Askarieh, Hedhammar et al. 2010). The CTD and NTD each contribute specific roles in the silk spinning process, and each will be discussed below.

MaSp C-terminal Domain Structure and Function

The repetitive domains of spidroins are flanked by non-repetitive N- and C-terminal domains. The sequences of these domains bear little resemblance to each other (Sponner, Unger et al. 2004, Rising, Hjälm et al. 2006, Gaines and Marcotte 2008); however, each are highly conserved across many species of spider and between types of silk (Sponner, Vater et al. 2005). This suggests that they play critical roles in the silk formation process. The CTD is primarily responsible for organization of the spidroins in the ampulle (Gaines, Sehorn et al. 2010). The NMR structure of the CTD has been solved in solution, revealing several key aspects that allude to its function (Figure 1.9) (Hagn, Eisoldt et al. 2010, Wang, Huang et al. 2014, Otikovs, Chen et al. 2015).

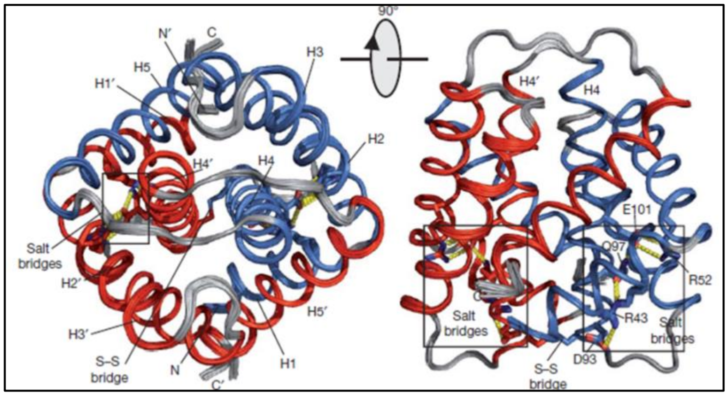

Figure 1.9, NMR structure of the *A. diadematus* spidroin CTD. The 20 best-energy structures of the *A. diadematus* ADF3 CTD were overlaid with a root mean square deviation (RMSD) of 0.18 Å. The structure reveals that the CTD forms a homodimer with helices 1, 4 and 5 forming the dimer interface. Intrasubunit salt bridges between R43 and D93 and between R52 and E101 stabilize the tertiary structure by fixing helices 1 and 2 to helix 4. An intermolecular disulfide bond between C92 of each subunit stabilizes the quaternary structure. PDB: 2KHM. Image taken from Hagn et al. 2010 (Hagn, Eisoldt et al. 2010).

The monomers are covalently linked via a disulfide bond, and sequence homology analysis of the CTD reveals that the cysteine residue involved in this bond is highly conserved (Wang, Huang et al. 2014). Additionally, two intramolecular salt bridges between oppositely charged residues were identified as the first points of protein unfolding in salt denaturation experiments, which indicated that the salt bridges were critical to tertiary structure because they stabilized intramolecular helix alignment. The R43-D93 salt bridge stabilizes the helix 1-helix 4 orientation, while the R52-E101 salt bridge stabilizes the helix 2-helix 4 orientation (Gao, Lin et al. 2013). Finally, the dimer interface was identified as consisting of mainly hydrophobic residues along helices 1, 4, and 5 (Wang, Huang et al. 2014).

Several studies have investigated the function of the CTD by recombinantly expressing it fused with four units from the repeat region (Rn-CTD) and comparing this construct to the Rn by itself. When exposed to shear forces and/or high concentrations of sodium phosphate (as described above), the Rn-CTD complex formed larger and more ordered aggregates compared to the Rn alone. The resulting macroscopic Rn-CTD fibers also displayed molecules aligned with the fiber axis, compared to the random alignment seen in the Rn aggregates (Eisoldt, Hardy et al. 2010, Hagn, Eisoldt et al. 2010). Additionally, it was shown that the aforementioned disulfide bond was not critical to fiber formation for Rn-CTD constructs. Using the *A. diadematus* ADF3 spidroin (described above) as their model, Ittah et al. created C52S and C52R mutants to compare to the wild type Rn-CTD construct. The cysteine to serine mutation did not alter fiber morphology compared to wild type, suggesting that the fibers could form without the disulfide bond. Conversely, the cysteine to arginine mutant disrupted CTD homodimerization, which severely inhibited fiber assembly (Ittah, Cohen et al. 2006, Ittah, Michaeli et al. 2007). Therefore, it was concluded that the dimerization of the CTD is necessary for fiber formation but that this dimerization is not necessarily dependent on the disulfide bond. However, since the cysteine is so highly conserved and is most likely involved in properly aligning CTD monomers (Wang, Huang et al. 2014), its importance in the functionality of the CTD should not be overlooked. Interestingly, the CTD appears to be unresponsive to changes in pH, since the rate at which Rn-CTD constructs aggregated was unaffected by pH (Askarieh, Hedhammar et al.

2010). It was suggested the disulfide bond covalently links the CTDs together before any pH-dependent effects can occur to alter fiber formation (Sponner, Vater et al. 2005).

In summary, the conserved disulfide bonds limit polymerization to CTD-CTD homodimer formation, which prevents amorphous aggregation. This promotes spidroin organization in the ampulle gland by limiting fiber elongation to head to head and tail to tail positioning (Gao, Lin et al. 2013, Wang, Huang et al. 2014). As discussed below, the NTD does not contain cysteines, which, combined with the differences in primary sequence and tertiary structure, severely limits the possibility of NTD-CTD heterodimer formation. Instead, NTD-NTD homodimer formation has been shown to be crucial to spidroin organization and silk formation, and the NTD dimerization process has been a primary focus of most of the recent work concerning the roles of spidroin domains during silk formation, including this one.

The N-terminal Domain is Crucial to Silk Formation

General role of the NTD in silk formation

The concept of *in vivo* silk production provides an interesting dilemma. Large quantities of pre-spun silk components must be synthesized and stored so that the spider has ready access to it (Chen, Knight et al. 2002), but the silk cannot be allowed to prematurely aggregate as this would clog the spinning duct (Breslauer, Lee et al. 2009) and most likely kill the spider. The general structures and functions of both the Rn and CTD have been presented, with the CTD forming homodimers to link spidroins together, and the Rn adopting a primarily β-sheet secondary structure induced by the shear forces of the narrowing spinning duct. However, in the context of the complex silk spinning process, these two domains cannot provide the full mechanism for how soluble spidroins are converted into mature fibers. Thus, as will be described below, the NTD functions to provide a salt- and pH-dependent dimerization mechanism that facilitates the controlled, rapid assembly of the spidroins into mature silk.

The Effects of Salt Concentration on NTD Dimerization

As described above, the spidroins experience a decrease in salt concentration during their journey through the spinning duct (Vollrath and Knight 1999, Knight and Vollrath 2001, Sponner, Vater et al. 2007). Although salt does not appear to have an effect on the secondary structure of the *E. australis* MaSp1 NTD (Hedhammar, Rising et al. 2008), it has been established that the decrease in salt concentration is partially responsible for the formation of *E. australis* (Hagn, Thamm et al. 2011) and *N. clavipes* (Gaines, Sehorn et al. 2010)NTD homodimers. Using size exclusion chromatography (SEC), Gaines et al. showed that for the *N. clavipes* MaSp1A NTD, at pH 7.0 and high concentrations of sodium chloride (500 and 1000 mM), the NTD was mostly monomeric, but lowering the NaCl concentration caused the NTD to form homodimers. When the pH was decreased to 5.5, the NTD was slightly more dimeric at each salt concentration (Figure 1.10). These data were confirmed using a tryptophan fluorescence assay (the details of this procedure will be explained below) and a pulldown assay, in which free NTD was pulled from solution via homodimer interaction with resin-immobilized NTD of the same type (Gaines, Sehorn et al. 2010). These results are consistent with NMR spectra of the *L. hesperus* MaSp1 NTD (Hagn, Thamm et al. 2011), which showed significant peak broadening at lower salt concentration, indicating dimer formation, and they are also consistent with tryptophan fluorescence and urea denaturation experiments using the *E. australis* MaSp1 NTD (Kronqvist, Otikovs et al. 2014). Thus, the dimerization of the NTD as salt concentration decreases is consistent for all MaSp NTDs studied and is mostly likely crucial during the silk formation process for all spidroins.

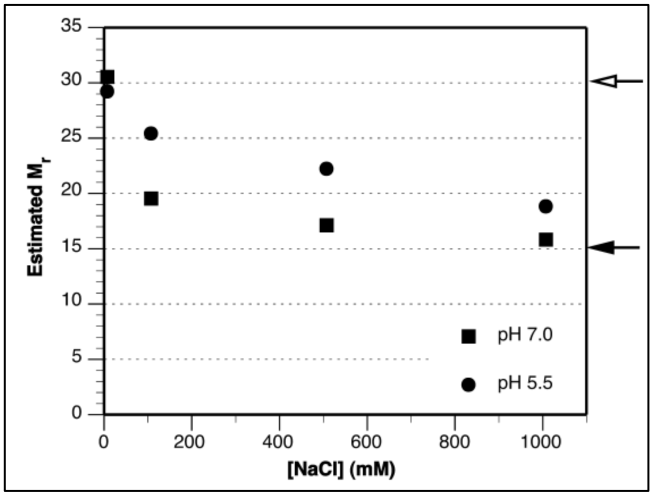

Figure 1.10, Salt concentration and pH affect the estimated molecular weight of *N. clavipes* MaSp1A NTD. The *N. clavipes* MaSp1A NTD was chromatographed in buffers at pH 7.0 or 5.5 and containing 0, 100, 500, or 1000 mM NaCl. Molecular masses (in kDa) are based on the SEC elution profile compared with molecular mass standards. Closed and open arrows indicate the predicted monomer and dimer molecular masses, respectively. Image taken from Gaines et al. 2010 (Gaines, Sehorn et al. 2010).

NTD Dimerization is a pH-Dependent Process

As described above, the spidroins also experience a decrease in pH along the spinning duct which serves to convert the spidroins into usable silk (Vollrath and Knight 1999). Using the *E. australis* MaSp1 as their model system, Askarieh et al. recombinantly synthesized “mini-spidroins,” which contained combinations of the NTD, four blocks of the Rn, and/or the CTD. As shown in Figure 1.11, the presence or absence of the NTD (large red circles) controls macroscopic assembly depending on the pH of the reaction. At pH 7, the NTD delays fiber formation, while at pH 6, the NTD accelerates formation. In comparison, the CTD (small green circles) accelerates assembly formation with respect to the repeat region without either terminal domain, but the pH does not affect this process. Assuming the activity of the mini-spidroins mimics the *in vivo* silk formation process, pH-dependent macroscopic fiber assembly is significantly more dependent on the NTD than the CTD (Askarieh, Hedhammar et al. 2010).

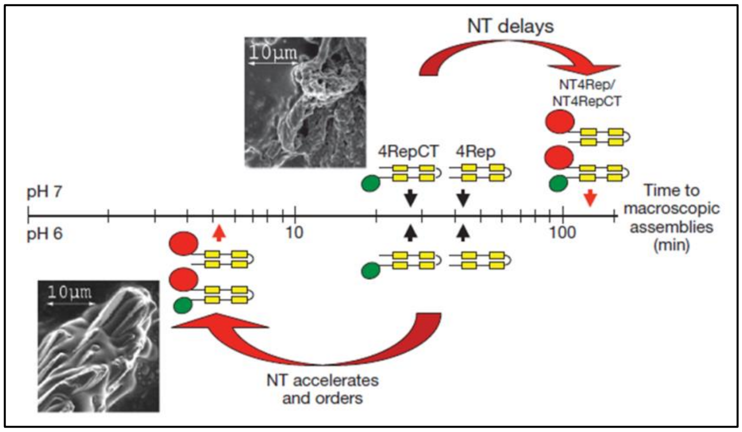

Figure 1.11, pH-dependent assembly of mini-spidroins. The time for self-assembly of mini-spidroins with NT (NT4RepCT or NT4Rep) or without NT (4RepCT or 4Rep) at pH 7 (above time scale) or at pH 6 (below time scale) was measured. The arrows indicate when macroscopic structures were first detected. The scanning electron micrographs are representative for early structures of 4RepCT at both pH 6 and 7 (figure above time axis) and of NT4RepCT at pH 6 (figure below time axis), respectively. The self-assembly process results in continuous fibers only for mini-spidroins including the C-terminal domain (NT4RepCT and 4RepCT). Image taken from Askarieh et al. 2010 (Askarieh, Hedhammar et al. 2010).

It was shown that this accelerated fiber assembly hinges on the pH-dependent dimer formation of the NTD. For all model systems studied, the MaSp NTD formed homodimers as the pH was decreased, and this mechanism was consistent regardless of the assay used (tryptophan fluorescence, size exclusion, pulldown assay, NMR, urea denaturation, etc.) (Gaines, Sehorn et al. 2010, Landreh, Askarieh et al. 2010, Hagn, Thamm et al. 2011, Jaudzems, Askarieh et al. 2012, Kronqvist, Otikovs et al. 2014). The pH-dependent dimerization was also observed for the *Araneus ventricosus* minor ampullate spidroin (MiSp) NTD (Otikovs, Chen et al. 2015), suggesting that this mechanism is conserved across all types of spider silks.

As described, the NTD forms homodimers when the salt concentration and/or pH are decreased. However, none of the NTDs studied contain cysteine residues; in fact, the absence of cysteines is highly conserved (Rising, Hjälm et al. 2006, Gaines and Marcotte 2008, Askarieh, Hedhammar et al. 2010). Thus, unlike the dimerization mechanism of the CTD described above, the formation of intermolecular disulfide bonds is not the cause for NTD homodimerization. Instead, the salt- and pH-mediated dimerization is facilitated by specific, highly conserved residues, which were identified through analysis of several MaSp and MiSp structures solved by X-ray crystallography and NMR.

Structures of Various Spidroin NTDs

The crystal structure of the *E. australis* NTD was the starting point for detailed analysis of the NTD and its role in spider silk formation (PDB: 3LR2) (Askarieh, Hedhammar et al. 2010). Similar to the CTD, the NTD structure is a homodimer consisting of two bundles of five α-helices. The monomers align in an antiparallel fashion such that helices 2, 3, and 5 form the dimer interface. As shown in Figure 1.12A, the residues that comprise the helices are highly conserved across the many studied species, indicating that the overall structure of NTDs is conserved to serve its necessary function in the silk spinning process. Additionally, as shown in Figure 1.12B, clusters of charged residues appear at opposite ends of the five-helix bundle so that when the two subunits form the dimer, the opposite charges are aligned.

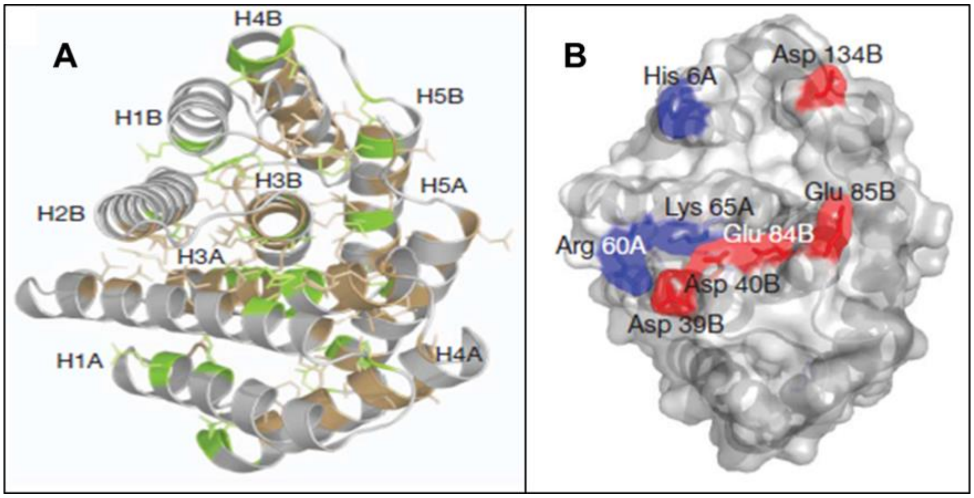

Figure 1.12, Crystal structure of the *E. australis* MaSp NTD. (A) Crystal structure of *E. australis* NTD, with strictly conserved residues colored green and residues conserved in greater than 60% of studied NTDs colored brown. **(B)** Location of charged residues; acidic residues are in red, basic residues are in blue. Images taken from Askarieh et al. 2010 (Askarieh, Hedhammar et al. 2010).

An NMR structure for the *E. australis* NTD (PDB: 2LPJ) (Jaudzems, Askarieh et al. 2012) at pH 7.2 was also solved, and the protein was found to be a monomer. The difference between the monomer and dimer structures appeared to be dependent on pH, since the crystal structure was solved for protein that crystallized at pH 6.0. Comparison of the monomer NMR structure and dimer crystal structure revealed differences in the angles between the helices, which either buried (in the monomer) or exposed (in the dimer) the single conserved tryptophan at residue 10. To further investigate the differences in subunit shape between the monomer and dimer, the A72R mutant was generated. It was observed that alanine 72 was directly in the middle of the dimer interface, so insertion of a large, charged side chain was intended to prevent dimer formation. Indeed, the A72R mutant crystallized as a monomer (PDB: 4FBS) (Jaudzems, Askarieh et al. 2012), and comparison with the WT dimer crystal structure and WT monomer NMR structure revealed better alignment with the monomer, including highly similar side chain conformation around the buried tryptophan (Figure 1.13) (Jaudzems, Askarieh et al. 2012).

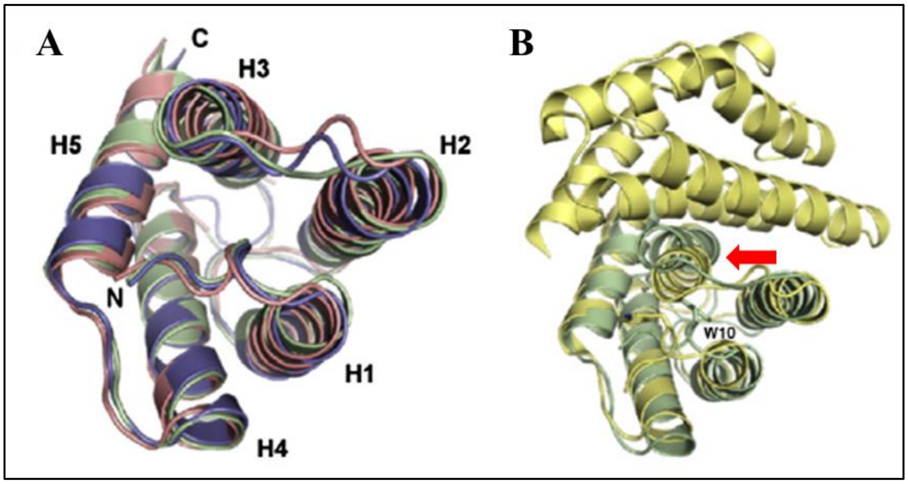

Figure 1.13, Comparison of monomeric and dimeric NTD structures. (A) Superposition of the NMR (blue) and crystal (salmon) structures of A72R with the NMR structure of WT NTD at pH 7.2 (pale green). **(B)** Superposition of the WT monomeric NTD NMR structure (pale green) with one subunit (chain B) of the crystal structure of WT NTD dimer (pale yellow). The second yellow structure is the other subunit (chain A) of the dimeric crystal structure. The side chain of Trp10 is shown with sticks and labeled. The red arrow indicates the rearrangement of helix 3 that must occur when Trp10 shifts from a buried conformation in the monomer to an exposed conformation in the dimer. In **(A)** and **(B)**, the structures were superimposed for minimal RMSD of the backbone N, C_α and C′ atoms of residues 8–82 and 90–130. Image adapted from Jaudzems et al. 2011 (Jaudzems, Askarieh et al. 2012).

Key Mechanisms that Govern NTD Dimerization

As described above, the decreases in salt concentration and pH observed in the spinning duct facilitate NTD dimerization. Analysis of the crystal and NMR structures of the *E. australis*

MaSp1 NTD (henceforth ^{Ea}NTD) revealed a series of specific, conserved residues that are affected by these forces and are involved in the mechanisms that regulate NTD homodimer formation. In addition to the WT and A72R mutant described above, a series of point mutations were generated to investigate the role that these residues play in the pH-dependent dimerization. Each of these point mutants were subjected to tryptophan fluorescence experiments conducted over a pH range of 5.6-7.6, which represented the pH range that the spidroins experience *in vivo* from production in the ampulle gland to the exit of the spinning duct (Knight and Vollrath 2001). The protein was excited at 280 nm, while emission spectra from 300-400 nm were collected. To analyze the data, the ratio of the intensity at 338 nm to 353 nm was calculated at each pH step, as these values corresponded to the WT protein in its monomeric and dimeric states, respectively. This intensity shift is reflective of the conformational change of W10 as the NTD converts from the monomer to dimer states, as shown in Figure 1.14A. In the tryptophan fluorescence assay, the A72R mutant remained monomeric throughout the pH decrease, and its structure more closely resembled the WT monomer instead of the dimer (data not shown). Thus, the structural differences between the monomer and dimer subunit had been established; however, the specific mechanisms that governed the transition between these two states were still not completely understood (Jaudzems, Askarieh et al. 2012).

As seen in the MaSp CTD (described above), oppositely charged residues can form salt bridges to stabilize structural elements; it was suspected that D39, D40, R60, and K65 in the NTD were involved in intersubunit salt bridges that aided in dimer formation based on the relative proximity of these residues in the crystal structure (Askarieh, Hedhammar et al. 2010). Thus, the point mutants D40K, K65D, K65A, and R60A were generated to disrupt these potential electrostatic interactions (Kronqvist, Otikovs et al. 2014). As shown in Figure 1.14B, the charged residues D40, R60, and K65 were necessary for intersubunit electrostatic interactions that participated in NTD dimerization. Mutating these side chains to the opposite charge resulted in dimer formation that required a lower pH (K65D) or did not occur at all (D40K), which mirrored the trend of the established monomer mutant, A72R. Mutation to neutral residues (K65A and R60A) also decreased dimer formation, but not as drastically as the opposite charge mutants. The formation of intersubunit salt bridges between the charged residues was also investigated using a metadynamics simulation that predicted the strength of specific salt bridges in the absence or presence of 500 mM NaCl. The simulated data showed that high salt increases the distance between specific pairs of oppositely charged residues. It was concluded that the sodium chloride ions shield the electrostatic interactions between charged residues, which inhibits the formation of intermolecular salt bridges (Gronau, Qin et al. 2013). Together, these results suggest that intermolecular electrostatic interactions between oppositely charged residues facilitate NTD dimer formation during the pH and salt decreases experienced by the spidroins during the silk spinning process.

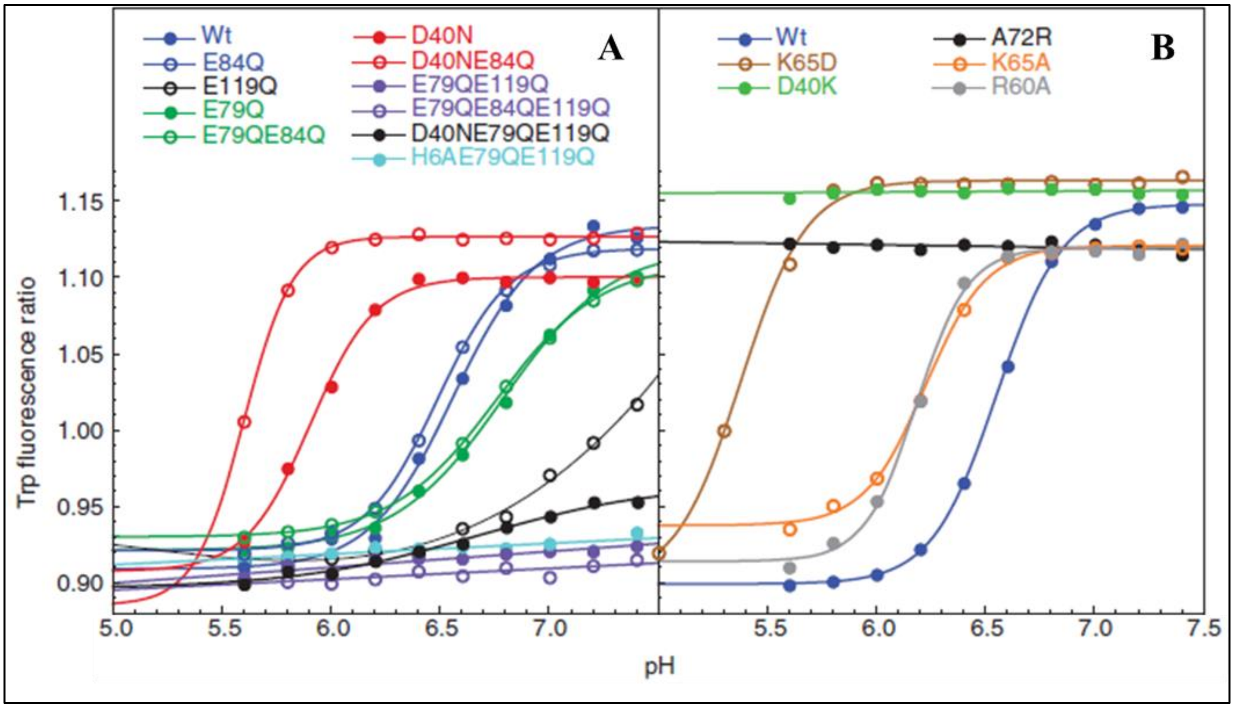

Figure 1.14, Tryptophan fluorescence assay for *E. australis* MaSp1 NTD. The ratio of tryptophan fluorescence at 338 nm (monomer state) to 353 nm (dimer state) for **(A)** protonation mimic mutants and **(B)** salt bridge disrupting mutants is shown. Image adapted from Kronqvist et. al. 2013 (Kronqvist, Otikovs et al. 2014).

Additionally, analysis of the WT ^{Ea}NTD structure revealed a curious orientation of acidic residues D40 and E84. These residues formed an intramolecular "handshake" interaction, a term coined to describe the effect when the oxygen atoms of two acidic side chains are within hydrogen bonding distance of each other (Askarieh, Hedhammar et al. 2010). A survey of 151 unique crystal structures revealed 102 pairs of acidic residues forming this interaction, with 31 of those pairs involving an aspartic acid and a glutamic acid with an average distance between the closest oxygen atoms of 2.6 Å (Flocco and Mowbray 1995). Thus, it was suspected that the D40-E84 handshake seen in the ^{Ea}NTD stabilized the structure until the decrease in pH protonated one or both of these side chains. Additionally, the WT structure was used in a pH-titration simulation to identify ionizable residues within the physiologically relevant pH range. This simulation identified conserved acidic residues E79 and E119 to be protonated as the pH decreases, and it was proposed that the neutralization of these side chains may be necessary to stabilize the NTD dimer (Wallace and Shen 2012). To investigate these possible protonation events, mutants that mimicked the protonated states of the acidic residues were generated. Double and triple point protonated mimics were also generated to ascertain the specific contribution of each acid side chain (Kronqvist, Otikovs et al. 2014). The aforementioned tryptophan fluorescence assay was employed to determine the effects of these point mutations on pH-dependent dimer formation. As shown in Figure 1.14A, the protonation-mimic mutants produced different effects on the dimer formation capacity of the NTD. The protonation of D40 decreased dimer formation on its own and in combination with the protonation of E84. The protonation of E84 by itself had no effect compared to WT, but when combined with the protonation of E79 and E119, it significantly promoted dimer formation. Conversely, the protonation of E79 and E119 promoted dimer formation at a higher pH, even when combined with the protonation of D40. The dimer was further stabilized in the E79Q/E84Q/E119Q triple mutant, indicating that within the D40-E84 handshake, D40 stabilizes the interaction until E84 is protonated. The need for all three of E79, E84, and E119 to be protonated was supported by charge difference experiments, in which it was determined that the WT protein accumulated three protons during the pH change from 8.0 to 5.0. Taken together, it was concluded that the acidic residues serve different purposes in dimer formation: D40 is necessary for intersubunit salt bridge formation with K65, which stabilizes the quaternary structure. Concurrently, the pH-mediated protonation of E79 and E119 stabilizes the tertiary structure of each subunit in the dimer structure, and the protonation of E84 further strengthens the dimer structure (Kronqvist, Otikovs et al. 2014). The pH-sensitive relay mechanism, in which the protonation of multiple acidic residues is necessary to fully stabilize the dimer, was also observed in the *A. ventricosus* MiSp NTD, albeit with a different set of conserved acidic residues. These data indicate that pH-dependent dimerization is a conserved mechanism for spidroin assembly, but that the residues involved in this process may differ depending on the structure of the NTD (Otikovs, Chen et al. 2015).

Based on their data, Kronqvist et al. proposed a multistep model for NTD dimerization during the silk spinning process: oppositely charged residues utilize electrostatic interactions to align the two NTD monomers, which leads to elevated pKa values of E79 and E119. Protonation of these acidic residues results in a weakly associated dimer, and the dimer is fully stabilized upon protonation of E84 (Figure 1.15).

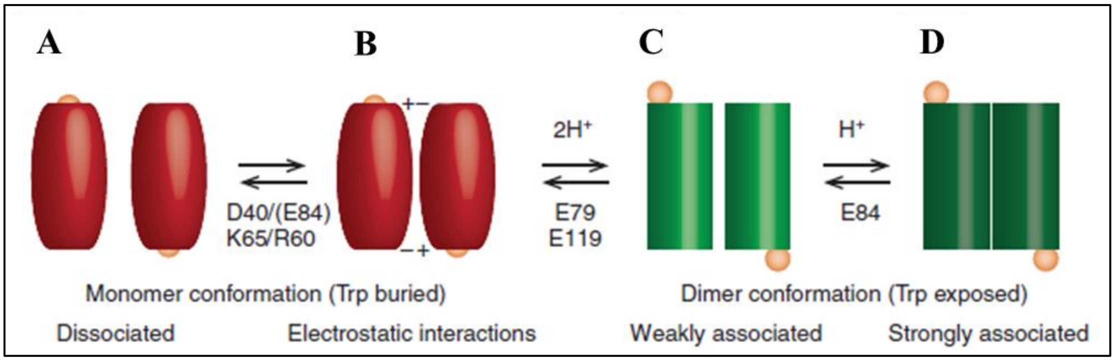

Figure 1.15, Proposed mechanism for NTD dimerization. (A) NTD molecules with a monomer conformation where W10 is buried in the hydrophobic core. **(B)** Electrostatic interactions mediated by D40, K65 R60 and possibly E84 in their charged state lead to elevated pKa values for E79 and E119 due to a changed environment between associated monomer subunits. **(C)** Protonation of E79 and E119 at pH 6.5 leads to the structural conversion to a weakly associated dimer conformation in which W10 becomes exposed to a more polar environment. **(D)** Upon further decrease in pH to 5.7, protonation of E84 promotes conversion from weakly associated dimers to strongly associated and fully stable dimers. Image taken from Kronqvist et al. 2014 (Kronqvist, Otikovs et al. 2014).

Summary

The roles of the NTD, Rn, and CTD have all been established within the context of the silk spinning process. As shown in Figure 1.16, after spidroins are synthesized in the tail region, they are stored in the ampullate gland at extremely high concentrations. At this stage, the CTD forms homodimers via disulfide bonds to link spidroins together tail to tail, and the Rn adopts a mostly disordered secondary structure. The high salt concentration and pH of the ampullate gland stabilize the NTD in a mostly monomeric conformation. As the spidroins are utilized for silk, they exit the ampullate gland and proceed down the narrowing spinning duct. The tapered geometry aligns the spidroins and induces the Rn to adopt a predominantly β-sheet conformation, which imparts the silk with its characteristic strength and elasticity. Water and salt ions diffuse out of the spinning dope, promoting expansion of the spidroins and alignment of the NTD via electrostatic interactions. The concomitant pH decrease allows for the protonation of key acidic residues that promotes a stably associated NTD dimer, linking the spidroins head to head along the fiber axis. The tightly wound spidroins form the inner and outer core of the silk fiber, and are covered with the protective glycoprotein and lipid coats. Finally, the spinneret pulls the mature fibers from the duct for the silk's intended purpose (Vollrath and Knight 1999, Knight and Vollrath 2001, Sponner, Vater et al. 2005, Gaines, Sehorn et al. 2010, Andersson, Holm et al. 2013, Kronqvist, Otikovs et al. 2014).

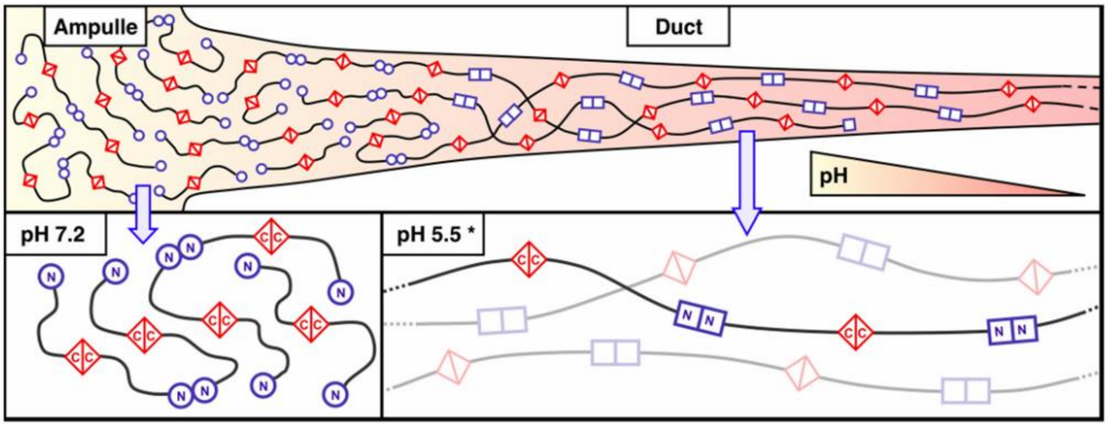

Figure 1.16, Model of proposed MaSp assembly into multimeric strands. MaSp proteins stored in the ampulle (left side of top panel and bottom left panel) exist as dimers stably adjoined through their CTDs (red triangles). The NTDs are mostly monomeric at this pH (blue circles), but could associate weakly with NTDs of other spidroins. Through these interactions, MaSp oligomers of short lengths can be formed, and because of the dynamic nature of the NTD association, tangles of spidroins that impede flow can be resolved. As these oligomers are drawn into the duct during spinning, they eventually experience a threshold pH (middle of top panel) at which NTDs associate much more strongly (blue squares). Stable attachments between MaSp molecules at both termini cause the formation of long multimeric strands (bottom right panel). To emphasize the terminal domain connectivity in this schematic, the length of the repeat domains (black lines) has been greatly reduced, the degree of entanglement or other supra-molecular organization among spidroin molecules has been simplified, and the amount of molecular alignment has been exaggerated. The ampullate gland pH (7.2) and duct pH (5.5) are shown. Image taken from Gaines et al. 2010 (Gaines, Sehorn et al. 2010).

The *N. clavipes* MaSp1A NTD appears to be similar to other NTDs in the pH- and salt-dependent dimer formation it exhibits (Gaines, Sehorn et al. 2010), which is unsurprising given the highly conserved sequence identity it shares with the NTDs of spidroins of other spider species (Askarieh, Hedhammar et al. 2010), including conservation of the acidic residues involved in the pH-relay mechanism described above. However, the *N. clavipes* NTD sequence also contains 6 more acidic residues than its *E. australis* counterpart, leaving open the possibility of other residues being involved in the pH-dependent dimerization mechanism. Additionally, NMR backbone assignments of the WT NTD have been collected in monomer favoring conditions (pH 7.0, 500 mM NaCl), and secondary structure analysis revealed six helical regions (Figure 1.17) (Parnham, Gaines et al. 2011), which differs from the canonical five helix bundle seen in the *E. australis* (Askarieh, Hedhammar et al. 2010) and *L. hesperus* (Hagn, Thamm et al. 2011) NTDs; based on the sequence alignment, helix 2 seems to be split into two separate secondary structures (Parnham, Gaines et al. 2011). Finally, as mentioned earlier, *N. clavipes* dragline silk displays noticeably different mechanical properties compared to its counterparts of other species (Vollrath and Knight 2001), which could be a result of the differences in primary sequence or secondary structure.

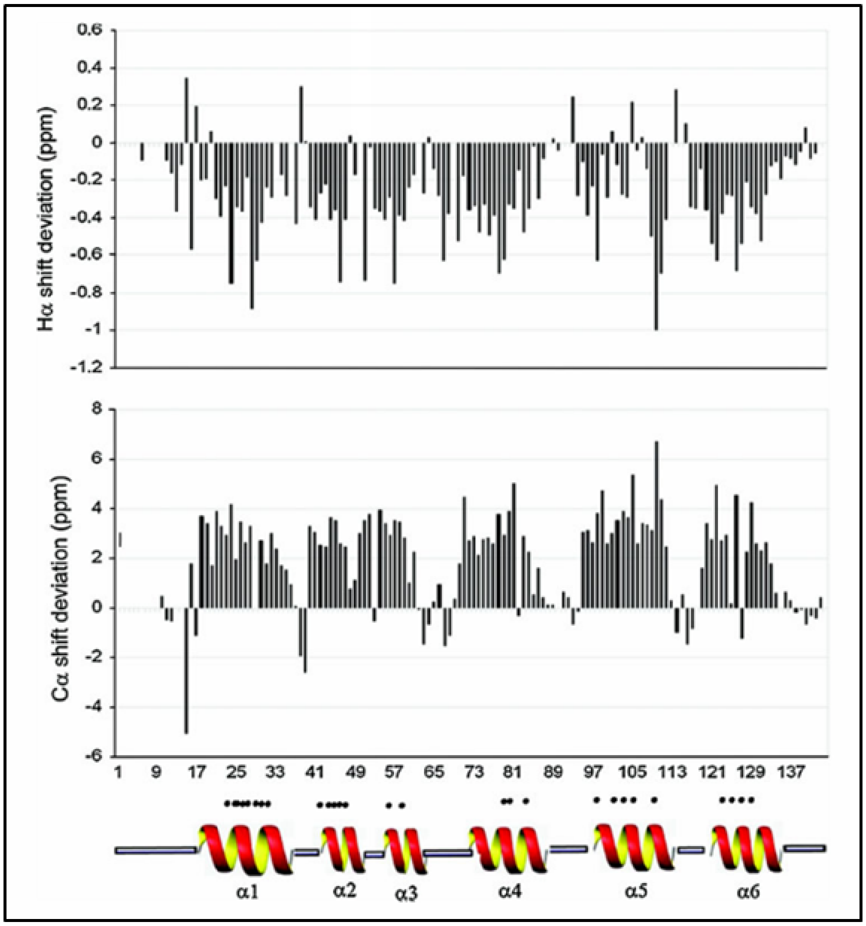

Figure 1.17, NMR-derived secondary structure predictions for the *N. clavipes* MaSp1A NTD. Proton (top panel) and carbon (bottom panel) chemical shift deviations used to derive the secondary structures. The accompanying predicted helix locations are shown, dividing the NTD into six α-helices. Image taken from Parnham et. al. 2011 (Parnham, Gaines et al. 2011).

The aim of this work is to investigate the structural differences between the *N. clavipes* and *E. australis* MaSp1 NTDs in order to further elucidate the biochemical mechanisms that contribute to NTD dimerization. Herein, I present the first published structure of the *N. clavipes* MaSp1A NTD, which reveals a distinct asymmetry at the dimer interface compared to other published NTD structures. Based on these findings, I propose that plasticity at the NTD dimer interface plays a role in the pH-dependent transition of the NTD from a loosely to a stably associated dimer as the spidroin progresses through the spider's silk extrusion duct.

Chapter 2: Crystal Structure of the *Nephila clavipes* Major Ampullate Spidroin 1A N-terminal Domain Reveals Plasticity at the Dimer Interface

Introduction

Spider silk displays remarkable mechanical and biochemical properties, making it a desirable component in many biomaterials applications (Kubik 2002). As described above, dragline silk is one of the strongest types of silk and has been the focus of many studies (Madsen, Shao et al. 1999), but the dragline silks from various spider species display variability in their mechanical properties (Vollrath and Knight 2001). The observed differences between the mechanical properties of *Euprosthenops* (high tensile strength) and *Nephila* (high flexibility) dragline silks (Madsen, Shao et al. 1999) could stem from differences in their primary and secondary structures of their MaSp NTDs (Parnham, Gaines et al. 2011). Thus, to further understand what structural features underlie these differences in mechanical properties, I solved the crystal structure of the *N. claivipes* major ampullate spidroin 1A (^{Nc}NTD) to 2.02 Å resolution. The ^{Nc}NTD structure contains asymmetric interactions including novel intermolecular salt bridges at opposite ends of the dimer (D39-K65 and D40-K65) that provide new insights into the crucial role these residues play in NTD dimer formation. The structure also reveals a unique intramolecular 'handshake' interaction between D17 and D53 which contributes to the asymmetry seen in the structure and potentially adds an additional layer of complexity to the pH-sensitive relay mechanism for NTD dimerization proposed by Knight, Johansson, and colleagues (Askarieh, Hedhammar et al. 2010, Kronqvist, Otikovs et al. 2014). The roles that these key salt bridge and handshake interactions play in dimer formation will be investigated in the next chapter.

Experimental Procedures

Protein expression and purification—All proteins in this study were expressed and purified using a slight variation of a previously published protocol (Gaines, Sehorn et al. 2010). The proteins were expressed by transforming the expression plasmids into BL21-DE3 (Stratagene) cells via heat-shock transformation. Large-scale cultures were grown in an incubated shaker at 37°C to an OD_{600} of 0.8. Protein overexpression was induced with 1 mM isopropyl β-D-1-thiogalactopyranoside (IPTG), and the cultures were shaken for an additional 18 hours at 18°C. Cells were harvested via centrifugation, and the pellets were re-suspended in buffer containing 20 mM Tris, pH 8.0 with 350 mM NaCl. The cells were lysed by sonication and purified using a GSTrap 4B column or GSTrap agarose gel bed (GE Healthcare Life Sciences). Affinity-tagged protein was eluted using a buffer containing 15 mM glutathione in 50 mM Tris, pH 8.0, 1 mM DTT. The samples were then buffer-exchanged to the same buffer used for re-suspension of the pellets. The GST tag was cleaved by incubating the purified fusion protein with PreScission Protease (GE Healthcare Life Sciences) at a ratio of 1:1000 (w/w) overnight at 4°C. After GST removal, 10 vector-derived residues (GPLGSPGIPG) remained on the N-terminal end of the mature protein. The samples were then purified using gel filtration (Hi Load 26/600 Superdex 75 pg, Amersham) in the 20 mM Tris, pH 8.0 with 350 mM NaCl buffer to separate the GST tag from the NTD. The samples were buffer exchanged to 20 mM Tris, pH 8.0 with 50 mM NaCl, then purified via ion exchange (MonoQ 10/100 GL, Amersham) using 20 mM Tris, pH 8.0 with 50 mM NaCl as Buffer A and 20 mM Tris, pH 8.0 with 1 M NaCl as Buffer B with a gradually increasing buffer B:A ration to fully separate the ^{Nc}NTD from the GST tag. The purity of each purified sample was assessed by SDS-PAGE using either a 15% or 17% acrylamide gel stained with Coomassie Brilliant Blue (See Appendix Figure A.1). The pure ^{Nc}NTD was then concentrated and/or buffer exchanged as needed.

X-ray crystallography—The ^{Nc}NTD was purified as described and concentrated to a final concentration of 10.1 mg/ml in a buffer containing 20 mM Tris pH 8.0 and 50 mM NaCl. The Index (Hampton Research) and JCSG Core I, II, III, and IV (Qiagen) commercial screens were used for sparse-matrix screening in 96-well Greiner microplates (400 nl sitting drop vapor diffusion format) to identify conditions suitable for crystal growth. The Crystal Gryphon robot (Art Robbins Instruments, Asbach, Germany) was used to set these trays. Diffraction-quality crystals were grown by manually mixing 1.0 µl of protein with 1.0 µl of well solution (0.1 M BIS-TRIS pH 6.5, 29% w/v PEG 3,350) by hanging drop vapor diffusion at 18°C. Crystals formed within 1-2 days and were harvested by flash freezing in liquid nitrogen in mother liquor plus 10% ethylene glycol as a cryoprotectant. The protein crystallized in the $P3_121$ space group with unit cell dimensions a=b=67.5 and c=90.4. There was one copy of the NTD dimer in the asymmetric unit and the crystal had an estimated solvent content of 38.0% (determined by Matthew's Coefficient calculator, http://www.ruppweb.org/mattprob/default.html). Diffraction data sets were collected on the Southeast Regional Collaborative Access Team (SER-CAT) 22-ID beamline at the Advanced Photon Source, Argonne National Laboratory. All data were indexed, integrated, and scaled using HKL2000 (Otwinowski and Minor 1997).

Structure determination and refinement—A data set was collected to a resolution of 2.02 Å for the *N. clavipes* major ampullate spidroin NTD. The R_{merge} values for the two highest resolution shells of this data set were 46 and 60%, respectively. The highest resolution shell was included due to its high I/σ_I (5.6) and $CC_{1/2}$ (93.5) and based on improved electron density map quality compared to alternatively processed data with lower resolution cut-offs. The structure of the *E. australis* major ampullate spidroin NTD (PDB: 3LR2) was used as the model for molecular replacement using the PHASER software (McCoy, Grosse-Kunstleve et al. 2007). The model was refined to R_{cryst}/R_{free} values of 0.164/0.205 by iterative refinement using PHENIX (Adams, Afonine et al. 2010) and COOT (Emsley 2013) software, and the electron density maps were of excellent quality (Figure 2.1, A-C). The final *N. clavipes* MaSp1A NTD model contains residues 6-82 and 87-128 in Chain A and residues 6-131 in Chain B. The model also contains Chain Z, which consists of the three amino acids SYG. I believe these to be residues 136-138; however, it is unclear as to which chain these residues belong, though it appears to derive from a symmetry-related NTD molecule in the crystal (Figure 2.1D). The refined structure also contained 123 water molecules. The detailed data collection and refinement statistics are listed in Table 2.1. Molecular graphics representations were generated using PYMOL (Schrodinger 2015) and the CCP4mg program of the CCP4 6.4.0 software suite (Winn, Ballard et al. 2011).

Results and Discussion

Overall structure of the N. clavipes major ampullate spidroin NTD

The ^{Nc}NTD structure is comprised of a five-helix bundle, and two NTD subunits form a homodimer, with helices 2, 3, and 5 forming the dimer interface (Figure 2.2A). Approximately 24% of each subunit's surface area is buried at the dimer interface, which is similar to the ~20% subunit surface area that is buried in the published ^{Ea}NTD (Kronqvist, Otikovs et al. 2014). Additionally, there are clusters of basic (K54, R57, K60, K64, K65) and acidic (D36, D39, D40, E79, D91) residues at opposite ends of each monomer subunit (Figure 2.2B). These charged areas create a dipole moment within each subunit, and the subunits are arranged antiparallel to accommodate the charged poles. This non-uniform charge arrangement aligns with other spidroin NTD structures (Askarieh, Hedhammar et al. 2010). The general similarity between the ^{Nc}NTD and the published ^{Ea} NTD structures (Askarieh, Hedhammar et al. 2010, Jaudzems, Askarieh et al. 2012) suggests that the structure is critical to the function of the NTD in the silk spinning process.

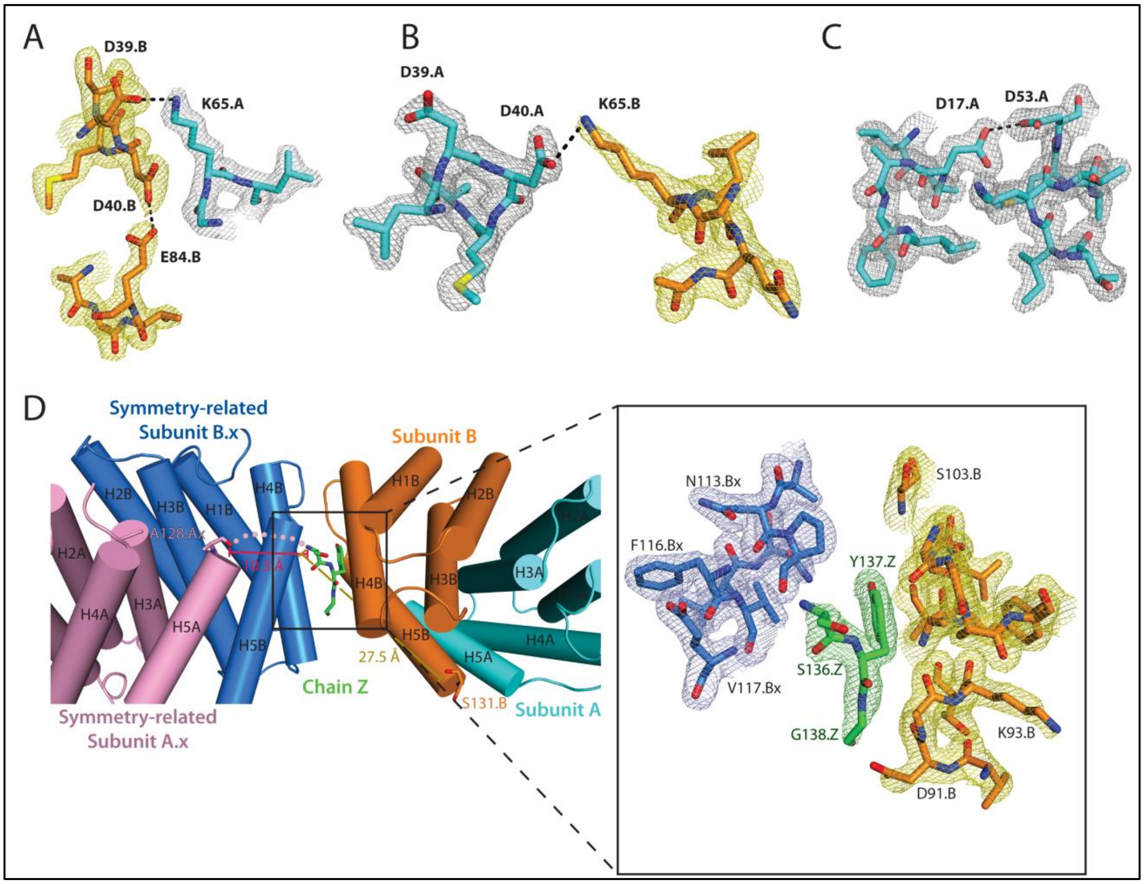

Figure 2.1, Key structural aspects of the ^{Nc}NTD. 2.02 Å 2F$_o$-F$_c$ electron density maps (contoured at 1.5σ) for selected regions of the structure including **(A)** the D39-K65 salt bridge and D40-E84 handshake at the ‘front’ end of the dimer interface, **(B)** the D40-K65 salt bridge at the ‘back’ end of the dimer interface, and **(C)** the D17-D53 handshake in subunit A. The electron density maps for subunit A are colored grey and those for subunit B are colored yellow. **(D)** Subunits A.x (pink) and B.x (blue) form the dimer of one symmetry-related molecule. Chain Z (green) was built into an area of electron density near the N-terminal end of helix 4B and consists of the residues SYG. The investigators believe that this chain contains residues 136-138 of the NTD, but it is unclear as to which chain these residues belong. The carboxyl groups of A128.Ax (the C-terminus of subunit A.x of the symmetry mate) and S131.B (the C-terminus of chain B of the actual structure) are the closest reasonable connection points for chain Z. Four residues (132-135) would not be enough to bridge the 27.5 Å gap to connect S131.B to the amino group of S136.Z. Therefore, chain Z most likely connects to chain A.x. In this case, the seven missing residues (QSSANEV) would easily connect to S136.Z, which is only 10.3 Å away from the C-terminus of this chain.

A comparison of the ^{Nc}NTD and ^{Ea}NTD was initiated by examining the differences in intramolecular secondary structure orientation between the subunits within each structure. The two subunits of the ^{Nc}NTD structure were not as structurally identical as those of the ^{Ea}NTD. The ^{Nc}NTD subunits superimposed with a backbone RMSD of 0.914 Å (Figure 2.2C), compared to the almost identical subunits of the ^{Ea}NTD (RMSD = 0.505 Å). In the ^{Nc}NTD subunits, helices 2, 3, and 5 are oriented differently with respect to helices 1 and 4. The helices will henceforth be referred to as H1-H5. Since the dimer interface consists of H2, H3, and H5, these architectural differences results in different dimer interfaces for the two NTD species (Figure 2.2D), which in turn results in a novel network of intermolecular contacts (Table 2.2). The details of the differences in subunit topology and the novel contacts that result will be discussed in greater detail below.

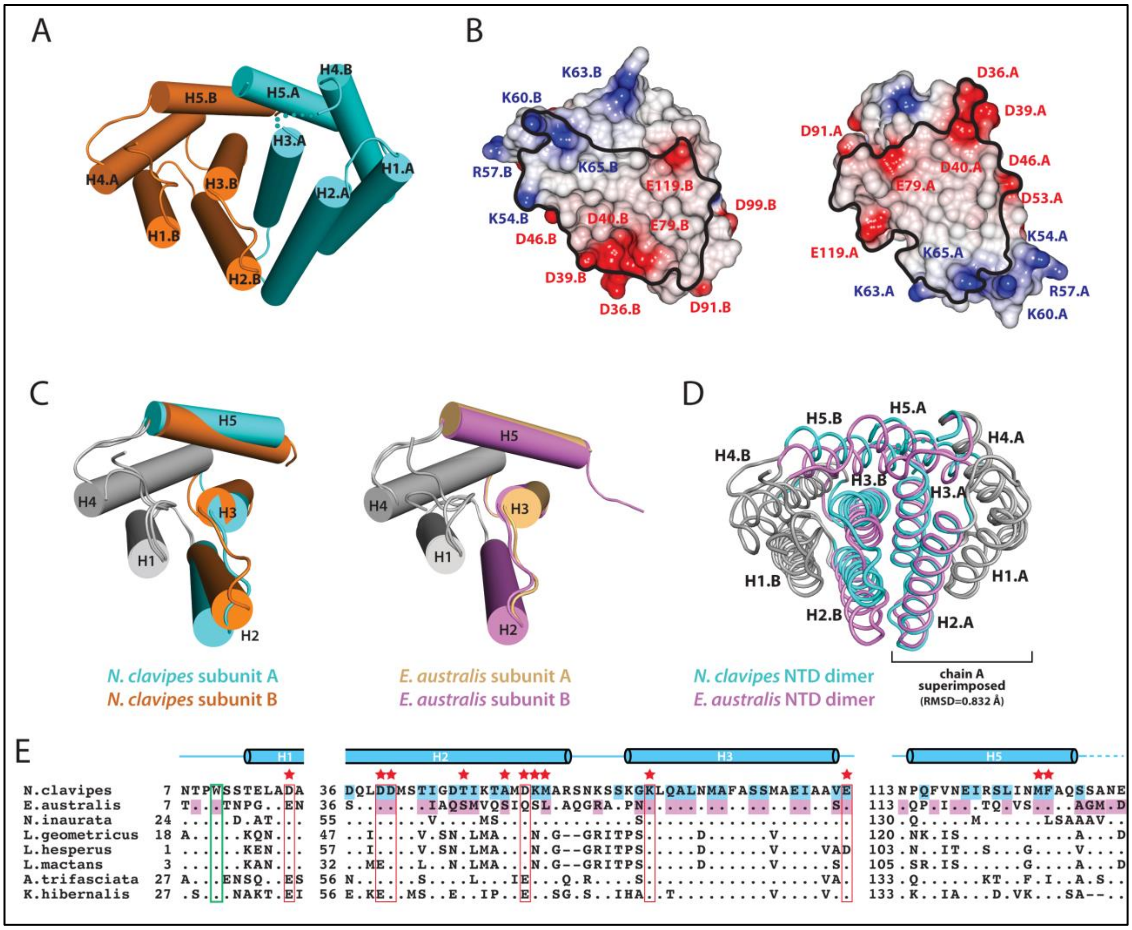

```
N.clavipes      7 NTPWSSTELADA  36 DQLDDMSTIGDTIKTAMDKMARSNKSSKGKLQALNMAFASSMAEIAAVE  113 NPQFVNEIRSLINMFAQSSANE
E.australis     7 T...TNPG..EN  36 S.......IAQSMVQSIQSL.AQGRA.PN..................S.  113 .QP.I...TQ.VS....AGM.D
N.inaurata     24 .....D.AT...  55 ........V....MS.............S....................  130 .Q.....M......LSAAAV..
L.geometricus  18 A.....KQN...  47 ..I....V.SN.LMA...N.G--GRITPS.....D......V.......  120 .NK.IS...........A...D
L.hesperus      1 ......KEN...  57 ..I....V.SN.LMA...N.G--GRITPS.....D......V....VAD  103 .N..IT..S...G....V....
L.mactans       3 ......KAN...  32 ..ME...L..N.LMA...N.G--GRITPS.....D......V.....S.  105 .SR.IS......G....A...D
A.trifasciata  27 A...ENSQ..ES  56 N......S....L...IE...Q.R....S.................VA.  133 .Q......KT..F.I..A.S..
K.hibernalis   27 .S...NAKT.EI  56 E.KE..MS..E..IP..E..SG.S..IHA..T.........V....V..  133 .K..IA...D.VK...SA--..
```

Figure 2.2, *N. clavipes* major ampullate spidroin NTD structure. (A) The crystal structure of the ^{Nc}NTD is shown as a ribbon representation with subunit A colored cyan and subunit B colored orange. Secondary structure elements are labeled H1–H5, and the letter A/B indicates the subunit. **(B)** The electrostatic surface potential of the ^{Nc}NTD shows clusters of positive and negative charges at opposite poles of each subunit. The structure is depicted in open book representation. The black outlines on the surface indicate the regions of each subunit that are making intermolecular contacts. The electrostatic potentials were calculated using the Poisson-Boltzmann method as implemented in CCP4mg with red and blue representing negative and positive electrostatic potential, respectively, on a scale ranging from +0.5 V to -0.5 V. **(C)** The subunits of the ^{Nc}NTD *(left)* and ^{Ea}NTD *(right)* structures were superimposed to highlight the topology of the helices comprising the five-helix bundles. Note that H2, H3, and H5 are oriented differently to H1 and H4 across the two subunits of the ^{Nc}NTD dimer, whereas the two subunits of the ^{Ea}NTD structure are virtually identical. The helices that comprise the dimer interface are colored, while non-interacting helices are grayed. **(D)** Comparison of the overall ^{Nc}NTD and ^{Ea}NTD structures. Chain A of the ^{Nc}NTD was superimposed with chain B of the ^{Ea}NTD as these were the subunits that were most similar to each other. Note the difference in the topology of the helices at the dimer interfaces of the structures. **(E)** The sequence alignment of MaSp NTDs is condensed to show the regions containing key residues involved in NTD dimerization. The secondary structure is shown above the sequence, and the dashed line at the C-terminus represents the disordered region. Cyan-shaded residues make intermolecular contacts in the ^{Nc}NTD structure. Violet shaded residues make intermolecular contacts in the ^{Ea}NTD structure. A period indicates a strictly conserved residue and a dash indicates a gap in the sequence. Residue numbers are shown on the left of each fragment of the alignment. Red boxes indicate residues involved in the key salt bridge and handshake interactions; red stars indicate other key residues at the dimer interface; the green box highlights the single, highly conserved tryptophan. The sequences chosen for alignment were based on the nucleotide-based distance trees for the major ampullate spidroin genes (Gaines and Marcotte 2008).

Notably, altered helix topology has been observed in other MaSp NTDs. The crystal structure for the monomeric ^{Ea}NTD A72R mutant (Jaudzems, Askarieh et al. 2012) shows distinct topological differences compared to the subunits of the wild-type ^{Ea}NTD dimer (Figure 2.3A), and it was shown that the monomer to dimer transition is dependent on structural rearrangement in which the 5-helix bundles adopt new conformations upon dimerization (Jaudzems, Askarieh et al. 2012). Additionally, in the ^{Nc}NTD structure, there are few crystal contacts around the dimer interface, suggesting that the differences in helix topology within this structure are not due to crystal packing. Together, the results suggest that the tertiary structural differences observed in the ^{Nc}NTD impact the mechanisms that control NTD dimerization.

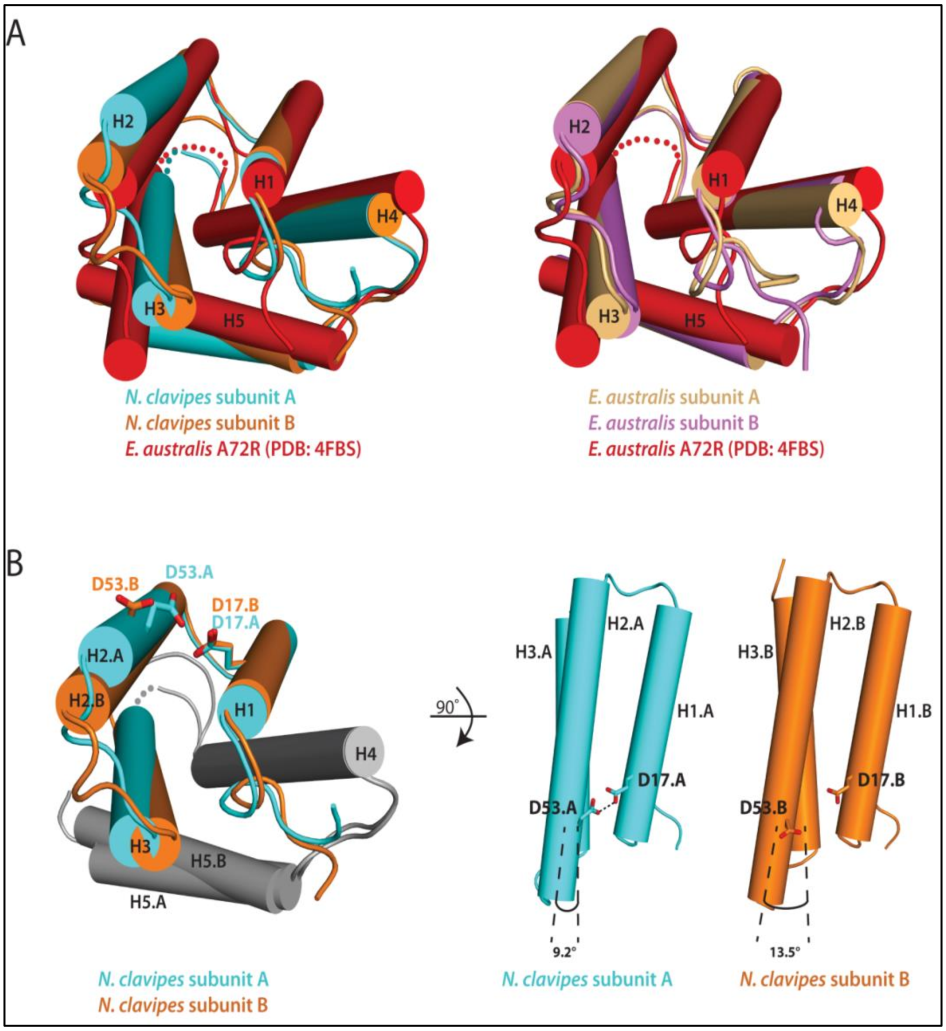

Figure 2.3, Altered helix topologies of monomer and dimer subunits. (A) Left, the subunits of the ^{Nc}NTD are superimposed along with the ^{Ea}NTD monomer crystal structure (A72R; PDB: 4FBS). Right, the subunits of the ^{Ea}NTD dimer crystal structure are superimposed with the ^{Ea}NTD monomer crystal structure. Both superimpositions illustrate the structural rearrangement of the five-helix bundle that occurs during the monomer to dimer transition. **(B)** The two subunits of the ^{Nc}NTD are superimposed. Side chains for residues D17 and D53 are shown, and the handshake interaction (black dashed line) between these two residues in subunit A (cyan) is shown. The D17-D53 handshake alters the angle between helices 2 and 3.

Distinct asymmetry among key salt bridge and handshake interactions

In addition to the differences in overall subunit topology, I also identified several key differences between the intermolecular contacts within the two structures. It had been previously established that residues D40, K65, and E84 were critical to the ^{Ea}NTD dimer formation process (Askarieh, Hedhammar et al. 2010, Kronqvist, Otikovs et al. 2014). In the ^{Ea}NTD crystal structure, D40 and E84 form an intramolecular handshake interaction (Askarieh, Hedhammar et al. 2010) that stabilizes the otherwise unfavorable clustering of two negatively charged residues (Flocco and Mowbray 1995). Additionally, the D40 and K65 side chains are 4.0 and 4.3 Å away from each other on the two ends of the dimer interface, which permits long-range electrostatic interactions. Importantly, the interactions involving D40, K65, and E84 are highly symmetrical, meaning that the equivalent residues on both subunits engage in the same intra- and intermolecular contacts (Figure 2.4C).

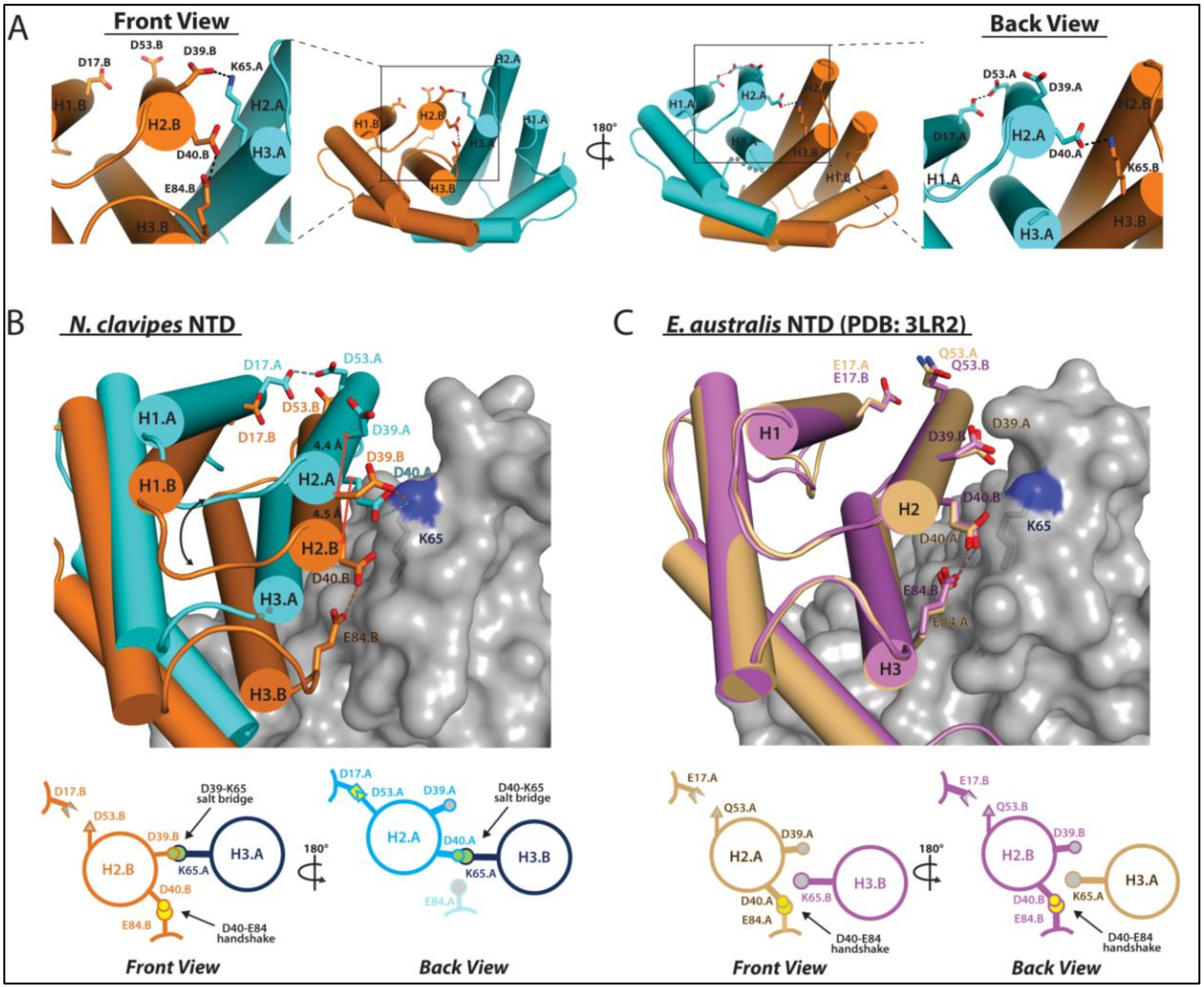

Figure 2.4, Comparison of key intra- and intermolecular interactions in the ^{Nc}NTD and ^{Ea}NTD structures. (A) Front and back views of the ^{Nc}NTD dimer reveals differences in the pattern of key salt bridge and handshake interactions taking place between equivalent residues on the two dimer subunits. **(B)** *(top)* To illustrate the asymmetry of the ^{Nc}NTD dimer interface, two copies of the NTD dimer were overlaid by superimposing the H1 and H4 of subunit A of one dimer with H1 and H4 of subunit B of the other. The subunits superimpose well with an RMSD of 0.525 Å and for clarity, only one copy is shown as a surface representation with the side chain of K65 shown as sticks. The other subunits of the dimers are shown as ribbons with residues involved in key intra- and intermolecular contacts shown as sticks. For a highly symmetrical dimer there would be two sets of equivalent interactions. *(bottom)* Cartoon schematic illustrating key intra- and intermolecular interactions at the ^{Nc}NTD dimer interface. **(C)** *(top)* Two copies of the ^{Ea}NTD dimer were superimposed and are shown as described in panel B. The ^{Ea}NTD dimer is more symmetric compared to the ^{Nc}NTD dimer and this is reflected by two sets of equivalent intra- and intermolecular interactions taking place between the subunits. *(bottom)* Cartoon schematic illustrating key intra- and intermolecular interactions at the ^{Ea}NTD dimer interface.

Conversely, the intra- and intermolecular interactions involving D40, K65, and E84 are distinctly different from their counterparts in the ^{Ea}NTD structure. Due to the asymmetric nature of these contacts in the ^{Nc}NTD structure, the two ends of the dimer interface are not identical, and for clarity, I have designated them as the 'front' and 'back' ends. At the front end, D40 and E84 form a handshake interaction that resembles the seen in the ^{Ea}NTD structure involving the same residues (Figure 2.4A). However, the intermolecular electrostatic interaction involving K65 is significantly different: this residue engages in a short-range (2.6 Å) intermolecular salt bridge with D39. On the back side of the dimer interface, D40 does not form a handshake interaction with E84, as the loop containing E84 is disordered in this chain. Instead, D40 forms a short-range (3.1 Å) intermolecular salt bridge with K65, and D39 is not involved in intermolecular contacts on this side of the dimer.

The role of D39, which is highly conserved across many species' NTDs (Figure 2.2E), in NTD dimerization had not been well studied, perhaps due to the fact that in the ^{Ea}NTD crystal structure, it does not appear to be involved in any intermolecular interactions (Askarieh, Hedhammar et al. 2010). In one recent study, systematic mutation of each of the acidic residues in the ^{Ea}NTD revealed that a D39N substitution significantly reduced dimer formation, but the authors of that study proposed that D39 was involved in pH-relay mechanism with D40 and E84 (Schwarze, Zwettler et al. 2013). However, the ^{Nc}NTD structure provides a molecular basis for the critical role of D39 in NTD dimerization as it clearly demonstrates that this residue engages in an intermolecular salt bridge with K65 (Figure 2.4A).

The intermolecular electrostatic interactions between D39, D40, and K65 in the ^{Nc}NTD and ^{Ea}NTD serve the same role, which is to facilitate proper subunit alignment in the dimer. However, the differences in the nature of these interactions in the ^{Nc}NTD and ^{Ea}NTD structures are reflective of the differences in subunit topology of the two dimers. As described above, the ^{Ea}NTD subunits are nearly identical, and the intermolecular contacts involving D39 and D40 are highly symmetric (Figure 2.4C). On the other hand, the asymmetric nature of the ^{Nc}NTD dimer is apparent in comparison of the salt bridges involving these residue, with the D39-K65 salt bridge at one end of the dimer and the D40-K65 salt bridge at the other (Figure 2.4B). I believe that the asymmetric nature of these salt bridges is indicative of dimer interface plasticity. The presence of acidic residues at positions 39 and 40 is a highly conserved motif (Figure 2.2E), and it allows for variability in the intermolecular contacts with K65. As mentioned above, mutation of either D39 or D40 results in abolishment of ^{Ea}NTD dimer formation (Schwarze, Zwettler et al. 2013, Kronqvist, Otikovs et al. 2014), even though these residues do not form the short-range salt bridges with K65 as seen in the ^{Nc}NTD. Thus, the ability for electrostatic interactions to form between D39 and D40 with K65 is important for dimer formation, but the plasticity of the dimer interface allows for more than one type of intermolecular interaction (short-range salt bridge vs. long-range electrostatic) to mediate subunit alignment during NTD dimerization.

A novel D17-D53 intramolecular handshake interaction in the N. clavipes NTD

During the structural analysis, I observed a novel intramolecular handshake interaction that takes place between D17 and D53 in one subunit of the ^{Nc}NTD (Figure 1.4A). D17 and D53 are highly conserved as acidic residues among MaSp NTDs; however, this intramolecular handshake interaction was not observed in the ^{Ea}NTD structure because it has a glutamine at position 53 (Figure 2.2E). The D17-D53 handshake appears to have a clear effect on the ^{Nc}NTD subunit topologies. In the subunit in which this interaction is present, H2 tilts closer to H1 than in the subunit in which this interaction is absent (Figure 2.3B). This suggests that the asymmetric nature of the D17-D53 handshake interaction partially accounts for the differing five-helix bundle topologies of the ^{Nc}NTD dimer subunits described above (Figure 2.2C), and by extension, the asymmetric intermolecular interactions observed at the dimer interface (Table

2.2). The potential role that the D17-D53 handshake plays in ^{Nc}NTD dimer formation will be discussed in more detail in Chapters 3 and 4.

Altered arrangement of NTD dimer subunits results in unique intermolecular contacts

For both the ^{Nc}NTD and ^{Ea}NTD, H2, H3, and H5 contain all of the residues involved in intermolecular contacts. As noted above, in the ^{Nc}NTD, H2, H3, and H5 are oriented differently with respect to H1 and H4 for the two subunits of the dimer, whereas for the ^{Ea}NTD, the subunits are virtually identical. Thus, there are unique sets of intermolecular contacts for each of the two structures (Figure 2.5B). Additionally, the dissimilar subunits of the ^{Nc}NTD results in a significant increase in asymmetric contacts (Table 2.3) at the dimer interface (60%; 30 of 50 total contacts) compared to the ^{Ea}NTD (39%; 20 of 52 total contacts). The difference in symmetric contacts correlates with the aforementioned RMSD values for the superimposition of the subunits within each structure, with the ^{Ea}NTD structure appearing to be more symmetric than the ^{Nc}NTD structure in both tertiary structure and intermolecular contacts (Figures 2.2C and 2.4C).

All of the intermolecular contacts were sorted by buried surface area (BSA), and instances in which the BSA for a residue in the ^{Nc}NTD structure was 25 Å^2 greater than the equivalent residue in the ^{Ea}NTD structure were further examined. At the portion of the dimer interface formed by H2 and H3, T47.B, K54.B, and M55.B of the ^{Nc}NTD are significantly more buried than the corresponding S47.A, S54.A, and L55.A residues of the ^{Ea}NTD. These three residues in subunit B of the ^{Nc}NTD contact eight residues (D40.A, T43.A, D46.A, T47.A, I48.A, A51.A, L69.A, and I80.A) in subunit A (Figure 2.5A, top row, left panel), while the equivalent residues in subunit A of the ^{Ea}NTD only contact three residues (T43.B, S51.B, and L55.B) in subunit B (Figure 2.5A, top row, right panel). Some of these differences in contacts may be attributable to a different residue (and therefore, different sidechain) at the specified positions. For example, the lysine at position 54 in the ^{Nc}NTD has a much bulkier side chain than that of the corresponding serine in the ^{Ea}NTD. However, the differences in BSA values, which are due to number and types of contacts being made, are more likely due to the alignment of the dimer interface at this region. The angles at which helices 2 and 3 cross their counter parts in the ^{Nc}NTD and ^{Ea}NTD structures differ by 11.5 and 6.4 degrees, respectively (Figure 2.5A, middle panels) due to the differences in subunit topology discussed above. Additionally, the helices at the dimer interface of the ^{Nc}NTD are in a more parallel alignment than those of the ^{Ea}NTD, which leads to a greater number of intermolecular contacts in this area.

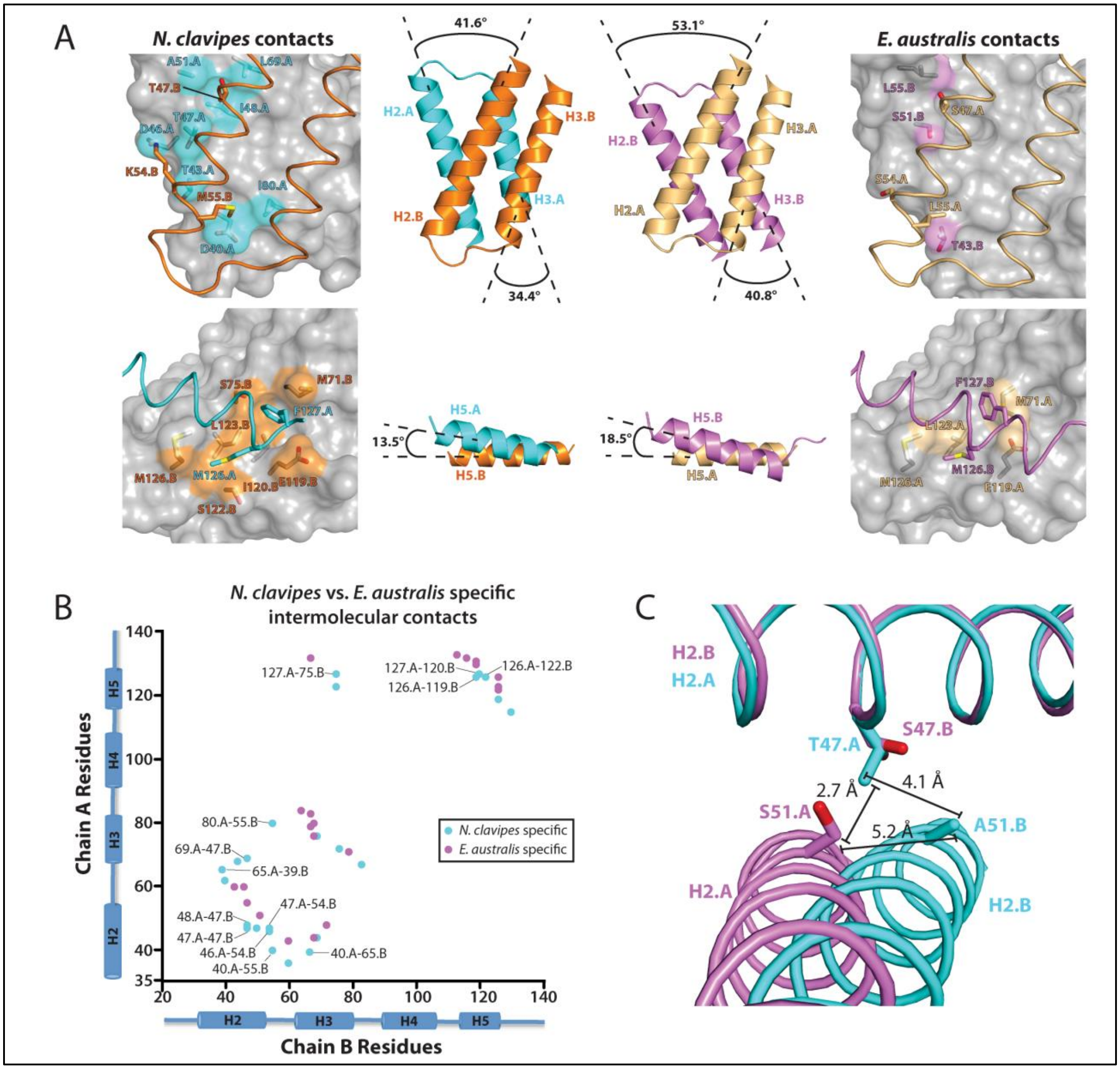

Figure 2.5, Differences in the topology of the subunits at the NTD dimer interface results in unique intermolecular contacts. **(A)** To illustrate the differences in how the interfacial helices are arranged at the dimer interface, I calculated the angles at which H2/H3 (top, middle) and H5 (bottom, middle) cross each other in the ^{Nc}NTD and ^{Ea}NTD structures, which are shown in the same orientation as ribbons. Angles were calculated using the program Chimera. In the left (^{Nc}NTD) and right (^{Ea}NTD) panels, one NTD subunit of each dimer is shown as a transparent gray surface and the other as ribbons. Side chains of residues that engage in novel contacts resulting from the altered interfacial helix topologies are shown as sticks and the surface is colored as in the center panel. Only one side of the dimer interfaces is shown for clarity. **(B)** A protein contact map shows where the unique intermolecular contacts are clustered on the secondary structure elements of the ^{Nc}NTD (cyan) and ^{Ea}NTD (violet) structures. The protein contact maps are restricted to show only unique intermolecular contacts. Residue numbers are indicated on the x and y axes. The secondary structure of the subunits is also shown on the axes to facilitate identification of where the unique contacts are occurring in the context of the structure. Unique contacts that were discussed in the text are indicated with lines and the residue numbers shown. **(C)** The ^{Nc}NTD and ^{Ea}NTD structures were superimposed and are depicted as described in Figure 2.2D. The beta branched side chain of ^{Nc}NTD T47, which is conserved in most MaSp1A orthologs but is a serine in ^{Ea}NTD, can be accommodated as a result of the difference in the topology of the interfacial helices, in particular H2. Distances between atoms discussed in the text are indicated.

The helices at the H2/H3 dimer interface cross at a sharper angle than the helices at the H5 interface. Interestingly, the residues making intermolecular contacts at the point where the H2's cross have distinctly different orientations for the ^{Nc}NTD and ^{Ea}NTD structures. In both structures, residue 47 contacts residue 51, and the contact is symmetric (Figure 2.5C). The angle at which H2A crosses H2B in the ^{Nc}NTD increases the distance between the distal atoms of the T47 and A51 side chains by about 1.5 Å relative to the ^{Ea}NTD, and this subtle shift creates space that is required to accommodate the larger T47 side chain (Figure 2.5C). A threonine at position 47 and an alanine at position 51 are both strictly conserved (Figure 2.2E), except in the *E. australis* sequence. However, if a threonine were to be substituted for the serine in the ^{Ea}NTD, there would be steric clashes due to the proximity of residue 47's C_β to the opposing chain, regardless of the rotamer adopted by either side chain. The ^{Nc}NTD can accommodate a beta-branched amino acid due to the altered helix alignment, suggesting that the helices cross to accommodate the side chains of the residues comprising the dimer interface.

The differences in the intersubunit contacts extend to the H5:H5 interface as well. M126.A and F127.A of the ^{Nc}NTD also had significantly larger BSA values than the corresponding residues M126.B and F127.B of the ^{Ea}NTD. Again, the differences in BSA values is attributed to the difference in the number of contacts the residues are making: in the ^{Nc}NTD, M126.A and F127.A collectively make seven intermolecular contacts (M71.B, S75.B, E119.B, I120.B, S122.B, L123.B, and M126.B) (Figure 2.5A, bottom row, left panel), while M126.B and F127.B collectively make just four intermolecular contacts (M71.A, E119.A, L123.A, and M126.A) in the ^{Ea}NTD (Figure 2.5A, bottom row, right panel). Additionally, in the ^{Nc}NTD, F127.B fits neatly into a pocket formed by M71.A, S75.A, E119.A, and I120.A. However, if subunit B from the ^{Nc}NTD were to replace subunit A in the ^{Ea}NTD, F127 would clash with the residues across the dimer interface. This conflict is interesting, because unlike the aforementioned interface residues in H2, the residues noted here in H5 are strictly conserved. Similar to the H2/H3 interface, the two H5s are more parallel to each other in the ^{Nc}NTD (13.5°) than in the ^{Ea}NTD (18.5°). Thus, the more likely reason for the differences in buried surface area and contacts is the difference in the H5:H5 angle for the two structures.

Conclusions

In this chapter, I have presented the high-resolution crystal structure of the *N. clavipes* MaSp1 NTD dimer, which contains subunits with distinctly different topologies. These differences are due to different arrangements of helices 2, 3, and 5 with respect to helices 1 and 4, which affect intermolecular contacts when compared to previously reported crystal and NMR structures of the *E. australis* NTD (Askarieh, Hedhammar et al. 2010, Kronqvist, Otikovs et al. 2014). The ^{Nc}NTD contains more asymmetric contacts than the ^{Ea}NTD, including the critical interactions involving D39, D40, and K65. In the ^{Nc}NTD, short-range salt bridges form between D39 and K65 on one side of the dimer interface and between D40 and K65 on the other, whereas in the ^{Ea}NTD, D40 and K65 form symmetric, long-range electrostatic interactions on both sides of the dimer interface. Thus, the presence of fully conserved consecutive acidic residues at positions 39 and 40 of major ampullate NTDs allows for plasticity in the interactions these residues engage in depending on precisely how the subunits are arranged at the dimer interface. I also identified a novel intramolecular handshake between conserved acidic residues at positions 17 and 53 that could be part of the pH-dependent dimerization, similar to the role of the D40-E84 handshake observed in the ^{Ea}NTD (Kronqvist, Otikovs et al. 2014), though further studies will be required to test this possibility.

Recently, a “conformational selection” model was proposed in which spidroin NTDs populate many conformations in dynamic equilibrium while in their monomeric state in the high pH conditions of the ampullate gland. Dimerization occurs when an NTD subunit selects a partner with the complementary binding interface from an ensemble of conformers (Ries, Schwarze et al. 2014). The ^{Nc}NTD structure is the first to show two significantly different subunit topologies in one dimer, and the aforementioned dimer interface plasticity could play a role in accommodating the topological differences and regulating the monomer to dimer transition and/or the transition from loosely to stably associated dimer. Thus, the ^{Nc}NTD structure presented here and the previously published spidroin NTD structures (Askarieh, Hedhammar et al. 2010, Jaudzems, Askarieh et al. 2012, Kronqvist, Otikovs et al. 2014) could be on-pathway snapshots of the NTD during the pH-dependent dimerization process that occurs as the spidroins progress through the spinning duct.

Table 2.1, Crystallographic Data and Refinement Statistics.

	N. clavipes MaSp1A NTD
PDB ID	5IZ2
Source	APS 22 ID
Wavelength (Å)	1
Resolution Limits (Å)	58.5-2.02 (2.07-2.02)
Space Group	$P3_121$
Unit Cell (Å) *a, b, c*	67.5, 67.5, 90.4
Number of observations	174181 (12661)
Number of reflections	16120 (1145)
Completeness (%)	98.2 (94.6)
Mean I/σI	21.7 (5.8)
R-merge on I [a]	0.081 (0.60)
Refinement Statistics	
Resolution Limits (Å)	35.7-2.02 (2.09-2.02)
# of reflections (work/free)	15808/1561
Completeness (%)	98.2 (94.6)
Protein/water atoms	1844/120
R_{cryst} [b]	0.164 (0.169)
R_{free} (10% of data)	0.205 (0.233)
Bonds (Å)/ Angles (°)	0.004/0.724
B-factors: protein/water ($Å^2$)	36.7/40.5
Ramachandran plot statistics (%)	
Preferred regions	100
Outlier regions	0
MolProbity score	0.77- 100th percentile (N=12151, 2.02 Å ± 0.25Å)

Parentheses indicate statistics for the high-resolution data bin for x-ray data.

a. $Rmerge = \sum_{hkl} \sum_i |I(hkl)_i - \langle I(hkl)\rangle| / \sum_{hkl} \sum_i \langle I(hkl)_i \rangle$.

b. $Rcryst = \sum_{hkl} |Fo(hkl) - Fc(hkl)| / \sum_{hkl} |Fo(hkl)|$, where Fo and Fc are observed and calculated structure factors, respectively.

Table 2.2, Comparison of intermolecular contacts at the ^{Nc}NTD and ^{Ea}NTD interfaces.

Nc_A	Nc_B
D40	K65
K65	D39
D36	K60
T47	K54
S62	D40
D46	K54
A68	S76
S75	A72
E119	S130
I44	L69
T47	T47
E119	M126
M126	E119
T47	A51
A51	T47
G64	D40
K65	D40
A68	E79
L69	I44
M71	F127
A72	A72
S75	S75
S76	A72
E79	A68
L123	L123
F127	E119
D40	M55
T47	T50
I48	T47
Q67	V83
A68	I44
L69	T47
A72	S76
S76	L69
I80	M55
N115	S130
L123	S75
M126	S122
F127	M71
F127	S75
F127	I120
T43	K54
M55	T43
G64	E84
K65	T43
Q67	E79
A68	I80
E79	M71
E119	F127
M126	L123

Ea_B	Ea_A
T43	R60
S51	S51
S76	A68
S47	S51
S51	S47
E79	Q67
R60	Q46
N133	N113
K65	D39
L55	S47
R60	T43
M71	E79
E84	N64
M126	M126
A130	E119
D40	K65
T43	L55
L55	T43
N64	E84
K65	D40
N67	E79
A68	S76
A68	E79
A68	I80
M71	F127
A72	A72
S75	S75
E79	A68
E79	M71
I80	A68
E119	F127
E119	A130
M126	L123
F127	M71
F127	E119
I44	A68
M48	A72
S83	Q67
Q122	M126
L123	M126
G131	E119
M132	Q67
M132	W10
M132	F116
N133	W10
D134	T8
N64	D40
K65	T43
L69	I44
S75	A72
S76	A72
L123	L123

KEY:

Salt bridges are shaded blue
Hydrogen bonds are outlined in bold
Symmetric contacts are shaded yellow
Unique contacts are colored red

Table 2.3, Summary of intermolecular contacts at the ^{Nc}NTD and ^{Ea}NTD interfaces

^{Nc}NTD Intermolecular Contacts							
		Unique		**Shared**		**Total**	
		Number	%	Number	%	Number	%
All		22	44.0%	28	56.0%	50	100.0%
	Symmetric	4	18.2%	13	46.4%	20	40.0%
	Asymmetric	18	81.8%	15	53.6%	30	60.0%
Involve H2,H3		16	40.0%	24	60.0%	40	80.0%
	Symmetric	2	12.5%	13	54.2%	15	37.5%
	Asymmetric	14	87.5%	11	45.8%	25	62.5%
Involve H5		8	57.1%	6	42.9%	14	28.0%
	Symmetric	2	25.0%	3	50.0%	5	35.7%
	Asymmetric	6	75.0%	3	50.0%	9	64.3%

^{Ea}NTD Intermolecular Contacts							
		Unique		**Shared**		**Total**	
		Number	%	Number	%	Number	%
All		22	42.3%	30	57.7%	52	100.0%
	Symmetric	9	40.9%	23	76.7%	32	61.5%
	Asymmetric	13	59.1%	7	23.3%	20	38.5%
Involve H2,H3		13	32.5%	25	62.5%	38	73.1%
	Symmetric	7	53.8%	19	76.0%	26	68.4%
	Asymmetric	6	46.2%	6	24.0%	12	31.6%
Involve H5		11	78.6%	7	50.0%	18	34.6%
	Symmetric	2	18.2%	6	85.7%	8	44.4%
	Asymmetric	9	81.8%	1	14.3%	10	55.6%

Chapter 3: The Salt- and pH-Dependent Dimer Formation of the ^{Nc}NTD is Governed by Key Salt Bridge and Handshake Interactions

Introduction

As described in Chapter 1, the dimerization of the NTD is crucial for spidroin organization during the silk spinning process, and it is mediated by decreases in both pH and salt concentration (Askarieh, Hedhammar et al. 2010, Gaines, Sehorn et al. 2010, Hagn, Thamm et al. 2011, Kronqvist, Otikovs et al. 2014). Both the ^{Nc}NTD and ^{Ea}NTD form homodimers as the salt concentration decreases, as demonstrated by size exclusion chromatography, pull-down assays, and tryptophan fluorescence assays (Gaines, Sehorn et al. 2010, Kronqvist, Otikovs et al. 2014). It was proposed that the high salt concentration found in the ampullate gland promotes a mostly monomeric population of NTD, because the sodium chloride ions shield the electrostatic interactions between charged residues, which inhibits the formation of intermolecular salt bridges (Gronau, Qin et al. 2013). As the spidroins progress down the spinning duct, the decrease in sodium chloride concentration promotes NTD dimer formation by allowing oppositely charged residues to form intermolecular electrostatic interactions that align the NTD subunits anti-parallel to one another (Gaines, Sehorn et al. 2010). The long-range electrostatic interactions observed in the ^{Ea}NTD crystal and NMR structures (Askarieh, Hedhammar et al. 2010, Kronqvist, Otikovs et al. 2014) and the short-range salt bridges observed in the ^{Nc}NTD crystal structure (described in Chapter 2) support this mechanism. The residues involved in these electrostatic interactions (D39, D40, R60, and K65) are all highly conserved among spidroin NTDs (Gaines and Marcotte 2008, Askarieh, Hedhammar et al. 2010), and mutation of these residues results in abolishment of the ^{Ea}NTD dimer (Schwarze, Zwettler et al. 2013, Kronqvist, Otikovs et al. 2014), suggesting that the charge-mediated alignment mechanism is a necessary part of NTD dimer formation.

The decrease in pH observed in the limbs of the spinning duct (Knight and Vollrath 2001, Dicko, Vollrath et al. 2004, Andersson, Chen et al. 2014) also promotes NTD homodimer formation (Askarieh, Hedhammar et al. 2010, Gaines, Sehorn et al. 2010, Hagn, Thamm et al. 2011). Based on tryptophan fluorescence, urea denaturation, and proton uptake assays, Kronqvist et al. proposed that for the ^{Ea}NTD dimer formation process, the salt-mediated NTD subunit alignment described above alters the local environment of specific charged residues and leads to elevated pKa values of residues E79 and E119. As the pH decreases, both of these acidic residues become protonated, which allows formation of the weakly associated NTD dimer, and the dimer is fully stabilized by subsequent protonation of E84. All of these acidic residues are highly conserved among MaSp NTDs, suggesting that the pH-mediated protonation mechanism is necessary for MaSp NTD dimer formation (Kronqvist, Otikovs et al. 2014). Interestingly, this mechanism was also observed in the *A. ventricosus* MiSp NTD, but the acidic residues involved did not completely correlate with those of the *E. australis* MaSp NTD (Otikovs, Chen et al. 2015). Thus, it is likely that pH-dependent dimer formation is crucial for general spidroin assembly, but the specific acidic residues involved in this mechanism can vary.

The separate but complimentary effects of decreases in salt concentration and pH on NTD dimer formation are apparent, but the specific molecular mechanisms that govern these forces are still not completely understood. Through detailed analysis of the high resolution crystal structure of the ^{Nc}NTD presented in Chapter 2, I identified key residues that appear to be important for dimer formation. In this chapter, I systematically introduced point mutations for these key residues and employed several assays to investigate their effects on ^{Nc}NTD dimer formation. The data confirm the importance of the intermolecular salt bridges (D39-K65 and

D40-K65) and suggest that the novel D17-D53 handshake is important for pH-dependent dimer formation.

Experimental Procedures

Mutagenesis—All point mutations were introduced using PCR-based mutagenesis and sent off-site to confirm the mutations. Primers used for mutagenesis are listed in Table 3.1. Each construct was expressed and purified using the same protocol as for wild type.

Chemical Crosslinking—The BS3 (bis(sulfosuccinimidyl)suberate) (ThermoFisher Scientific) chemical crosslinker (which has an 11.4 Å arm length and covalently binds to lysine side chains) was used to covalently bind the proteins in solution. The crosslinker was incubated with 312.5 µM of protein. For each mutant, a series of crosslinker:protein dilutions ranging from 0:1 to 5:1 molar ratio were used. The reactions were carried out in the pH 7.0, 500 mM and pH 7.0, 50 mM NaCl buffers. After two hours at 4°C, the reactions were quenched by lowering the pH by adding 5 µl of 1 M Tris-HCl (pH 2.8). Each sample was run on an SDS-PAGE gel, and as a control, each gel was washed with 25 mL of fixing solution for 20 minutes, 25 mL of staining solution for 30 minutes, and 25 mL of destaining solution for 16 hours, all at room temperature. Crosslinked dimers survived SDS denaturing, which provided a clear distinction between the monomer and dimer fractions in each reaction. Kodak software was used to image the gel and to calculate the density of the monomer and dimer bands to compare the monomer- and dimer-favoring conditions.

Size Exclusion Chromatography—Size exclusion chromatography (SEC) was used as a low resolution, non-denaturing approach to approximate the molecular weight of the WT NTD in three buffer conditions. To mimic the *in vivo* conditions the proteins experience in the spinning duct, three buffers were created. The monomer-favoring buffer was pH 7.0, 500 mM NaCl, which mimics the ampulle gland. The dimer-favoring buffers were pH 7.0, 50 mM NaCl and pH 5.5, 50 mM NaCl, which mimic the decreases in NaCl and pH as the spidroins are pulled down the duct to be spun into fibers (Knight and Vollrath 2001, Andersson, Chen et al. 2014). All buffers were made using a total of 25 mM of sodium phosphate and citric acid in appropriate ratios to achieve the desired pH. Five hundred or 50 mM NaCl was then added as desired. Purified ^{Nc}NTD was buffer-exchanged to the desired pH and NaCl concentration condition and concentrated to 200 µM. The Superdex 200 10/300 (GE Healthcare) size exclusion column was equilibrated with the desired buffer. Two hundred microliters of protein were injected and passed over the column at a fixed flow rate of 0.15 ml/min. The UNICORN (GE Healthcare) software package was used to observe the elution profiles at each condition and calculate the elution volume of the proteins. Three separate runs were conducted at each condition. To create a calibration curve, the total volume (V_t, 24.0 ml) and void volume (V_o, 7.65 ml) of the column were calculated. Five proteins of known molecular weight were passed over the column (Figure 3.2A), and their individual elution volumes (V_e) were recorded. The partition coefficient, K_{av}, was then calculated for each standard using the equation: $K_{av} = \frac{V_e - V_o}{V_t - V_o}$. The logarithm of the established molecular weight for each standard was then plotted against the K_{av} to generate the calibration curve (Figure 4.2B). The molecular weights (MW), $\log_{10}$[MW], and K_{av} values of each standard are listed in Table 3.2. A linear regression based on these standards was then generated: $K_{av} = -0.3061 \log_{10} MW + 0.6691$. The K_{av} equation and molecular weight standards were provided by GE Healthcare. For each ^{Nc}NTD variant, the K_{av} was calculated using the elution volume and this value was used to calculate the apparent molecular weight. The elution volume for each ^{Nc}NTD variant was collected in triplicate.

Tryptophan fluorescence—Stock buffer solutions were made using a 20 mM MES/20 mM HEPES buffer system to cover the pH range of 5.4-7.4 in 0.2 pH increments. Working buffers were made to contain 154 mM sodium chloride to reflect physiological conditions (Knight and Vollrath 2001). Each mutant was expressed and purified as described in Chapter 2 and was buffer-exchanged to 20 mM Tris-HCl, pH 8.0, 50 mM NaCl then concentrated to 2 mM of protein. Five µl of concentrated protein was mixed with 995 µl of each working buffer, so that the final protein concentration was 10 µM. The resulting 1 ml sample was left at room temperature for 30 minutes to allow the protein to equilibrate. The pH-adjusted samples were transferred to a 1 x 1-cm quartz cuvette and placed in the spectrofluorometer (QuantaMaster 300, Photon Technology International). The samples were excited at 280 nm using a 1-nm bandwidth, and emission spectra were recorded in 1 nm steps between 300 and 400 nm using a 1-nm bandwidth (protocol was adopted from Kronqvist et. al. 2013 (Kronqvist, Otikovs et al. 2014)). The ratio between the signals at 321 nm to 338 nm, which reflects the ratio between monomeric and dimeric NTD, was calculated for each pH step to compare all mutants across the measured pH range. As a control, the buffer for each pH step was excited without protein added to ensure that the measured signals for the protein samples were not artifacts of the buffer components.

Results and Discussion

Electrostatic interactions involving K65 are crucial to ^{Nc}NTD dimerization

It was previously established that the salt-dependent dimerization of the ^{Ea}NTD utilizes electrostatic interactions involving D40 and K65, and mutation of either of these residues resulted in abolishment of dimer formation (Wallace and Shen 2012, Schwarze, Zwettler et al. 2013, Kronqvist, Otikovs et al. 2014). During structural analysis of the ^{Nc}NTD, I identified the D40-K65 intermolecular salt bridge, as described in Chapter 2. To investigate the importance of this electrostatic interaction, charge-swap mutants (D40K and K65E) for each of these residues were generated. Also, despite the differences between the topologies of the ^{Nc}NTD and ^{Ea}NTD dimer interfaces described in Chapter 2, A72 is located at the center of the ^{Nc}NTD dimer interface (similar to the ^{Ea}NTD), prompting us to generate the A72R mutant to introduce two charged, sterically bulky side chains across from each other. Thus, as expected, the A72R mutant has been shown to be monomer-stabilizing despite decreases in salt concentration and/or pH and therefore serves as an adequate monomer control in the assays presented here.

As discussed in Chapter 1, the spidroin NTDs are not known to contain cysteine residues that could covalently link NTD monomers via disulfide bonds (Sponner, Vater et al. 2005, Gao, Lin et al. 2013). Instead, the NTD must form homodimers utilizing the proposed salt- and pH-dependent dimer formation mechanisms. However, the dimerization forces imparted by these mechanisms are not enough to preserve the dimer upon denaturation during SDS gel electrophoresis (Gaines, Sehorn et al. 2010). In an effort to observe the effects of salt concentration on dimer formation, I introduced the BS3 chemical crosslinker to the ^{Nc}NTD in solutions of varying ionic strength. The crosslinker covalently linked ^{Nc}NTD subunits that were already in close proximity due to the dimer-promoting effects of decreased NaCl concentration, and the crosslinked dimers survived SDS denaturing. The monomer and dimer fractions could then be observed via SDS-PAGE. Unsurprisingly, the wild type (WT) ^{Nc}NTD population was more dimeric as more crosslinker was added, even at the high NaCl concentration (Figure 4.1A). Additionally, lowering the ionic strength also promoted increased dimer formation compared to the higher NaCl concentration (Figure 3.1B), which is in agreement with other assays investigating the effects of salt concentration on NTD dimer formation (Gaines, Sehorn et al. 2010, Kronqvist, Otikovs et al. 2014). At both salt concentrations, the A72R mutant displayed a lower dimer population compared to WT, indicating that introduction of the bulky, charged arginine side chain at the center of the dimer interface decreased dimer formation. Interestingly, the mutants intended to disrupt the observed salt bridge interaction (D40K and K65E) did not behave similarly. The D40K behaved essentially the same as WT, while the K65E mutant was significantly more monomer-stabilizing than WT, even at the lower salt concentration. These data could indicate that the D39-K65 salt bridge observed in the ^{Nc}NTD crystal structure could be forming at both ends of the dimer interface to compensate for the disrupted D40-K65 salt bridge in the D40K mutant. Conversely, in the case of the K65E mutant, the negative charge introduced by the glutamate would be repulsive to both D39 and D40.

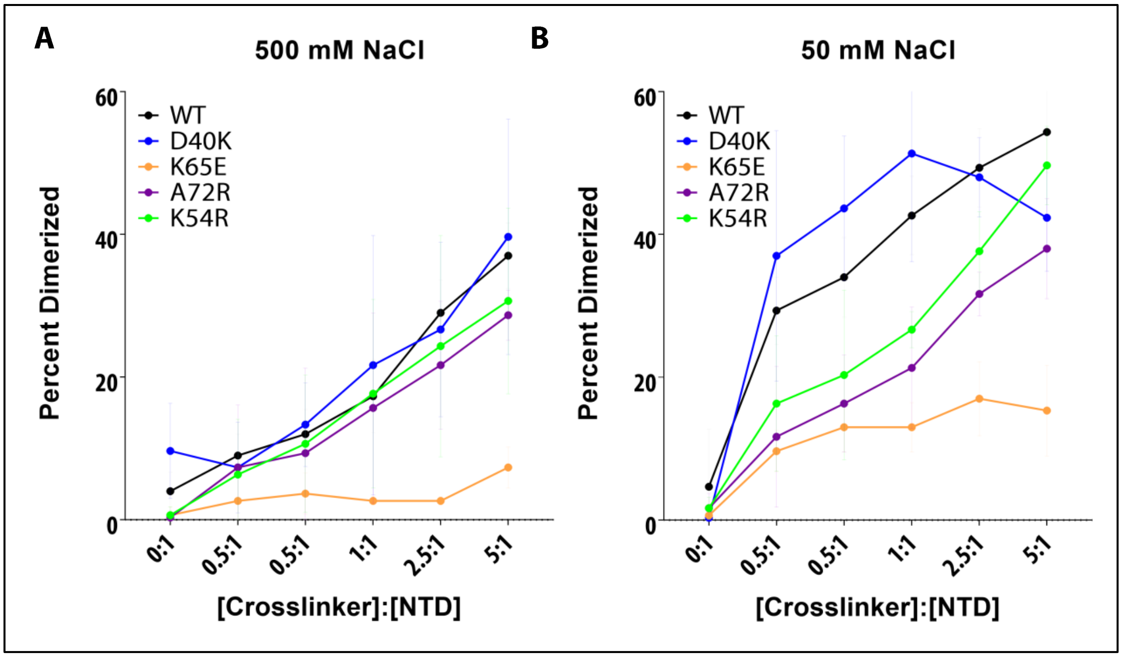

Figure 3.1, K65 is involved in salt-dependent intermolecular electrostatic interactions. The BS3 chemical crosslinker was used to covalently link ^{Nc}NTD monomers together in solution. The molar ratio of crosslinker to ^{Nc}NTD was varied from 0:1 up to 5:1. Each sample was run on an SDS PAGE gel and stained with Coomassie blue in a controlled manner (see Experimental Procedures section). The density of the dimer and monomer bands for each sample was measured, and the percentage of the density of the dimer band out of the total density in each lane is plotted. The assay was performed at pH 7.0, 500 mM NaCl and pH 7.0, 50 mM NaCl. Error bars represent standard error; n=3.

There are two significant drawbacks to this assay. First, because the crosslinking reaction is quenched by lowering the pH of the solution, this assay could only be performed at pH 7, so I could not investigate the effects of the mutations on pH-dependent dimerization. Second, the very nature of the crosslinker itself could explain the results for the D40K and K65E mutants. The BS3 crosslinker covalently binds to lysines, so the introduction of a lysine at position 40 (in the D40K mutant) is in effect providing a new binding site for the crosslinker, especially since D40 is shown to be near several lysine residues (K60, K63, and K65) in the ^{Nc}NTD structure. In this same manner, the K65E mutant is effectively removing a potential BS3 binding site, which could be artificially decreasing the observed percentage of dimer population for this mutant. However, based on the ^{Nc}NTD crystal structure, the only lysine that could potentially form a BS3 crosslink (based on the 11.4 Å arm length of the crosslinker) with K65 is at position 93, and that crosslink would require the BS3 molecule to insert between helices of NTD subunit, which is highly unlikely. Instead, the intermolecular crosslinks most likely involve lysines at positions 49, 54, and 60. Thus, to investigate if the removal of a probable BS3 binding site truly affected dimer formation, the K54R mutant was generated. The lysine to arginine substitution was chosen to retain the positive charge at this position, and lysine 54 was chosen as the residue to mutate because it is near the center of the dimer interface, can form BS3-mediated bonds with K49, K54, or K60 of the opposite NTD subunit, and most importantly, is a non-conserved residue and therefore unlikely to be involved in formation of the NTD dimer. As shown in Figure 3.1, the K54R mutant was less dimer- stabilizing than WT at both salt concentrations (indicating that K54 likely is a BS3 crosslink site), yet still showed a decrease in dimer formation with the decreased ionic strength (although not to the level of the K65E mutant). Thus, the K65E mutant is most likely dimer deficient due to disruption of the salt bridges in which K65 is involved and not because of the loss of a potential crosslinking site.

With the inherent flaws of the crosslinking assay in mind, I employed size-exclusion chromatography (SEC) to verify the salt concentration-induced effects on ^{Nc}NTD dimer formation as well as explore the effects of pH on dimerization. In this assay, the data for the WT ^{Nc}NTD are in close agreement with similar data collected by Gaines et al., in which decreasing both the NaCl concentration and the pH promoted dimer formation of the ^{Nc}NTD (Figure 3.2) (Gaines, Sehorn et al. 2010). At high pH and salt concentration, the elution volume for WT indicated that its apparent molecular weight was approximately 18.7 kDa, which is close to the expected monomer molecular weight of 14.9 kDa. When the NaCl concentration was decreased, the WT was almost completely dimeric, with its elution profile suggesting a molecular weight of 29.9 kDa, which compares favorably with the expected dimer molecular weight of 29.8 kDa.

Decreasing the pH to 5.5 in the presence of 50 mM NaCl did not significantly affect the apparent molecular weight, confirming that within the physiologic pH and salt concentration range, the ^{Nc}NTD does not form higher order oligomers.

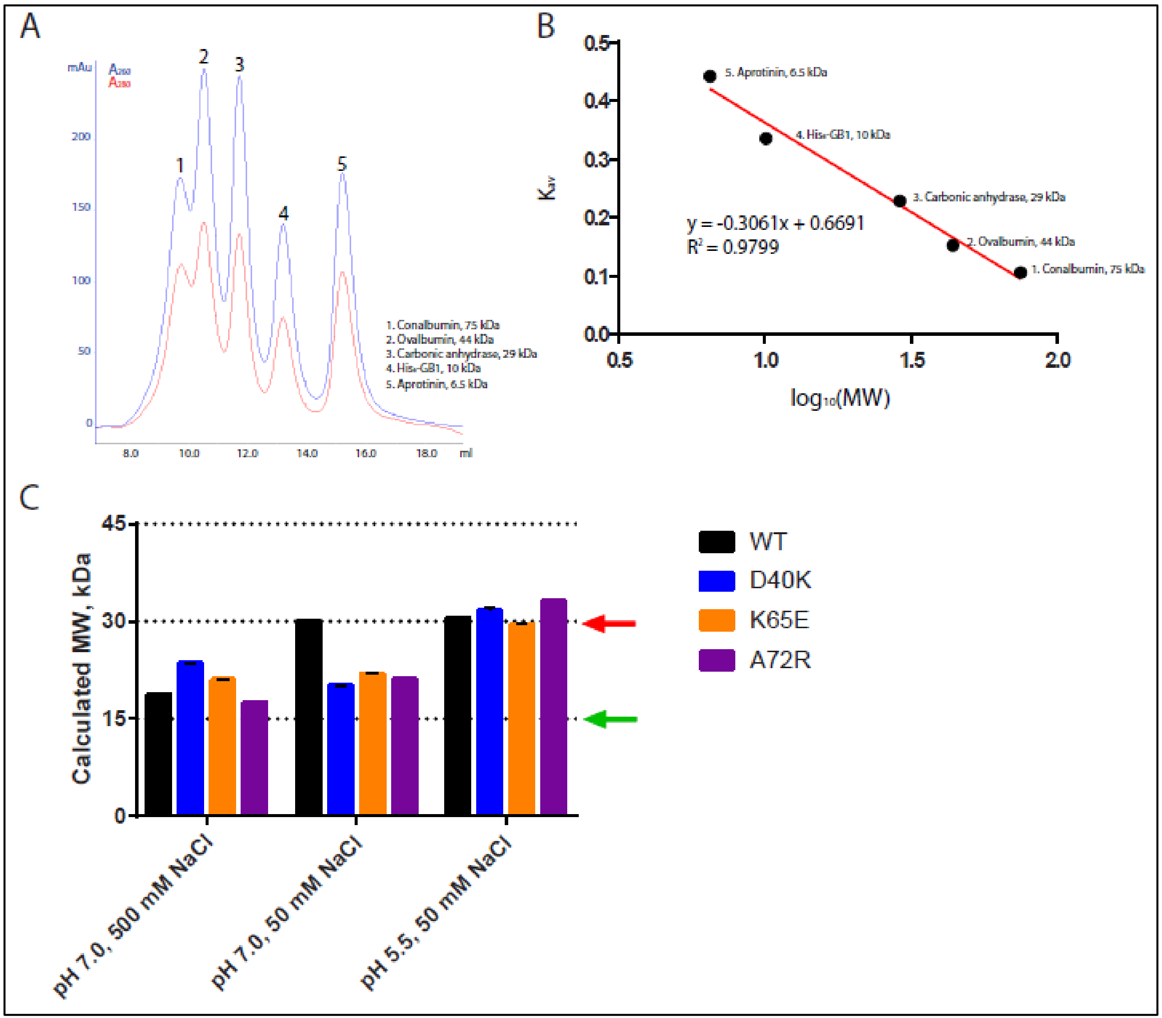

Figure 3.2, D40-K65 salt bridge is crucial to salt-dependent ^{Nc}NTD dimerization. (A) The five molecular weight standards (1. conalbumin, 2. ovalbumin, 3. carbonic anhydrase, 4. H_6-GB1, and 5. aprotinin) were passed over the SEC column and their elution volumes were recorded. **(B)** A calibration curve was generated by plotting the calculated K_{av} of each standard (see Experimental Procedures section) against logarithm of its established molecular weight. **(C)** Each ^{Nc}NTD variant was eluted in the monomer-favoring buffer (pH 7.0, 500 mM NaCl) and the two dimer-favoring buffers (pH 7.0, 50 mM NaCl and pH 5.5, 50 mM NaCl), and the molecular weight for each variant was calculated using its observed elution volume as described in the Experimental Procedures section. The green and red arrows indicate the predicated monomer and dimer molecular weights of 14.9 and 29.8 kDa, respectively. Error bars represent standard error; n=3.

In comparison to WT, the D40K and K65E mutants did not form dimers upon decreasing the NaCl concentration of the buffer from 500 to 50 mM, which confirms that the salt bridge formed between these residues is necessary for salt-dependent dimer formation (Wallace and Shen 2012). However, when the pH was lowered to 5.5, both of these mutants eluted at volumes that indicated NTD homodimer formation. Thus, it is possible that the mechanisms that govern pH-dependent dimer formation are strong enough to overcome the theoretical charge repulsion introduced by the mutations, or that other electrostatic interactions, such as the D39-K65 salt bridge observed in the ^{Nc}NTD structure, can compensate for the disrupted D40-K65 salt bridge. Interestingly, the A72R mutant also formed dimers at the lower pH condition, perhaps indicating that the ^{Nc}NTD can still form dimers through the aforementioned salt- and pH-mediated mechanisms despite the steric clash introduced by the mutation.

In summary, the size exclusion assay confirmed the salt- and pH-dependent dimerization of the WT and also highlighted the importance of the D40-K65 salt bridge with regards to subunit alignment in low ionic strength conditions. However, this assay was less clear in explaining the specific mechanisms of the pH-dependent NTD dimer formation, prompting the pursuit of other methods of investigating this crucial part of the silk spinning process.

Novel intra- and intermolecular interactions are involved in ^{Nc}NTD dimerization

While size exclusion chromatography was useful in confirming that decreasing the pH induced ^{Nc}NTD dimer formation, it only provided quaternary structural information for the start and end points of the physiologic pH range. Thus, I used a tryptophan fluorescence assay to obtain a more nuanced understanding of the role that the residues involved in the key handshake and salt bride interactions in the ^{Nc}NTD structure play in the pH-dependent dimerization process.

This assay was developed and has routinely been used by groups studying spidroin NTDs (Askarieh, Hedhammar et al. 2010, Gaines, Sehorn et al. 2010, Kronqvist, Otikovs et al. 2014, Otikovs, Chen et al. 2015). It has been shown that in the ^{Ea}NTD, during the monomer-to-dimer NTD transition, highly conserved W10 undergoes a conformational change that increases its solvent exposure and results in quenching of its intrinsic fluorescence emission (Askarieh, Hedhammar et al. 2010, Kronqvist, Otikovs et al. 2014). Similar to the ^{Ea}NTD, the ^{Nc}NTD also harbors a tryptophan at position 10 (Figure 3.2E), and this residue is expected to behave similar to its counterpart in the ^{Ea}NTD during pH-dependent dimerization (Gaines, Sehorn et al. 2010).

The pH-dependent dimerization of the ^{Nc}NTD was explored by exciting the samples at 280 nm and recording their emission spectra between 300-400 nm from a pH range of 7.4 to 5.4. The ratio between the fluorescence intensity at 321 nm to 338 nm at each pH step represents the ratio of the ^{Nc}NTD in its monomeric and dimeric states, respectively (Figure 3.3). The WT ^{Nc}NTD behaved as expected (Gaines, Sehorn et al. 2010), with the monomer to dimer transition point at ~pH 6.1 (Figure 3.4A). The A72R mutant remained monomeric throughout the pH range, which is in agreement for similar data for the ^{Ea}NTD A72R mutant (Jaudzems, Askarieh et al. 2012).

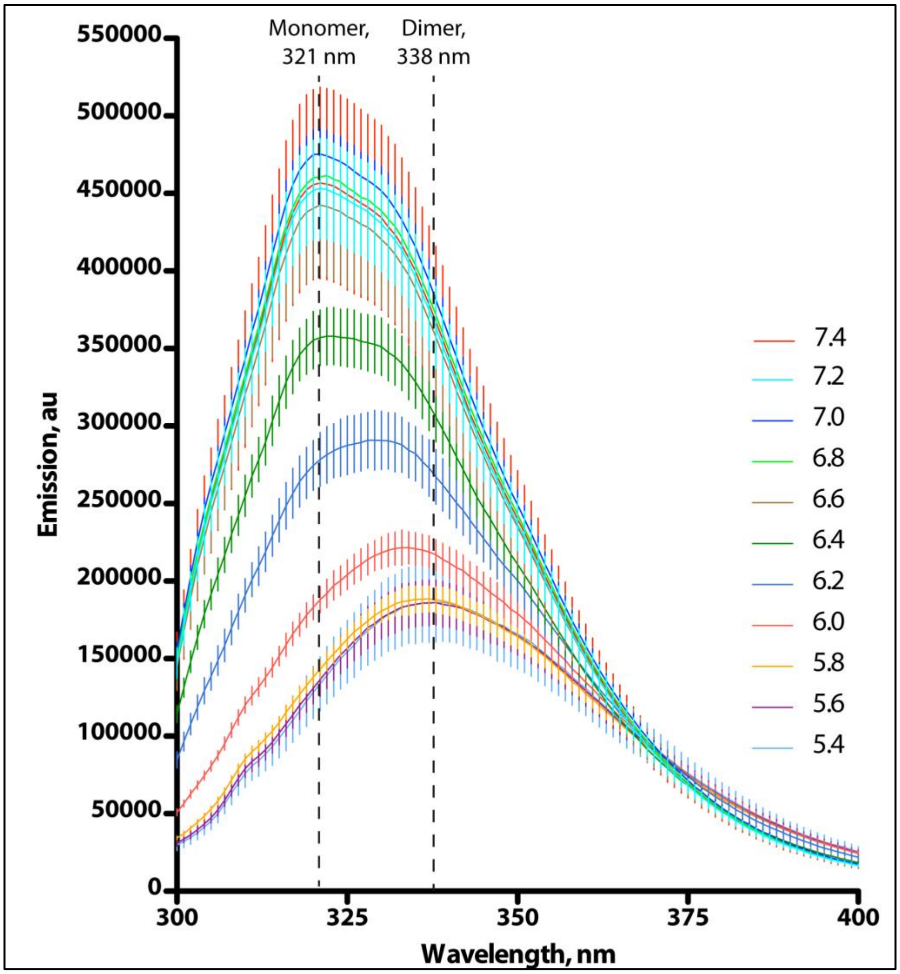

Figure 3.3, Tryptophan fluorescence raw data. Each protein sample was excited at 280 nm and the emission spectra were recorded from 300-400 nm in 1 nm steps for each pH. The signal at 321 nm corresponded to the monomer state, and the signal at 338 nm corresponded to the dimer state. The ratio of these two signals was used to compare the WT and mutants at each pH step. Three replicates were collected at each pH increment for each mutant and error bars correspond to standard error.

The mutations designed to disrupt the intermolecular electrostatic contacts (D39A, D39K, D40A, D40K, and K65E) all shifted the monomer to dimer transition point to a lower pH, indicating a more stable monomer, albeit to different degrees (Figure 3.4A). The D40K mutant resembled the A72R mutant as it was completely monomeric throughout the pH range. The D39K mutant only began to show a transition towards dimer formation at the lowest pH steps, and a fully stable dimer was not achieved. These data suggest that both the D39-K65 and D40-K65 salt bridges are necessary for dimer formation. The D39A and D40A mutants were both more dimer destabilizing compared to WT, but not to the extent of the D39K and D40K mutants.

Taken together, these data indicate that replacement of either conserved aspartic acid residue with a lysine residue most likely results in both an electrostatic and steric clash with K65. When either acidic residue is replaced with an alanine, the dimer destabilizing effect is lessened, most likely because K65 can still form a compensatory salt bridge with the non-mutated acidic residue. These data directly support the previously described dimer plasticity model, in which either conserved consecutive acidic residue D39 or D40 can still form a short-range salt bridge or long-range electrostatic interaction to form with K65, regardless of differences in subunit topology (^{Nc}NTD vs. ^{Ea}NTD) or presence of a non-acidic residue at either position.

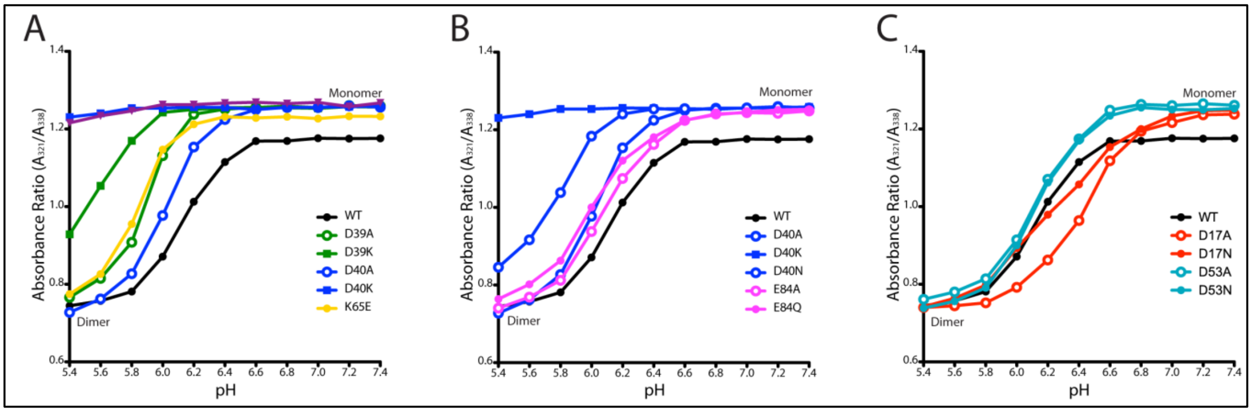

Figure 3.4, Structure-function analysis of residues involved in ^{Nc}NTD dimerization. During transition of the NTD from monomer to dimer, the single tryptophan residue of the NTD (W10) undergoes a conformational change that increases its solvent exposure and results in quenching of its intrinsic fluorescence emission. The ratio of the tryptophan fluorescence signals at 321 nm to 338 nm reflects the ratio between monomeric (338 nm) and dimeric (321 nm) NTD. The tryptophan fluorescence ratio of the signals at 321 nm and 338 nm was plotted as a function of pH for **(A)** WT, A72R, and mutants intended to affect the D39-K65 and D40-K65 salt bridges, **(B)** mutants probing

Interestingly, disrupting the salt bridge via opposite charge swapping from the lysine end (the K65E mutant) was not as dimer destabilizing as from the acidic end (the D39K and D40K mutants); perhaps other basic residues near K65, such as K60 or K63, can form compensatory long-range electrostatic interactions with D39 and/or D40, and this mechanism can be further probed by generating double- or triple-point mutants to charge-swap these residues. Overall, the data agree with tryptophan fluorescence assay results for the ^{Ea}NTD, in which disruption of the D40-K65 salt bridge highly favors the monomer conformation (Kronqvist, Otikovs et al. 2014).

the D40-E84 handshake interaction, and **(C)** mutants probing the D17-D53 handshake interaction. Experiments were performed in triplicate and representative raw data are shown in Figure 3.3.

The mutations designed to affect the D40-E84 handshake (D40A, D40N, E84A, and E84A) also all resulted in transition points occurring at a lower pH than WT (Figure 3.4B). The effects of the protonation-mimic mutants (D40N and E84Q) closely resemble the results from the same mutations in the ^{Ea}NTD (Kronqvist, Otikovs et al. 2014), with the D40N mutation having a greater dimer destabilizing effect than E84Q. The larger degree of dimer disruption for D40N is most likely due to D40's involvement in both the salt bridge with K65 and the handshake with E84. The D40A, E84A, and E84Q all destabilize the dimer to approximately the same degree, suggesting they all disrupt the D40-E84Q handshake in a similar manner and that this handshake serves a similar purpose in pH-dependent dimerization in both NTD species.

The most surprising results involve the mutations designed to affect the D17-D53 handshake (D17A, D17N, D53A, and D53N) (Figure 3.4C). Neither mutation of D53 affected the dimer stability compared to WT, while D17A and D17N had opposing effects on dimer formation. D17N destabilized the dimer, while D17A facilitated dimer formation at a higher pH compared to WT. The charge of the residue has an effect on dimer stability, but the mechanisms that explain this effect are unclear and will be explored in greater detail in the following chapter.

Conclusions

The biochemical data presented in this chapter confirm that the novel intra- and intermolecular interactions observed in the ^{Nc}NTD crystal structure are all necessary for the ^{Nc}NTD dimerization process. The asymmetric D39-K65 and D40-K65 salt bridges observed in the crystal structure are all critical to ^{Nc}NTD dimer formation, as mutation of the residues involved in these interactions all decrease dimer formation. These data are in agreement with data collected for the ^{Ea}NTD (Schwarze, Zwettler et al. 2013, Kronqvist, Otikovs et al. 2014), and more importantly, they underscore the importance of intermolecular electrostatic interactions for salt- and pH-dependent NTD dimerization. The concept of plasticity at the ^{Nc}NTD dimer interface (discussed in Chapter 2) is strengthened by the fact that the D39A and D40A mutants were not as dimer destabilizing as the D39K and D40K mutants.

The conflicting pH-dependent dimerization results for the D40K and K65E between the SEC and tryptophan fluorescence assays can be partially explained by a key feature of the experimental designs. The protein used in the SEC experiments was 20 times more concentrated that that used for the tryptophan fluorescence assay (200 µM vs. 10 µM), which could have increased dimer population regardless of the mutations that were introduced. This condition could actually have some relevance to the *in vivo* silk spinning process, in which the spidroins are stored at extremely high concentrations in the ampullate gland yet do not prematurely aggregate (Chen, Knight et al. 2002) until they experience concomitant decreases in salt concentration and pH in the spinning duct (Knight and Vollrath 2001). Perhaps the high NTD concentrations used in the SEC experiments approximate the *in vivo* spidroin concentrations, and the combination of compensatory long-range electrostatic interactions and pH-dependent dimerization mechanisms can overcome the disrupted salt bridges (D40K or K65E) or sterically unfavorable side chains (A72R) at low pH and salt concentrations. In this same manner, the ^{Nc}NTD was not at high enough concentration in the tryptophan fluorescence assay for the cumulative effect of these mechanisms to overcome the dimer destabilizing effects of the point mutations.

The novel D17-D53 handshake observed in the ^{Nc}NTD crystal structure also affects the pH-dependent dimerization, although the specific mechanisms involved are still unknown. As described in Chapter 1, pH-sensitive relays that involve the protonation of multiple acidic residues have been shown to facilitate dimer formation in spidroin NTDs (Kronqvist, Otikovs et al. 2014, Otikovs, Chen et al. 2015). It is possible that the D17-D53 handshake could play a similar role as the D40-E84 handshake in the pH-dependent dimerization of the ^{Nc}NTD, although further experiments will be necessary to completely elucidate the roles of these residues in such a mechanism.

Table 3.1, Additional Primers Used for Site-Directed Mutagenesis

Mutant	Forward Sequence	Reverse Sequence
WT	*Received construct from Marcotte Lab	
D17A	gtcaagtacggaactagcagctgcattcattaatgcattcatg	catgaatgcattaatgaatgcagctgctagttccgtacttgac
D17N	gtcaagtacggaactagcaaacgcattcattaatgcattcatg	catgaatgcattaatgaatgcgtttgctagttccgtacttgac
D39A	ttactgcggatcaacttgctgatatgtctaccatcgg	ccgatggtagacatatcagcaagttgatccgcagtaa
D39K	ttactgcggatcaacttaaagatatgtctaccatcgg	ccgatggtagacatatctttaagttgatccgcagtaa
D40A	ctgcggatcaacttgatgctatgtctaccatcggagacac	gtgtctccgatggtagacatagcatcaagttgatccgcag
D40K	*Received construct from Marcotte Lab	
D40N	ctgcggatcaacttgataacatgtctaccatcggagacac	gtgtctccgatggtagacatgttatcaagttgatccgcag
D53A	gacacaattaaaacggcgatggccaaaatggcgagaagcaacaag	cttgttgcttctcgccattttggccatcgccgttttaattgtgtc
D53N	gacacaattaaaacggcgatgaacaaaatggcgagaagcaacaag	cttgttgcttctcgccattttgttcatcgccgttttaattgtgtc
K54R	cacaattaaaacggcgatggacgcaatggcgagaagcaacaagagttc	gaactcttgttgcttctcgccattgcgtccatcgccgttttaattgtg
R57A	cggcgatggacaaaatggcggcaagcaacaagagttcaaaagg	ccttttgaactcttgttgcttgccgccattttgtccatcgccg
K65E	gagttgcaagctcttaacatggc	tccttttgaactcttgttgcttc
A72R	cgtttcgcttcatcaatggcg	catgttaagagcttgcaactttcc
E84A	ggcggaaattgctgcagtagcacaaggaggtttaagtgtag	ctacacttaaacctccttgtgctactgcagcaatttccgcc
E84Q	ggcggaaattgctgcagtacaacaaggaggtttaagtgtag	ctacacttaaacctccttgttgtactgcagcaatttccgcc

Table 3.2, Protein Standards Used for SEC Calibration Curve

Standard	MW (kDa)	$\log_{10}$(MW)	K_{av}
Conalbumin	75	1.8751	0.1062
Ovalbumin	44	1.6435	0.1525
Carbonic Anhydrase	29	1.4624	0.2285
H_6-GB1	10	1.0043	0.3356
Aprotinin	6.5	0.8129	0.4419

Chapter 4: Analysis of ^{Nc}NTD Mutants and the Importance of the Novel D17-D53 Handshake

Introduction

The high resolution ^{Nc}NTD crystal structure provided the first known instance of a handshake interaction between residues D17 and D53 in a MaSp NTD. As shown in Chapter 3, this interaction is asymmetric in the ^{Nc}NTD (it only occurs in subunit A), which could be a consequence of the difference in the way the helices are arranged within each subunit (Figure 2.3B). These rearrangements affect the dimer interface, which contributes to the asymmetry of the intermolecular contacts. Sequence homology analysis shows that acidic residues at positions 17 and 53 are highly conserved (Figure 3.2E), except in the ^{Ea}NTD, which contains a glutamine at position 53. As Kronqvist et al. demonstrated, the D40-E84 handshake interaction in the ^{Ea}NTD facilitates the pH-dependent protonation of E84, which is a critical for the transition from weakly to stably associated NTD dimers (Kronqvist, Otikovs et al. 2014). In the ^{Nc}NTD, it is possible that the novel D17-D53 handshake interaction could serve a similar purpose as the D40-E84 mutant. To examine this, I generated point mutants to probe the role that this handshake has on ^{Nc}NTD pH-dependent dimer formation. The data from the tryptophan fluorescence assay for these mutants (Figure 3.4C) demonstrated that disruption of this interaction via the D17A mutant significantly stabilized the monomer.

The D17-D53 handshake interaction is clearly important for ^{Nc}NTD dimer formation, necessitating further investigation of its role in this process. During refinement of the WT ^{Nc}NTD structure, I noticed that R57 from the asymmetric unit seemed to be making crystal contacts with the D17-D53 handshake interaction. To confirm that the D17-D53 handshake interaction was not an artifact of crystal packing, I generated the R57A mutant. In this chapter, I present the R57A crystal structure, solved to 2.2 Å resolution, and investigate its effects on pH-dependent dimerization utilizing the tryptophan fluorescence assay. I also present the crystal structure of the D17A mutant, solved to 1.7 Å resolution and compare its structure to that of the WT ^{Nc}NTD. The biochemical data confirm the legitimacy of the D17-D53 handshake interaction, as well as its importance in the pH-mediated dimerization of the ^{Nc}NTD, and the structural comparisons grant further support to the dimer interface plasticity and conformational selectivity concepts discussed in Chapter 2.

Experimental Procedures

X-ray crystallography—The D17A and R57A mutants were purified as described in Chapter 2 and concentrated to 10.1 mg/ml for D17A and 40.3 mg/ml for R57A in a buffer containing 20 mM Tris pH 8.0 and 50 mM NaCl. The Index (Hampton Research) and JCSG Core I, II, III, and IV (Qiagen) commercial screens were used for sparse-matrix screening in 96-well Greiner microplates (400 nl sitting drop vapor diffusion format) to identify conditions suitable for crystal growth. The Crystal Gryphon robot (Art Robbins Instruments, Asbach, Germany) was used to set these trays. Diffraction quality crystals were grown by manually mixing 1.0 µl of protein with 1.0 µl of well solution by hanging drop vapor diffusion at 18°C.

For the R57A mutant, the well solution contained 0.1 M sodium acetate trihydrate pH 4.5 and 25% PEG 3,350. Crystals formed within 1-2 days and were harvested by flash freezing in liquid nitrogen in mother liquor plus 10% ethylene glycol as a cryoprotectant. The protein crystallized in the $P3_121$ space group with unit cell dimensions a=67.2, b=67.2, and c=89.8, which was identical to the WT protein. There was one copy of the NTD dimer in the asymmetric unit and the crystal had an estimated solvent content of 37.4%.

For the D17A mutant, the well solution contained 0.2 M ammonium acetate, 0.1 M BIS-TRIS pH 5.5, and 21% w/v PEG 3,350. Crystals formed within 1-2 days and were harvested by flash freezing in liquid nitrogen in mother liquor plus 10% ethylene glycol as a cryoprotectant. The protein crystallized in the P_1 space group with unit cell dimensions a=35.9, b=41.0, and c=46.4. There was one copy of the NTD dimer in the asymmetric unit and the crystal had an estimated solvent content of 38.1%. Diffraction data sets for both mutants were collected on the Southeast Regional Collaborative Access Team (SER-CAT) 22-ID beamline at the Advanced Photon Source, Argonne National Laboratory. All data were indexed, integrated, and scaled using HKL2000 (Otwinowski and Minor 1997).

Structure determination and refinement—Data sets were collected to resolutions of 2.2 and 1.7 Å for the R57A and D17A mutants, respectively. In each case, the structure of the WT ^{Nc}NTD (PDB: 5IZ2) was used as the model for molecular replacement using the PHASER software (McCoy, Grosse-Kunstleve et al. 2007). The models were refined to R_{cryst}/R_{free} values of 0.191/0.249 and 0.136/0.164 for R57A and D17A, respectively by iterative refinement using PHENIX (Adams, Afonine et al. 2010) and COOT (Emsley 2013) software. For the R57A mutant, the final model contains residues 7-83 and 88-128 in Chain A and residues 9-56 and 62-130 in Chain B. Similar to the WT crystal structure (see Chapter 2), Chain Z was built as the residues SYG which are mostly likely residues 136-138 of chain A. For the D17A mutant, the final model contains residues 7-125 in chain A and 7-129 in chain B. No evidence of residues 136-138 was observed. The detailed data collection and refinement statistics for both mutants are listed in Table 4.1. Molecular graphics representations were generated using PYMOL

(Schrodinger 2015) and the CCP4mg program of the CCP4 6.4.0 software suite (Winn, Ballard et al. 2011).

Results and Discussion

The D17-D53 handshake interaction is not an artifact of crystal packing

Structural analysis of the WT ^{Nc}NTD crystal structure revealed the D17-D53 handshake interaction, but the side chain of R57.Ax of one of the symmetry-related molecules was possibly also interacting with these acidic residues (Figure 4.1A). To ensure that the D17-D53 handshake interaction was not an artifact of crystal packing, I generated the R57A mutant and also solved its crystal structure to 2.2 Å resolution (Table 4.1). The R57A mutant crystallized in the same $P3_121$ space group as WT and contains subunits of differing helical arrangements, also similar to WT (Figure 4.1B). The R57A and WT structures superimpose with an RMSD of 0.270 Å (Figure 4.1C), with the only notable differences being slightly more disordered termini and the disordered loop containing residues 57-61 in subunit B in the R57A structure.

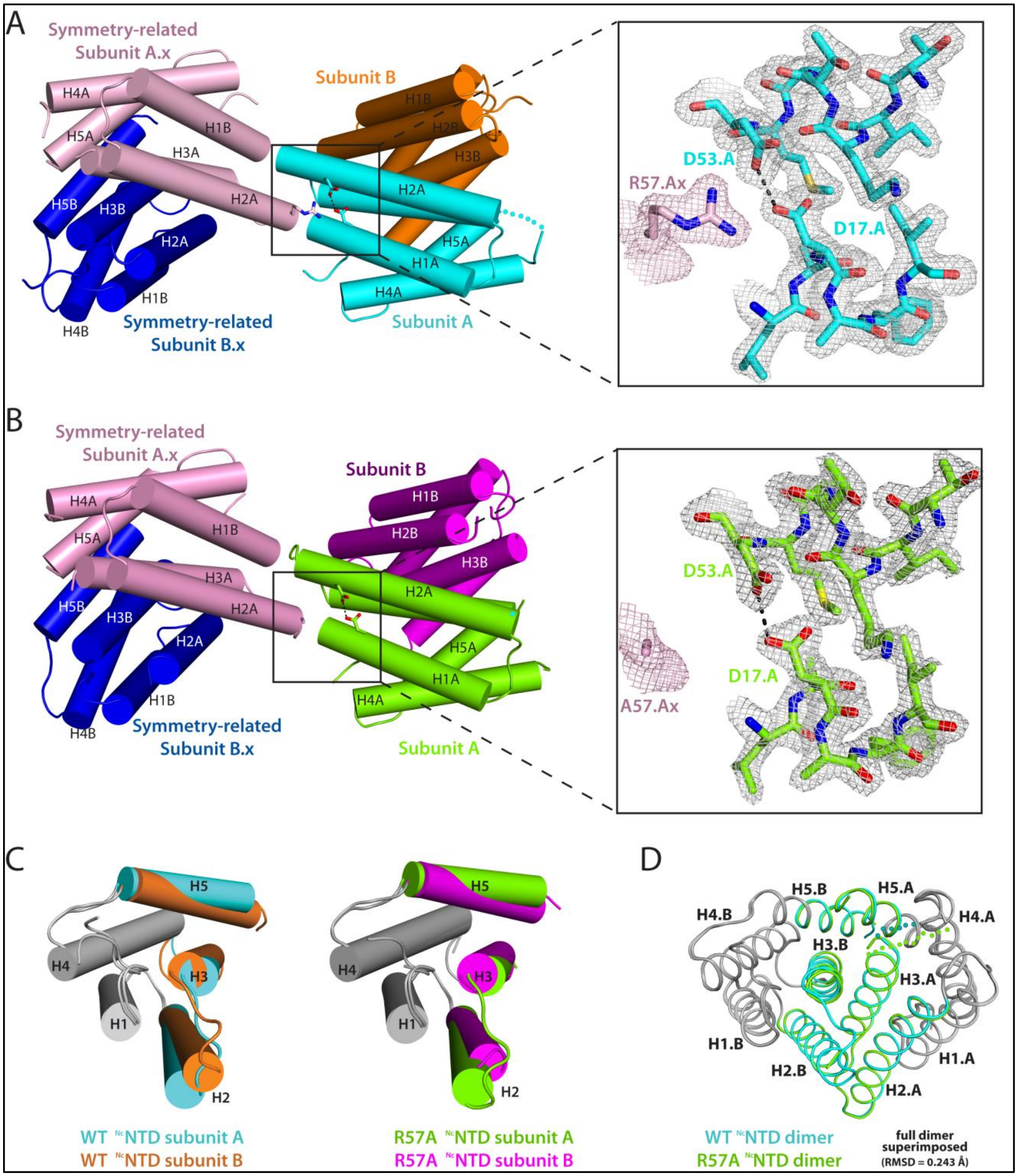

Figure 4.1, WT and R57A ^{Nc}NTD crystal structures are highly similar. (A) For the WT ^{Nc}NTD, Subunits A.x (pink) and B.x (blue) form the dimer of one symmetry-related molecule. R57.Ax makes a crystal contact with D17.A and D53.A and could be facilitating the handshake interaction between these residues. 2.2 Å 2|Fo|-|Fc| electron density map (contoured at 1.5σ) for this interaction is shown. **(B)** For comparison, for the R57A mutant, Subunits A.x (pink) and B.x (blue) of the symmetry-related molecule are shown again. The handshake interaction between D17.A and D53.A is identical to the equivalent interaction in the WT ^{Nc}NTD despite the absence of the crystal packing interaction with A57.x. The electron density maps (sigma cutoff = 1.5 σ) for this interaction are shown **(C)** The subunits of the WT (left) and R57A (right) structures were superimposed to highlight the topology of the helices comprising the five-helix bundles. Note that for both structures, H2, H3, and H5 are oriented differently to H1 and H4 across the two subunits of each of the ^{Nc}NTD dimers. (**D**) Comparison of the overall WT and R57A structures. Chain B from the WT was superimposed with chain B of R57A as these were the subunits that were most similar to each other. Note that the structures are essentially identical.

The overall crystal structures for WT and R57A are virtually identical, and thus, unsurprisingly, the R57A mutant displayed the same asymmetric salt bridge and handshake interactions as WT. Using the same nomenclature described in Chapter 2, I designated the two ends of the dimer as the ‘front’ and ‘back’ sides. On the front side of the dimer, D40 and E84 engage in the intramolecular handshake interaction as observed in the WT structure, and an intermolecular salt bridge forms between D39 and K65 (Figure 4.2A). On the back side of the dimer, the loop containing E84 is disordered, D40 forms an intermolecular salt bridge with K65, and D39 is not involved in intermolecular contacts. Also, similar to WT, the D17-D53 handshake only occurs in one subunit (subunit A) and is partly responsible for the differing subunit topologies (Figure 4.2B). In subunit B, the D17 and D53 side chains are oriented as if to form a handshake interaction, but the nearest oxygen atoms of these side chains are 4.3 Å apart. The interacting oxygen atoms of the handshake interactions seen in the WT ^{Nc}NTD and ^{Ea}NTD (Askarieh, Hedhammar et al. 2010) are all 2.6-2.7Å apart, suggesting that the orientation of the D17 and D53 side chains observed in subunit B of the R57A structure does not designate a true handshake interaction. Also unsurprisingly, the R57A mutant displayed the same pH-dependent dimerization profile as WT (Figure 4.2C). It should be noted that R57 is not well-conserved among MaSp NTDs (Figure 2.2E) and thus, is not expected to be critical to NTD dimer formation. Cumulatively, the crystal structure and biochemical data for the R57A mutant confirm that the D17-D53 handshake interaction is not a result of crystal packing and is relevant to the pH-dependent dimerization mechanism of the ^{Nc}NTD.

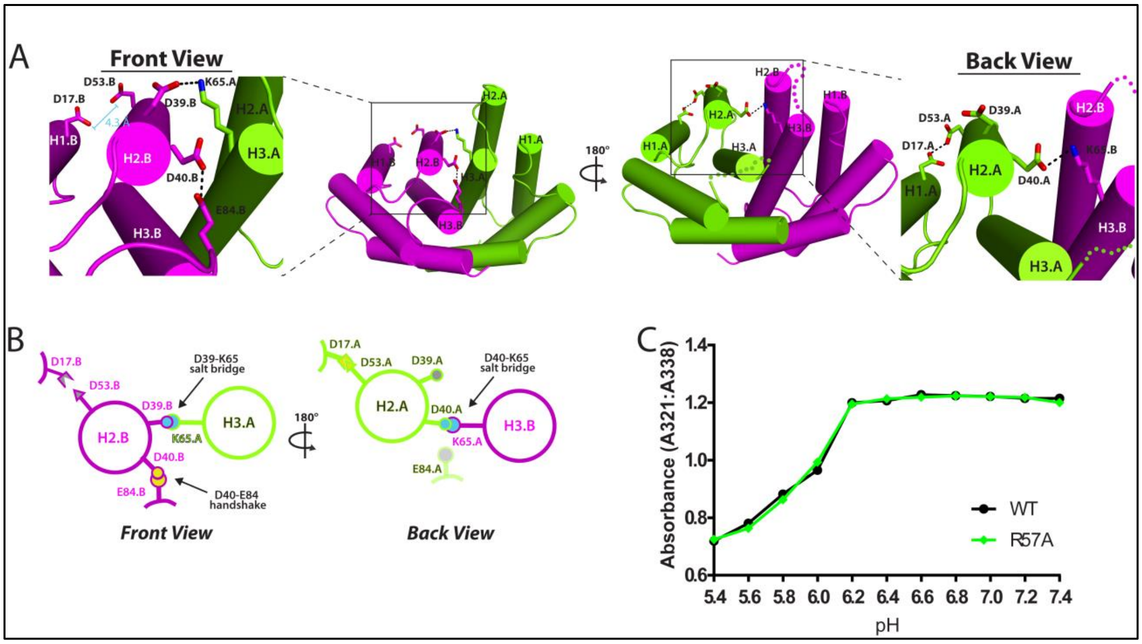

Figure 4.2, R57A mutant displays conserved intra- and intermolecular interactions important for ^{Nc}NTD dimerization. (A) Front and back views of the R57A dimer reveals differences in the pattern of key salt bridge and handshake interactions taking place between equivalent residues on the two dimer subunits. **(B)** Cartoon schematics illustrating key intra- and intermolecular interactions at the WT and R57A ^{Nc}NTD dimer interfaces are conserved. **(C)** Tryptophan fluorescence data shows that the R57A mutation does not affect pH-dependent dimerization compared to WT.

D17A crystal structure contains subunits of similar topologies

Interestingly, of all the point mutations generated for the ^{Nc}NTD, D17A is the only mutant that appeared to stabilize the dimer at a higher pH compared to WT, regardless of the salt concentration. Thus, to gain a better understanding of the effects of this mutation on the pH-dependent dimerization mechanism, I solved the D17A crystal structure to 1.7 Å resolution. In comparison to the WT structure, the D17A structure displays the same dimer conformation consisting of two subunits each adopting the canonical five-helix bundle shape (Figure 4.3A). However, unlike the WT and R57A structures described above, the topologies of the two subunits within the D17A dimer superimpose better than those of the WT dimer (Figure 4.3B). With helices 1 and 4 acting as a rigid body, helices 2 and 3 appear to be more aligned with their counterparts in the opposite subunit as compared to the WT structure. This difference in subunit topology appears to be influenced by the presence or absence of the D17-D53 handshake.

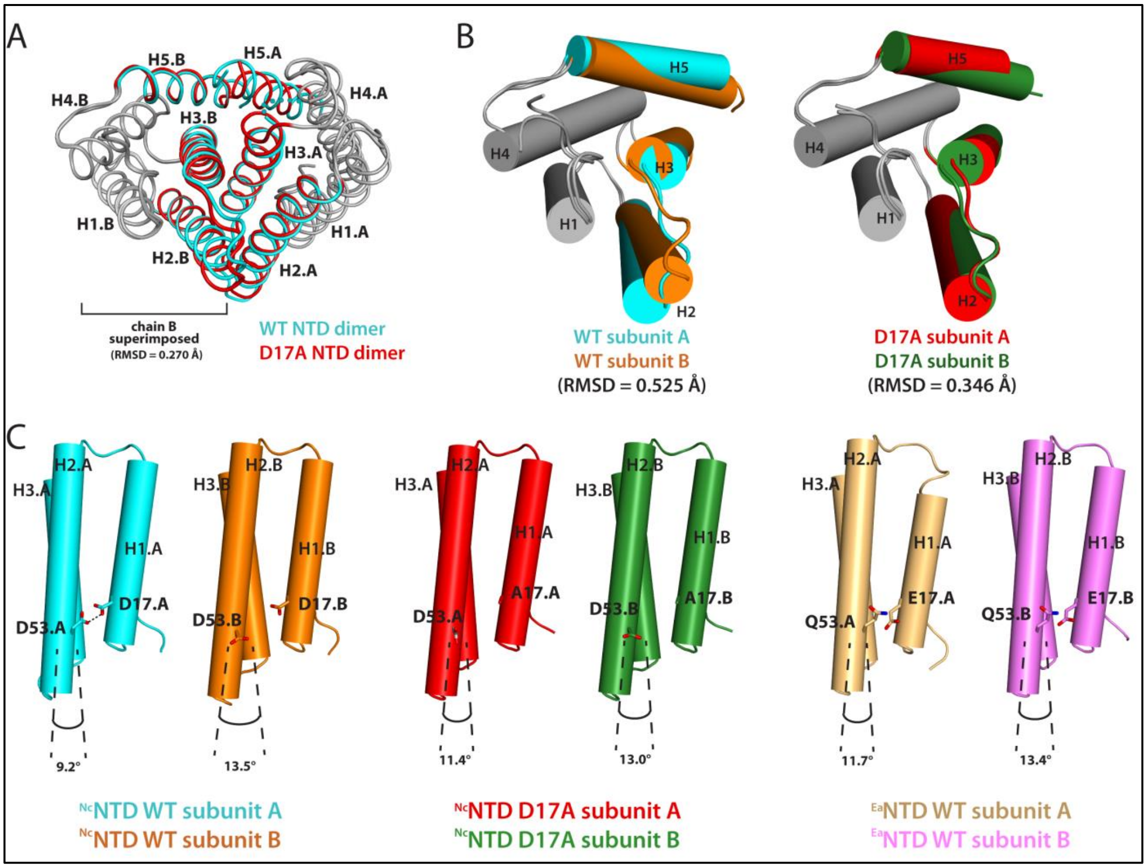

Figure 4.3, Comparison of subunit topologies of NTD structures. (A) Comparison of the overall WT and D17A ^{Nc}NTD structures. Chain B of the WT structure was superimposed with chain B of the D17A structure as these were the subunits that were most similar to each other. **(B)** The subunits of the WT (left) and D17A (right) structures were superimposed to highlight the topology of the helices comprising the five-helix bundles. Note that H2, H3, and H5 are oriented differently to H1 and H4 across the two subunits of the WT dimer, whereas the two subunits of the D17A dimer are much more similar. The helices that comprise the dimer interface are colored, while non-interacting helices are grayed. **(C)** H1, H2, and H3 from each subunit of the WT and D17A ^{Nc}NTD and WT ^{Ea}NTD structures are shown. The D17-D53 handshake interaction (black dashed line) in subunit A of the WT ^{Nc}NTD structure (cyan) alters the angle between helices 2 and 3 in this subunit compared to the other orthologs.

The effect of the D17-D53 handshake interaction on WT ^{Nc}NTD subunit topology was discussed in Chapter 2; briefly, this interaction appeared to stabilize the tertiary structure of subunit A by 'pulling' helix 2 towards helix 1 (Figure 2.3B). The asymmetric nature of this interaction partially accounts for the differing subunit topologies, and this observation is confirmed when the WT ^{Nc}NTD subunit topologies are compared to those of the D17A ^{Nc}NTD and WT ^{Ea}NTD structures. In both of these NTD species, the handshake interaction is absent, either due to mutation (D17A) or presence of a non-acidic residue (Q53 in the ^{Ea}NTD). When comparing the subunits, the angle between helices 2 and 3 is altered by 4.3° in the WT ^{Nc}NTD dimer compared to just 1.6° and 1.7° in the D17A and ^{Ea}NTD structures, respectively (Figure 4.3C). This difference is extremely important, because as described in Chapter 2, the majority of NTD intermolecular contacts involve residues on helices 2 and 3. The effects of the altered dimer interface topology imparted by the D17A mutation on the intermolecular contacts will be discussed below.

D17A mutation influences the arrangement of key intra- and intermolecular interactions

As discussed in Chapter 3, in the WT ^{Nc}NTD, key electrostatic intermolecular interactions are crucial for shaping the dimer interface. The previously described asymmetric D39-K65 and D40-K65 salt bridges are also present in the D17A structure, but they display unique orientations compared to their counterparts in WT structure. Similar to the WT structure, at the front end of the D17A dimer interface, D39 and K65 form an intermolecular salt bridge, but unlike in the WT structure, an intermolecular salt bridge also forms between D40 and K65 (Figure 4.4A). On the back side of the D17A dimer interface, D40 also engages in a salt bridge with K65, while D39 does not participate in intermolecular interactions. Thus, the two ^{Nc}NTD structures display differing sets of short-range salt bridges that utilize the same collection of residues (Figure 4.4B). Additionally, the involvement of K65 in simultaneous salt bridge interactions with both D39 and D40 on one side of the D17A ^{Nc}NTD structure is very similar to the symmetric, long-range electrostatic interactions involving these residues observed in the ^{Ea}NTD (described above, Figure 2.4C). Cumulatively, the differences in the short-range salt bridges between the two ^{Nc}NTD structures and the long-range electrostatic interactions seen in the ^{Ea}NTD underscore the concept of plasticity at the NTD dimer interface. These intermolecular electrostatic interactions are not restricted to specific distances or orientations, and this flexibility allows them to facilitate the alignment of the NTD subunits for dimerization during the rapid silk assembly process.

As described in Chapter 1, the D40-E84 handshake interaction is critical to the pH-relay mechanism that is the basis of pH-dependent NTD dimer formation process (Kronqvist, Otikovs et al. 2014), and mutation of the residues involved in this interaction destabilizes the dimer (Figure 4.4B). The D17A ^{Nc}NTD structure differs from the WT ^{Nc}NTD structure in that it displays symmetric D40-E84 handshake interactions (Figure 5.5B), which mirrors the symmetry of the same interaction in the ^{Ea}NTD (Figure 3.4C). It is tempting to speculate that the increased dimer-stability displayed by the D17A mutant (Figure 5.3) can be partly explained by the presence of the D40-E84 handshake at both ends of the dimer interface, compared to just one instance of this handshake in the WT ^{Nc}NTD structure. Generation of double point mutations, such as D17A/D40N or D17A/E84Q and investigation of their effects on the pH-dependent dimerization process are warranted.

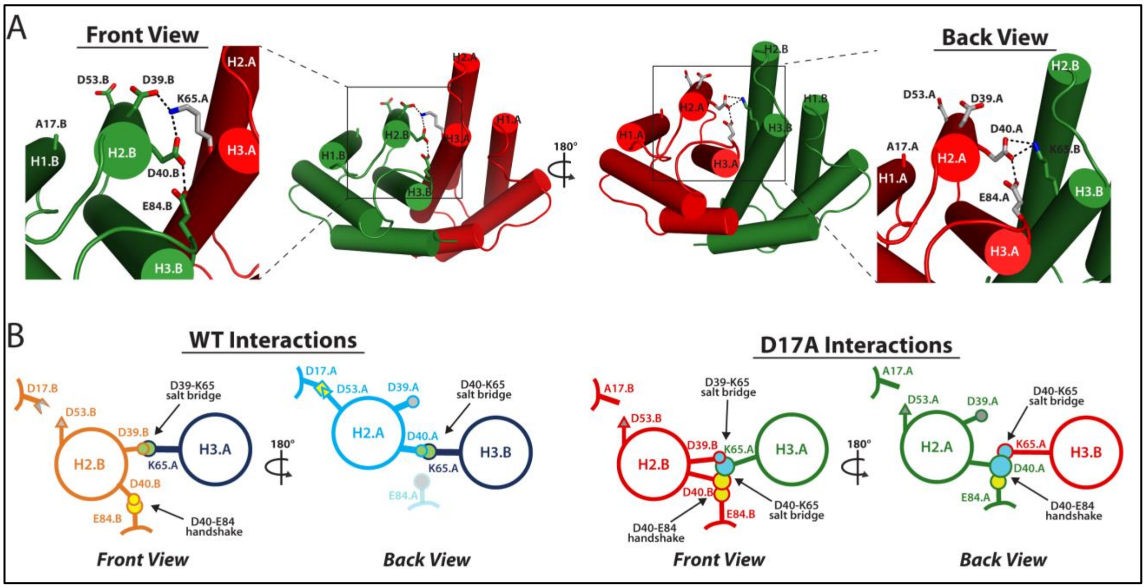

Figure 4.4, Comparison of key intra- and intermolecular interactions in the WT and D17A ^{Nc}NTD structures. **(A)** Front and back views of the D17A dimer reveal differences in the pattern of key salt bridge and handshake interactions taking place between equivalent residues on the two dimer subunits. **(B)** Cartoon schematics for WT and D17A illustrating key intra- and intermolecular interactions at each structure's dimer interface.

D17A mutation results in unique intermolecular contacts

As shown in Figure 4.3C, the D17A mutation alters the tertiary structure of the NTD subunits with respect to WT, which in turn affects the intermolecular contacts observed in this structure. The interfacial helices cross their counterparts at slightly different angles in the WT and D17A structures (Figure 4.5A, middle panels), which results in 9 out of the 41 (22%) of the D17A structure's intermolecular contacts to be unique (Figure 4.5B). Of these unique contacts, in the D17A structure, M71.A on helix 3 makes a unique contact with E79.B (Figure 4.5A, top right panel), which as described in Chapter 1, is a highly conserved residue that becomes protonated during the pH-dependent dimer formation process in the ^{Ea}NTD (Kronqvist, Otikovs et al. 2014). With respect to helix 5, L123.A forms a unique intermolecular contact with M71.B. This pair of contacts is relevant to the altered dimer interface topology imparted by the D17A mutation, because M71 is buried at the center of the dimer interface. Furthermore, the conserved acidic residues E79, E84, and E119 make different sets of contacts in the D17A structure compared to WT (Figure 4.5C). As described above, protonation of these residues is crucial for the transition from weakly to stably associated dimer. Thus, similar to the WT ^{Nc}NTD and ^{Ea}NTD structures, it is possible that the D17A structure could also be a snapshot on the pH-dependent dimer formation pathway.

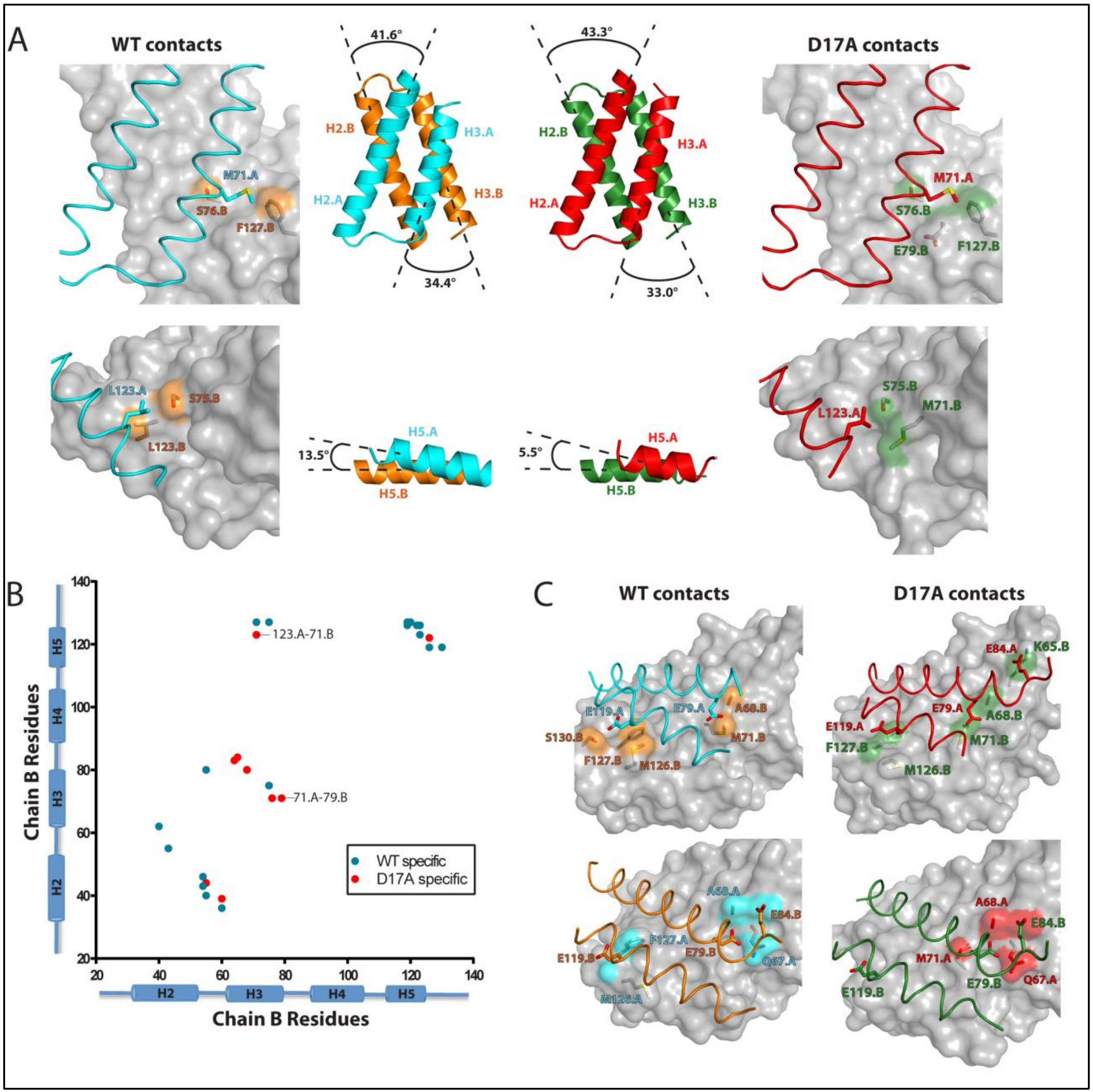

Figure 4.5, The D17A mutation affects the ^{Nc}NTD intermolecular contacts. (A) Differences in the topology of the subunits at the NTD dimer interface results in unique intermolecular contacts. To illustrate the differences in how the interfacial helices are arranged at the dimer interface, I calculated the angles at which H2/H3 (top, middle) and H5 (bottom, middle) cross each other in the WT and D17A ^{Nc}NTD structures, which are shown in the same orientation as ribbons. Angles were calculated using the program Chimera. In the left (WT) and right (D17A) panels, one NTD subunit of each dimer is shown as a transparent gray surface and the other as ribbons. Side chains of residues that engage in novel contacts resulting from the altered interfacial helix topologies are shown as sticks and the surface is colored as in the center panel. Only one side of the dimer interfaces is shown for clarity. **(B)** Similar to Figure 2.5B, a protein contact map shows where the unique intermolecular contacts are clustered on the secondary structure elements of the WT (cyan) and D17A (red) ^{Nc}NTD structures. The protein contact maps are restricted to show only unique intermolecular contacts. Residue numbers are indicated on the x and y axes. The secondary structure of the subunits is also shown on the axes to facilitate identification of where the unique contacts are occurring in the context of the structure. Unique contacts that were discussed in the text are indicated with lines and the residue numbers shown. **(C)** Intermolecular contacts for conserved acidic residues E79, E84, and E119 in both protomers of WT and D17A. One NTD subunit of each dimer is shown as a semitransparent gray surface and the other as ribbons. Side chains of conserved acidic residues and the residues to which they make intermolecular contacts are shown as sticks and the surface is colored as in panel (A).

Conclusions

In this chapter I have presented the high resolution crystal structures for the ^{Nc}NTD R57A and D17A mutants. The R57A structure is almost identical to that of WT, suggesting that the D17-D53 handshake observed in the WT structure is physiologically relevant and not the result of a crystal packing interaction with R57. Conversely, the D17A structure displays distinct differences to the WT structure in both its subunit topologies and sets of intra- and intermolecular contacts. These differences appear to have direct effects on the pH-dependent dimer formation of the D17A mutant compared to WT, mostly likely due to alterations of the dimer interface and intermolecular contacts involving key residues that are protonated during the pH decrease that facilitates spidroin NTD dimerization.

The asymmetry of the D17-D53 handshake observed in the WT ^{Nc}NTD could contribute to the conformational selectivity model proposed in Chapter 2, in which the NTD monomer subunits exist in an ensemble of conformers in the high pH and salt concentration conditions of the ampullate gland (Ries, Schwarze et al. 2014). Dimerization is initiated when a subunit selects a binding partner with a complementary binding interface from this group. The presence or absence of the D17-D53 handshake alters the subunit topology, and the subunits within the D17A structure represent specific NTD conformers within the ensemble in which the D17-D53 handshake is absent in both conformers. This specific pair of conformers appears to facilitate dimer formation at a higher pH compared to the pair of subunit topologies observed in the WT ^{Nc}NTD. The unique arrangement of the intermolecular salt bridges in the D17A structure further supports the concept of NTD dimer interface plasticity, which also contributes to the conformational selectivity model by providing a means for properly aligning subunits of differing topologies to form the weakly associated dimer. The different pairs of subunit topologies affect the burial or exposure of residues at the center of the dimer interface, such as M71, which in turn affects the intermolecular proximity of the conserved acidic residues E79, E84, and E119. The subsequent pH-dependent protonation of these residues relieves the electrostatic stress brought about by this proximity. Thus, I propose that the D17-D53 handshake interaction contributes to the MaSp dimerization process by providing a mechanism for imparting increased conformational heterogeneity to the ensemble of the NTD subunits. This increase in variability would theoretically decrease the NTD dimerization rate and thereby prevent premature aggregation of the spidroins during the tightly regulated salt- and pH-dependent NTD dimer formation process.

Table 4.1, Crystallographic Data and Refinement Statistics for R57A and D17A

	^{Nc}NTD R57A	^{Nc}NTD D17A
PDB ID	N/A	N/A
Source	APS 22 ID	APS 22 ID
Wavelength (Å)	1.00	1.00
Resolution Limits (Å)	29.92-2.22 (2.30-2.22)	50.00-1.70 (1.76-1.70)
Space Group	$P3_121$	P1
Unit Cell (Å) *a, b, c*	67.2, 67.2, 89.8	35.9, 41.0, 46.4
Unit Cell (°) α, β, γ	90, 90, 120	70, 84.7, 67.4
Number of observations	114845	96998
Number of reflections	11945 (610)	24544 (2328)
Completeness (%)	99.6 (94.4)	96.7 (92.4)
Mean I/σI	0.14 (0.048)	0.12 (0.10)
R-merge on I [a]	8.6 (32.0)	4.1 (12.0)
Cut-off criteria I/σI	-3	-3
Refinement Statistics		
Resolution Limits (Å)	29.9-2.22 (2.30-2.22)	33.7-1.70 (1.76-1.70)
# of reflections (work/free)	11924/1178	24538/2000
Completeness (%)	99.7 (98.0)	96.7 (91.0)
Cutoff Criteria I/σI	0	0
Protein/water atoms	1829/87	2098/299
R_{cryst} [b]	0.1910 (0.2859)	0.1361 (0.1536)
R_{free} (10% of data)	0.2492 (0.3673)	0.1637 (0.1799)
Bonds (Å)/ Angles (°)	0.007/0.8	0.005/0.77
B-factors: protein/water ($Å^2$)	27.8/28.2	21.9/33.0
Ramachandran statistics (%)		
Preferred regions	100	100
Outlier regions	0.0	0.0
MolProbity score	1.02- 100th percentile (N=454, 2.224 Å ± 0.25Å)	0.98- 100th percentile (N=1784, all resolutions)

Parentheses indicate statistics for the high-resolution data bin for x-ray data.
a. $Rmerge = \sum hkl \sum i|I(hkl)i - <I(hkl)>|/\sum hkl \sum i <I(hkl)i>$.
b. $Rcryst = \sum hkl\ |Fo(hkl)-Fc(hkl)|/\sum hkl\ |Fo(hkl)|$, where *Fo* and *Fc* are observed and calculated structure factors, respectively.

Chapter 5: NMR-Mediated Investigation of the ^{Nc}NTD

Introduction

In the preceding chapters, I have presented high resolution crystal structures of the WT and D17A ^{Nc}NTD. These structures have provided valuable insight on the specific residues that appear to facilitate ^{Nc}NTD dimerization, and biochemical assays probing these residues have illuminated some of their mechanistic roles. The D17-D53 handshake interaction was identified in the WT ^{Nc}NTD crystal structure, and its importance to pH-dependent NTD dimerization has been explored using tryptophan fluorescence. However, the crystal structures are only a snapshot of the protein in a specific condition; in an effort to study the previously identified key intra- and intermolecular interactions in a more dynamic way, I conducted a variety of NMR-based experiments on the WT and D17A ^{Nc}NTD. These experiments stemmed from assignment of the backbone residues of the wild type WT ^{Nc}NTD (Parnham, Gaines et al. 2011), which were used for secondary structure prediction, relaxation, and titration experiments. Also, I have begun to collect a series of NMR titration experiments that could give even more detailed insight into the mechanisms of ^{Nc}NTD pH-dependent dimer formation. The preliminary data presented in this chapter give insight into the effects of specific salt and pH conditions on the dynamic nature of certain residues within the structure and provided an excellent starting point for more refined NMR-based experiments that probe the dynamic nature of the protein's key structural elements.

Experimental Procedures

NMR backbone assignments—To obtain isotope-labeled ^{Nc}NTD, the protein was expressed and purified in M9 minimal media, which was prepared using [^{15}N] ammonia as the primary nitrogen source and either unlabeled or [^{13}C] glucose as the primary carbon source for protein synthesis.

Standard triple-resonance experiments for the [^{13}C]- and [^{15}N]-labeled WT ^{Nc}NTD at pH 7.0, 500 mM NaCl were collected. All NMR experiments were carried out at 298 K, using approximately 500 µM of protein per sample. The NMR data were processed using nmrPipe (Delaglio 1995), and analyzed with Sparky NMR Assignment and Integration software (Goddard 2015). Sequential backbone assignments were achieved using 2D HNHSQC and through-bond 3D HNCACB, CBCA(CO)NH, HNCA, HN(CO)CA, and HNCO experiments.

NMR Relaxation—^{15}N-labeled WT protein was buffer-exchanged to the desired condition and concentrated to 500 µM. The NMR sample was prepared by mixing 450 µl of protein with 50 µl of 100% D_2O. The protein was excited with a series of magnetization pulses and then allowed to relax to its native state. The longitudinal (T_1) and transverse (T_2) relaxation times were varied, and an HNHSQC spectrum was recorded for each. The T_1 or T_2 times used are listed in Table 5.1. Exponential decay curves (plotted as $h = Ae^{(-Rt)}$ where 'h' is data height and 't' is the spectrum time parameter) of the data height for each peak were fitted using UCSF Sparky's Relaxation Fitting command (Goddard 2015), and T_1 or T_2 times for each residue where calculated from these curves as the time constant $T= 1/R$ and plotted by residue. In this way, the individual contribution of each residue to the protein's overall dynamic nature could be observed.

NMR titrations—A series of NaCl and pH titrations were collected for the WT and D17A ^{Nc}NTD. Each sample was expressed as ^{15}N-labeled protein, buffer-exchanged to pH 7.0, 50 mM NaCl, and concentrated to 500 µM. The samples were titrated to pH 5.4, 50 mM NaCl in 0.2 pH unit steps, and an HNHSQC spectrum was collected at each step.

Results and Discussion

Assignment of WT ^{Nc}NTD HNHSQC

Identification of the backbone residues in the HNHSQC is the crucial starting point for all of the NMR-based experiments. Thus, ^{13}C- and ^{15}N- labelled WT protein was expressed in order to collect standard 2D and 3D assignment spectra (see Experimental Methods section). As shown in Figure 5.1, 97% of the backbone residues were assigned for the WT protein in a buffer at pH 7.0 with 500 mM NaCl. Residue P114 could not be assigned as prolines do not have an amide proton, and peaks for residues T13 and N64 could not be verified using the correlated 3D spectra. The buffer conditions of pH 7.0 and 500 mM NaCl were considered the most monomer-favoring conditions based on previous studies of the ^{Nc}NTD (Gaines, Sehorn et al. 2010), and they were chosen to prevent ambiguity of peaks that could occur if the population of protein was a mixture of monomers and dimers. The backbone assignments were unambiguously assigned using coordinated CBCA(CO)NH and HNCACB spectra (Figure 5.2), and peak assignment was assisted using the Sparky PINE server (Lee, Westler et al. 2009) and verified against deposited assignments previously collected for the WT ^{Nc}NTD (Parnham, Gaines et al. 2011).

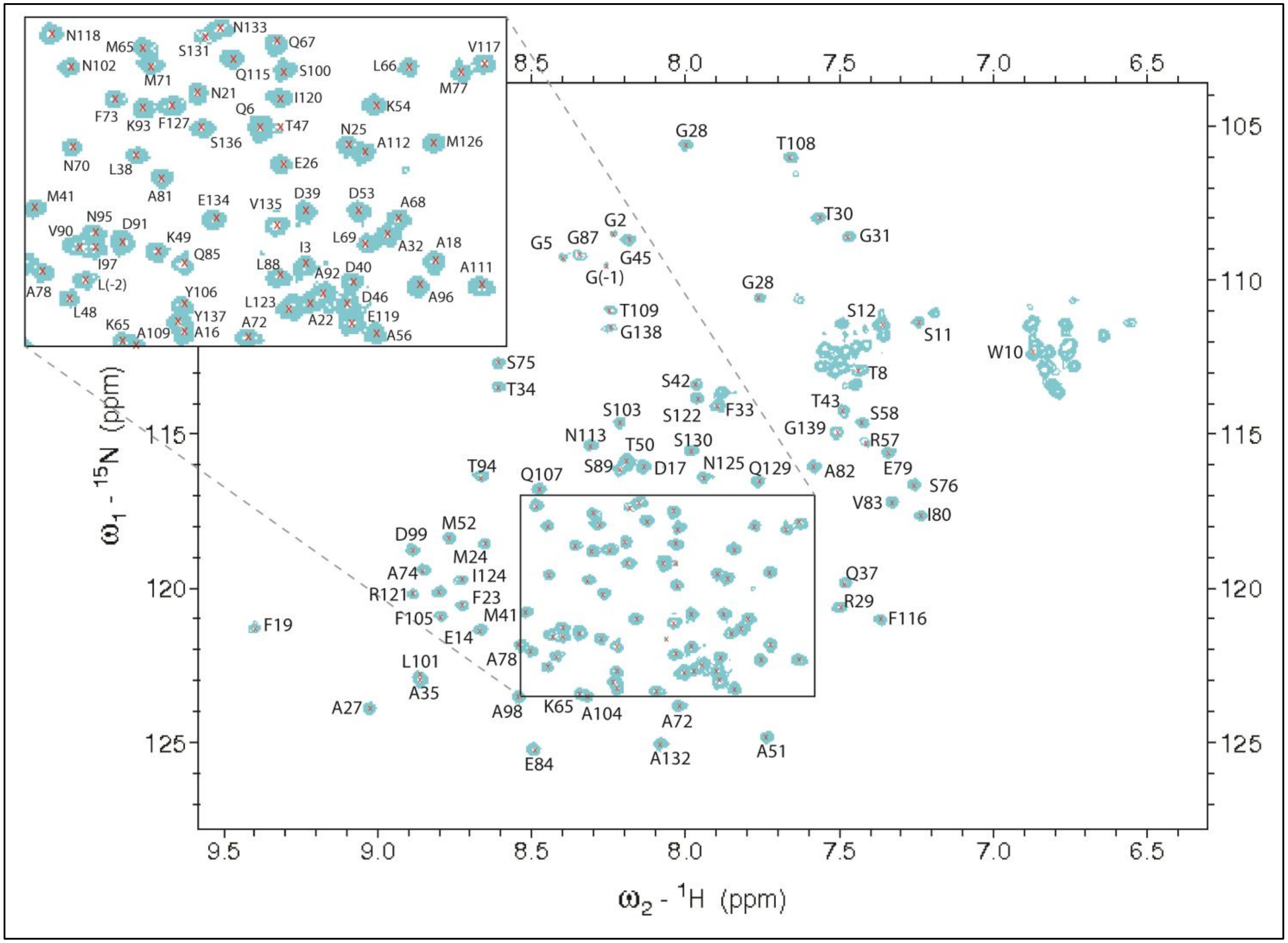

Figure 5.1, HNHSQC spectrum for WT at pH 7.0, 500 mM NaCl. Backbone assignments for the WT protein were generated by collecting a set of 2D and 3D NMR experiments at monomer-favoring conditions (pH 7.0, 500 mM) in an effort to prevent any signal distortion caused by NTD dimerization. For clarity, the assignments for the cluster of peaks at the middle of the spectrum are shown in the insert.

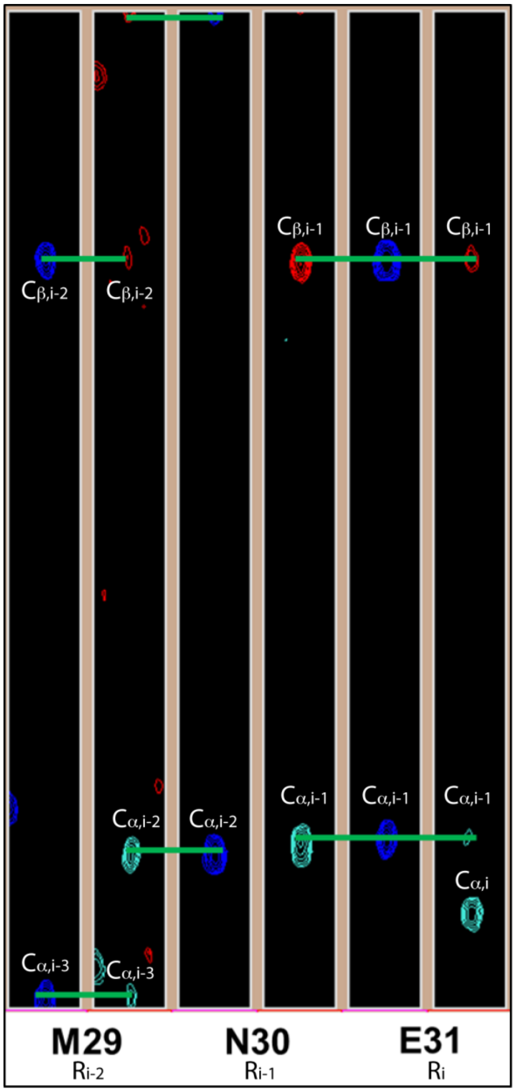

Figure 5.2, Example of 'backbone walk' used for HNHSQC assignments. For a given residue R_i, where i represents the residue's number in the primary sequence of the protein, the peak on the HNHSQC (Figure 5.1) corresponds to its amide (N) and amide proton (HN) chemical shift. Generally, each peak in the HNHSQC spectra is correlated to peaks in the CBCA(CO)NH and HNCACB spectra. The peaks in CBCA(CO)NH identify the $C_{\alpha,i-1}$ and $C_{\beta,i-1}$ of R_i in the CBCACONH and the peaks in the HNCACB spectra identify $C_{\alpha,i}$, $C_{\alpha,i-1}$, $C_{\beta,i}$, and $C_{\beta,i-1}$. Thus, by generating the strip plots as seen in this figure, the peaks of consecutive residues can be aligned. The three residues in this figure serve as an example for these assignments, with E31 designated as R_i. The blue peaks of E31's CBCA(CO)NH would correspond to its $C_{a,i-1}$ and $C_{\beta,i-1}$, which in this case are the C_α (cyan peak) and C_β (red peak) in N30's HNCACB, since N30 is R_{i-1}. In turn, N30's CBCA(CO)NH peaks would correspond to $C_{\alpha,i-2}$ and $C_{\beta,i-2}$, which in this case are the C_α and C_β of M29. Each residue has unique shifts for its C_α and C_β, which facilitates assignments.

NMR Relaxation Experiments

NMR relaxation experiments permitted observation of the dynamics of the individual residues in the various monomer- or dimer-favoring conditions. For each protein sample at the monomer- or dimer-favoring conditions, a series of T_1 (longitudinal) and T_2 (transverse) relaxation experiments were collected and recorded as 2D HNHSQC spectra. For the high pH conditions (pH 7.0, 500 and 50 mM NaCl), the backbone residues were assigned using the same assignments shown in Figure 2.1. However, I was unable to verify the assignments for the data collected at the pH 5.5, 50 mM NaCl condition, because the chemical shifts were significantly different for many of the peaks, which prevented transfer of the assignments from those of the monomer-favoring conditions. Thus, these peaks were arbitrarily numbered and the data from this condition was not used in the same analysis as that of the high pH conditions. The T_1 and T_2 values are shown for assigned residues of the ^{Nc}NTD collected at pH 7.0, 500 or 50 mM NaCl in Figure 5.3.

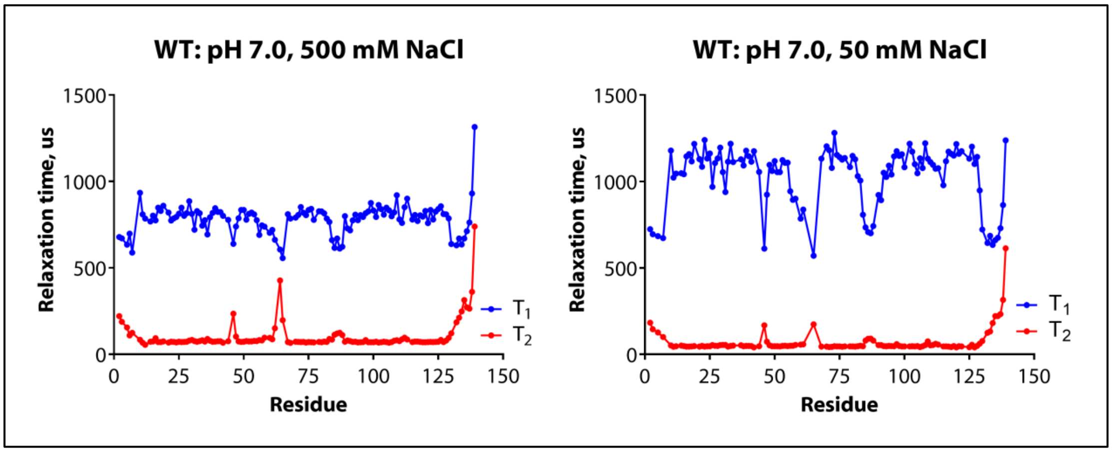

Figure 5.3, T_1 and T_2 relaxation times for WT ^{Nc}NTD. The T_1 and T_2 relaxation times are plotted for each residue at the pH 7.0, 500 mM NaCl (left) and pH 7.0, 50 mM NaCl (right) conditions. The relaxation times were calculated as described in the Experimental Procedures section.

NMR-Mediated Titration Experiments

HNHSQC spectra were collected for both the WT and D17A mutant at the monomer-favoring (pH 7.0) and dimer-favoring (pH 5.4) conditions. For both pH conditions, the WT and D17A spectra overlay well (Figure 5.4, A and B), which indicates that the general structures of the two proteins are mostly identical. Additionally, the sets of peaks at each condition are very distinct, indicating a clear structural shift in response to the decreased pH. This observation is in agreement with the tryptophan fluorescence data presented above, in which both proteins are monomeric at high pH and dimeric at low pH. As seen in the tryptophan fluorescence data, the monomer-to-dimer transition points for WT and D17A are significantly different (Figure 5.4), and thus, NMR-mediated observation of the proteins at steps along the physiologic pH range is warranted.

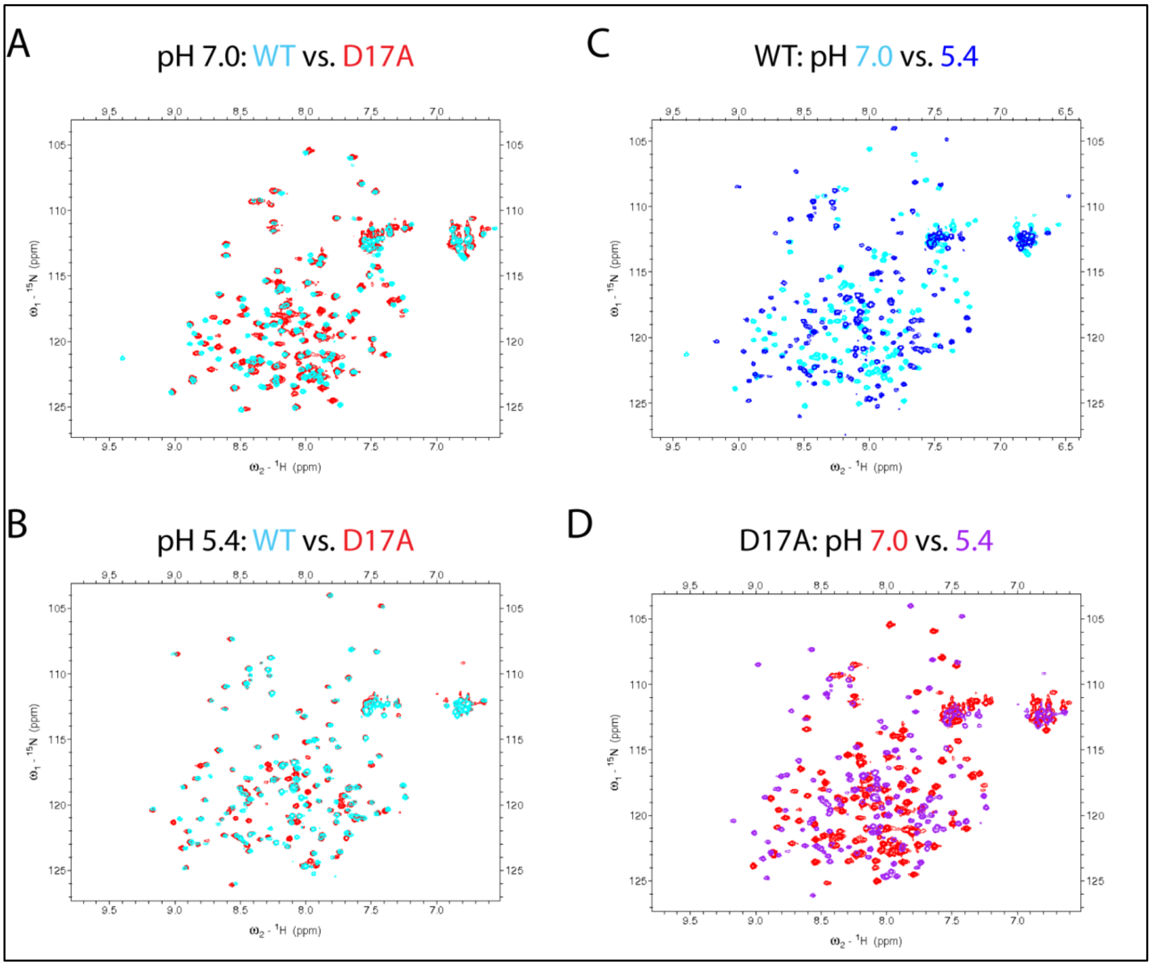

Figure 5.4, HNHSQC spectra for WT and D17A at high and low pH. HNHSQC spectra were collected as described in the Experimental Procedures section for WT and D17A at pH 7.0 and 5.4, both with 50 mM NaCl. The spectra are overlaid to compare **(A)** WT vs. D17A at pH 7.0, **(B)** WT vs. D17A at pH 5.4, **(C)** WT at pH 7.0 vs. 5.4, and **(D)** D17A and pH 7.0 vs. 5.4.

For ideal comparison to the tryptophan fluorescence data, the WT and D17A proteins were titrated from 7.0 to 5.5 in 0.2 pH unit increments, and an HNHSQC spectrum was collected at each step (Figure 5.5 for WT and Figure 5.6 for D17A). For a more reliable quantitative analysis of this data, the assignments for both proteins at each pH step will need to be generated and verified. With these in hand, the difference in chemical shift for each residue will be calculated and plotted against the change in pH. Qualitatively, the raw data appears to confirm the tryptophan fluorescence data. For the WT titration, the peak intensities begin to waver around pH 6.4-6.2, while for the D17A titration, they begin to waver around pH 6.8-6.6. Once all of the peak assignments have been made, I will be able to track the loss of intensity and/or movement of specific residues, which will indicate in what order key regions of the protein rearrange during the pH decrease.

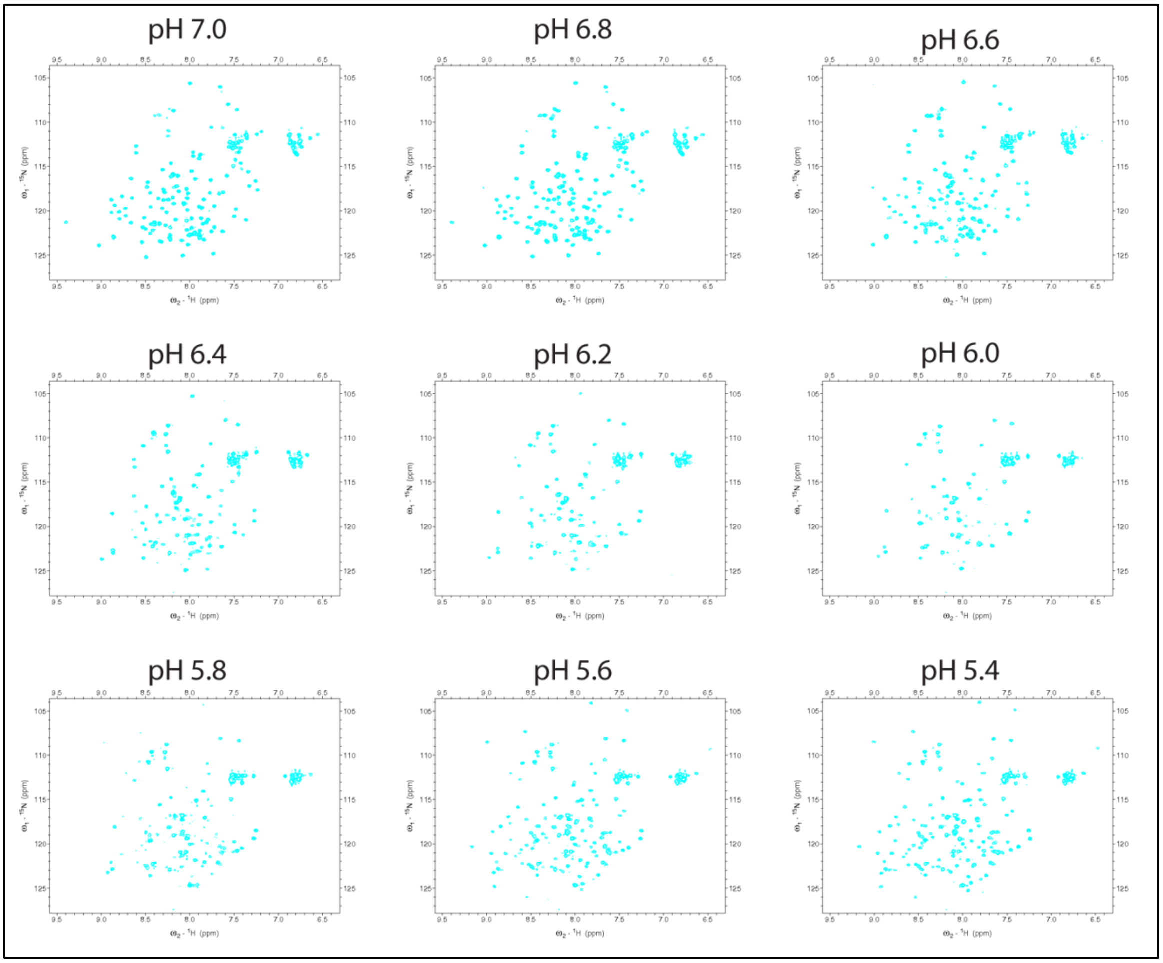

Figure 5.5, HNHSQC spectra for WT titration points. As described in the Experimental Procedures section, an HNHSQC spectrum for the WT protein was recorded for each pH titration point. The unassigned spectra are shown here.

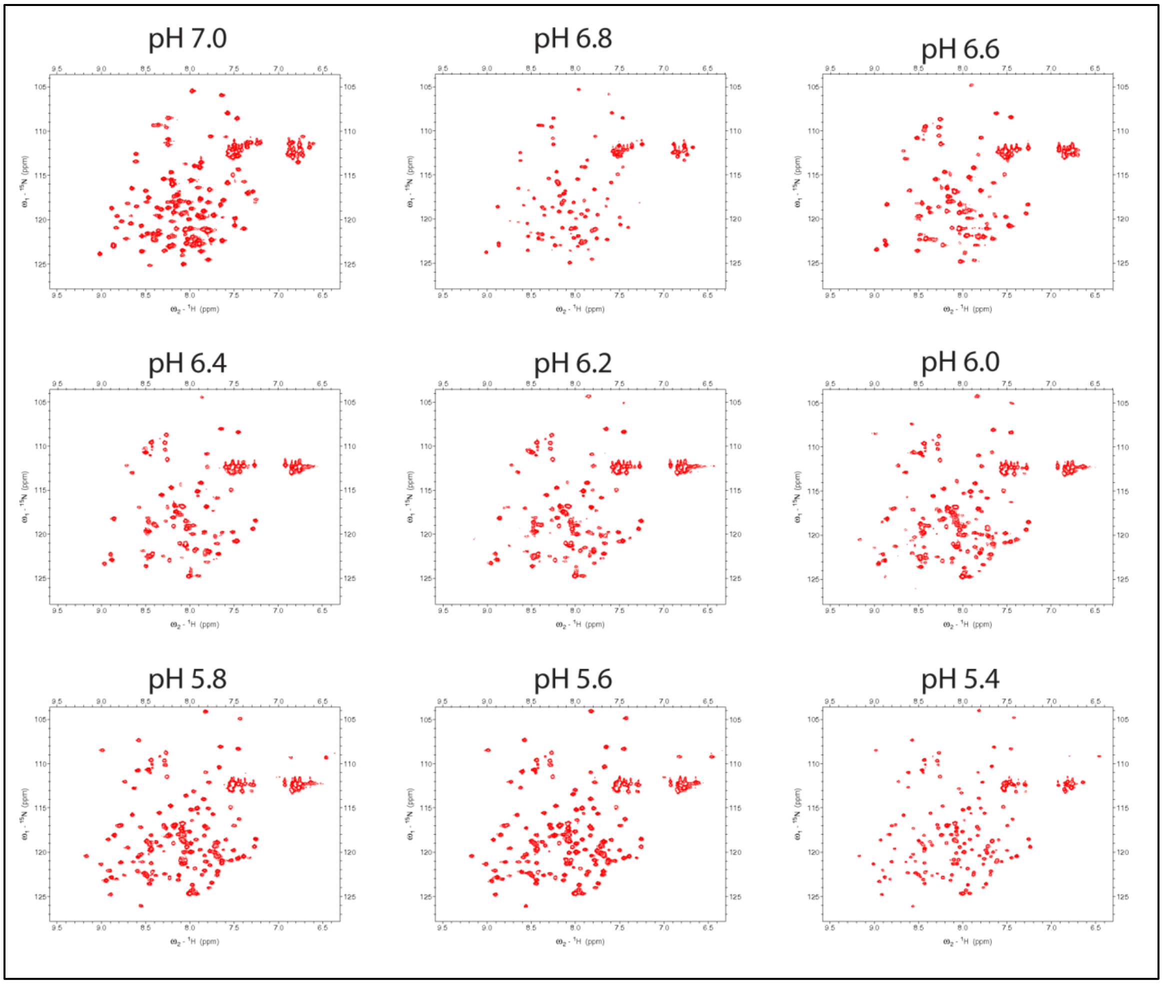

Figure 5.6, HNHSQC spectra for D17A titration points. As described in the Experimental Procedures section, an HNHSQC spectrum for the D17A protein was recorded for each pH titration point. The unassigned spectra are shown here.

Conclusions

In this chapter, I have presented preliminary NMR-mediated experiments on the ^{Nc}NTD. Although assignment of the backbone residues was achieved for the monomer-favoring condition, the large degree of chemical shifts of the peaks in the low pH dimer-favoring condition did not permit a transfer of these assignments. However, the relaxation data at pH 7.0 for both salt concentrations compares favorably with previously collected chemical shifts of the ^{Nc}NTD (Parnham, Gaines et al. 2011), and the rotational correlation time-derived molecular weights align with theoretical molecular weights of the ^{Nc}NTD at the monomer and dimer favoring conditions and confirm the results from the size-exclusion chromatography experiments (Figure 3.2). As a future direction, the relaxation experiments can be performed at two different magnetic field strengths, which will allow observation small amplitude bond fluctuations that reflect on the local environment around each residue and provide further structural information.

The data presented in this chapter lay the groundwork for residue-specific monitoring of the pH-dependent NTD dimerization. I hope that once backbone assignments have been collected, I will be able to make more detailed conclusions about the roles of specific residues and regions of the protein with respect to the change in pH. These data could also be used to determine the pKa's of specific side chains (Everill, Sudmeier et al. 2012), such as for the conserved acidic residues (E79, E84, and E119) thought to be protonated during the pH-mediated dimerization (Kronqvist, Otikovs et al. 2014) or similarly, to investigate possible protonation of the D17 or D53 side chains. Further characterization of the ^{Nc}NTD utilizing NMR will provide valuable information pertaining to the dynamics of the key residues thought to be involved in the intricate salt- and pH-dependent dimer formation process.

Chapter 6: Overall Conclusions and Future Directions

Overall Conclusions

In this dissertation, I have investigated the mechanisms that govern ^{Nc}NTD dimer formation using a combination of structural analysis and various biochemical assays.

To gain a better understanding of the ^{Nc}NTD structure, I solved the first high resolution crystal structure of the wild type ^{Nc}NTD (Chapter 3), and comparison of it to the structures of spidroin NTDs from other spider species has revealed key structural features thought to be important to the NTD dimerization process. The WT ^{Nc}NTD structure is the first to show two subunits displaying significantly different topologies in the same dimer, which is in stark contrast to the almost identical subunits seen in the well-characterized ^{Ea}NTD (Askarieh, Hedhammar et al. 2010). The ^{Nc}NTD structure contains two intermolecular salt bridges between D39 and K65 on one side of the dimer interface and D40 and K65 on the other. These interactions provide a molecular basis to explain the dimer destabilizing effects that result from mutation of these residues in other NTD species (Schwarze, Zwettler et al. 2013, Kronqvist, Otikovs et al. 2014), and the asymmetry of these salt bridges contributes to the plasticity of the ^{Nc}NTD dimer interface. The ^{Nc}NTD structure also contains a novel handshake interaction between highly conserved acidic residues D17 and D53 that appears to affect the topology of the NTD subunits. The ^{Nc}NTD and previously published spidroin NTD structures (Askarieh, Hedhammar et al. 2010, Jaudzems, Askarieh et al. 2012, Kronqvist, Otikovs et al. 2014) could all be on pathway snapshots of the NTD during the pH-dependent dimerization process.

I investigated the effects on dimerization of mutation of the key residues identified in the wild type ^{Nc}NTD structure using a series of biochemical assays (Chapter 4). The crosslinking and size exclusion experiments confirm the importance of the D40-K65 salt bridge for salt-dependent NTD dimerization. The tryptophan fluorescence assay showed that mutations that perturb the D39-K65 and D40-K65 salt bridges and the canonical D40-E84 handshake all decrease the NTD's ability to form dimers compared to WT. Conversely, disruption of the D17-D53 handshake interaction via the D17A mutation stabilized the dimer at a higher pH compared to WT. These data prompted me to investigate the residues involved in this interaction further.

The R57A mutant was generated to ensure that the D17-D53 handshake interaction was not an artifact of crystal packing (Chapter 5). This mutant is essentially identical to the WT protein in both structure and pH-dependent dimerization behavior, which confirmed the structural relevance of the D17-D53 handshake. Conversely, the D17A mutant was structurally distinct from the WT in both its subunit topologies and intermolecular interactions, which further supports the concept of dimer interface plasticity.

I have also begun using several NMR-based approaches to study the ^{Nc}NTD in monomer- and dimer-favoring conditions (Chapter 5). Almost complete assignment of the backbone residues at monomer-favoring conditions allowed residue-specific relaxation analysis, which in turn yielded interesting information regarding the dynamics of various regions of the protein. NMR titration data, which needs further analysis including complimentary NOESY experiments, reveal differences in the monomer-dimer transition for the WT and D17A in terms of chemical shift differences at each pH step. Further studies will be needed to track the structural effects of specific residues during pH-dependent dimerization.

In conclusion, I propose that the D17-D53 handshake present in one subunit of the WT ^{Nc}NTD crystal structure acts as a mechanism to increase the heterogeneity of the possible conformers the NTD subunits can adopt. Based on the proposed model of NTD conformational selectivity (Schwarze, Zwettler et al. 2013), an increased variability of conformers would result in a wider range of possible subunit pairings. The subunits in the D17A structure, neither of which contains the D17-D53 handshake interaction, dimerize at a higher pH than those of the WT structure, in which this handshake interaction is asymmetric. Thus, it is possible that increased conformer diversity broadens the range of pH-dependent ^{Nc}NTD dimerization, which could be important for preventing premature spidroin aggregation during the silk spinning process.

Future Directions

The D17-D53 handshake has been shown to be crucial to regulating ^{Nc}NTD dimer formation. Therefore, a variety of experiments could be pursued to further examine its importance. As mentioned above, acidic residues at positions 17 and 53 are highly conserved among MaSp NTDs; however, the only published structures (besides that of the ^{Nc}NTD) are of the *E. australis* MaSp NTD, in which residue 53 is a glutamine and this handshake interaction is absent. Structures for other MaSp NTDs that harbor acidic residues at both position 17 and 53, such as those of the *L. hesperus* or *N. inaurata* species, would confirm if this interaction is truly conserved. Additionally, to further probe if the D17-D53 handshake interaction is part of the pH-relay mechanism, generation of double- and triple-point mutants that mimic protonation of other conserved acidic residues in the ^{Nc}NTD could be generated. In this way, one could investigate if the D17-D53 handshake plays a similar role in the pH-dependent dimerization as the D40-E84 handshake in the ^{Ea}NTD (Kronqvist, Otikovs et al. 2014). The effects of these mutants on dimer formation could be investigated using tryptophan fluorescence, urea denaturation, and NMR experiments, and theoretically, it can be determined if protonation of either D17 or D53 is also necessary for NTD dimerization.

Interestingly, even though they serve the same biological purposes, dragline silks from different spider species display a wide range of mechanical properties, which are likely due to differences in biochemical composition (Vollrath and Knight 2001). As shown, substitutions of single residues can have a significant impact on the tertiary and quaternary structures of the spidroin NTD, which in turn can affect the structure of the entire spidroin. Thus, the previously described ‘mini-spidroins’ could be generated to contain key mutations such as D17A in the NTD, and their strength and elasticity could be compared to see if NTD structural alterations affect the mechanical properties of the silks. These analyses could be enhanced by crystal or cryo-electron microscopy structures of these mini-spidroins, which could lend insight into the relationship between differing NTD subunit topologies and the other spidroin domains.

Impact on the Field

The results of this work contribute to the general understanding of how spiders spin silk and could impact how silks are incorporated into biomaterials. The crystal structure of the WT ^{Nc}NTD is the first to show two distinctly different subunit topologies within the same dimer due to the asymmetry of the novel D17-D53 handshake interaction, which in turn affects the pH-dependent dimerization of the ^{Nc}NTD. The acidic residues at positions 17 and 53 are highly conserved among MaSp NTDs, which implies that the structural features imparted by the handshake interaction between these residues observed in the ^{Nc}NTD are likely also present in other spidroin NTDs. Thus, it is possible that the WT ^{Nc}NTD structure displays the more representative dimer topology for MaSp NTD structures compared to the published ^{Ea}NTD structures. The WT and D17A ^{Nc}NTD structures also demonstrate how the infidelity of the D39-K65 and D40-K65 salt bridges promotes dimer interface plasticity. This mechanism could contribute to the conformational selectivity model thought be involved in regulating the pH-dependent NTD dimer formation.

The production of artificial silks for biomaterial applications can also be enhanced by the findings of this work. The concept of dimer interface plasticity conferred by the D39-K65 and D40-K65 salt bridges could be expanded by adding more oppositely charged residues to the ends of the dimer interface, thereby strengthening the initial dimerization action. The presence or absence of the D17-D53 handshake has a clear effect on the pH-dependent dimerization of the ^{Nc}NTD; perhaps this can be incorporated in the production process to regulate the speed of silk production. Overall, this work contributes to the ever-improving production of spider silk-based biomaterials that will hopefully continue to yield innovative devices and products in the healthcare field.

REFERENCES

Adams, P. D., P. V. Afonine, G. Bunkóczi, V. B. Chen, I. W. Davis, N. Echols, J. J. Headd, L.-W. W. Hung, G. J. Kapral, R. W. Grosse-Kunstleve, A. J. McCoy, N. W. Moriarty, R. Oeffner, R. J. Read, D. C. Richardson, J. S. Richardson, T. C. Terwilliger and P. H. Zwart (2010). "PHENIX: a comprehensive Python-based system for macromolecular structure solution." Acta crystallographica. Section D, Biological Crystallography **66**(Pt 2): 213-221.

Adrianos, S. L., F. Teulé, M. B. Hinman, J. A. Jones, W. S. Weber, J. L. Yarger and R. V. Lewis (2013). "*Nephila clavipes* Flagelliform silk-like GGX motifs contribute to extensibility and spacer motifs contribute to strength in synthetic spider silk fibers." Biomacromolecules **14**(6): 1751-1760.

Allmeling, C., A. Jokuszies, K. Reimers, S. Kall, C. Y. Choi, G. Brandes, C. Kasper, T. Scheper, M. Guggenheim and P. M. Vogt (2008). "Spider silk fibres in artificial nerve constructs promote peripheral nerve regeneration." Cell Proliferation.

Altman, G. H., F. Diaz, C. Jakuba, T. Calabro, R. L. Horan, J. Chen, H. Lu, J. Richmond and D. L. Kaplan (2003). "Silk-based biomaterials." Biomaterials **24**(3): 401-416.

Andersson, M., G. Chen, M. Otikovs, M. Landreh, K. Nordling, N. Kronqvist, P. Westermark, H. Jörnvall, S. Knight, Y. Ridderstråle, L. Holm, Q. Meng, K. Jaudzems, M. Chesler, J. Johansson and A. Rising (2014). "Carbonic Anhydrase Generates CO_2 and H^+ That Drive Spider Silk Formation Via Opposite Effects on the Terminal Domains." PLoS Biology **12**(8).

Andersson, M., L. Holm, Y. Ridderstråle, J. Johansson and A. Rising (2013). "Morphology and composition of the spider major ampullate gland and dragline silk." Biomacromolecules **14**(8): 2945-2952.

Arøen, A., S. Løken, S. Heir, E. Alvik, A. Ekeland, O. G. Granlund and L. Engebretsen (2004). "Articular cartilage lesions in 993 consecutive knee arthroscopies." The American Journal of Sports Medicine **32**(1): 211-215.

Askarieh, G., M. Hedhammar, K. Nordling, A. Saenz, C. Casals, A. Rising, J. Johansson and S. D. Knight (2010). "Self-assembly of spider silk proteins is controlled by a pH-sensitive relay." Nature **465**(7295): 236-238.

Augsten, K., P. Mühlig and C. Herrmann (2000). "Glycoproteins and skin-core structure in *Nephila clavipes* spider silk observed by light and electron microscopy." Scanning **22**(1): 12-15.

Ayoub, N. A. and C. Y. Hayashi (2008). "Multiple Recombining Loci Encode MaSp1, the Primary Constituent of Dragline Silk, in Widow Spiders (*Latrodectus: Theridiidae*)." Molecular Biology and Evolution **25**(2): 277-286.

Baneyx, F. and M. Mujacic (2004). "Recombinant protein folding and misfolding in *Escherichia coli.*" Nature Biotechnology **22**(11): 1399-1408.

Bell, A. L. and D. B. Peakall (1969). "Changes in fine structure during silk protein production in the ampullate gland of the spider *Araneus sericatus*." The Journal of Cell Biology **42**(1): 284-295.

Berg J, T. J., Stryer L. (2002). " Biochemistry.".

Breslauer, D. N., L. P. Lee and S. J. Muller (2009). "Simulation of flow in the silk gland." Biomacromolecules **10**(1): 49-57.

Brooks, A. E., H. B. Steinkraus, S. R. Nelson and R. V. Lewis (2005). "An investigation of the divergence of major ampullate silk fibers from Nephila clavipes and Argiope aurantia." Biomacromolecules **6**(6): 3095-3099.

Buckwalter, J. A. and H. J. Mankin (1998). "Articular cartilage: degeneration and osteoarthritis, repair, regeneration, and transplantation." Instr. Course Lect. **47**.

Casem, M. L., L. P. P. Tran and A. M. Moore (2002). "Ultrastructure of the major ampullate gland of the black widow spider, *Latrodectus hesperus*." Tissue & Cell **34**(6): 427-436.

Chen, M. B., F. Zhang and W. C. Lineaweaver (2006). "Luminal fillers in nerve conduits for peripheral nerve repair." Ann. Plast. Surg **57**.

Chen, X., D. P. Knight and F. Vollrath (2002). "Rheological characterization of *Nephila* spidroin solution." Biomacromolecules **3**(4): 644-648.

Delaglio, F. G., Stephan; Vuister, Geerten W.; Zhu, Guang; Pfeifer, John; Bax, Ad (1995). "NMRPipe: A multidimensional spectral processing system based on UNIX pipes." Journal of Biomolecular NMR **6**(305): 17.

Dicko, C., D. Knight, J. M. Kenney and F. Vollrath (2004). "Secondary structures and conformational changes in flagelliform, cylindrical, major, and minor ampullate silk proteins. Temperature and concentration effects." Biomacromolecules **5**(6): 2105-2115.

Dicko, C., F. Vollrath and J. M. Kenney (2004). "Spider silk protein refolding is controlled by changing pH." Biomacromolecules **5**(3): 704-710.

Eisoldt, L., J. G. Hardy, M. Heim and T. R. Scheibel (2010). "The role of salt and shear on the storage and assembly of spider silk proteins." Journal of Structural Biology **170**(2): 413-419.

Eles, P. T. and C. A. Michal (2004). "A DECODER NMR study of backbone orientation in *Nephila clavipes* dragline silk under varying strain and draw rate." Biomacromolecules **5**(3): 661-665.

Emsley, P. (2013). "COOT." COOT.

Everill, P., J. L. Sudmeier and W. W. Bachovchin (2012). "Direct NMR Observation and pKaDetermination of the Asp102 Side Chain in a Serine Protease." Journal of the American Chemical Society **134**(4): 23482354.

Exler, J. H., D. Hümmerich and T. Scheibel (2007). "The amphiphilic properties of spider silks are important for spinning." Angewandte Chemie (International ed. in English) **46**(19): 3559-3562.

Fahnestock SR, I. S. (1997). "Synthetic spider dragline silk proteins and their production in *Escherichia coli*." Applied Microbiology and Biotechnology **47**(1): 23-32.

Ferruzzi, A., P. Calderoni, B. Grigolo and G. Gualtieri (2004). "Autologous articular chondrocytes implantation: indications and results in the treatment of articular cartilage lesions of the knee." Chir. Organi. Mov **89**.

Flocco, M. M. and S. L. Mowbray (1995). "Strange Bedfellows: Interactions between Acidic Side-chains in Proteins." J. Mol. Biol. **254**.

Fuqua, J. L., K. Hamorsky, G. Khalsa, N. Matoba and K. E. Palmer (2015). "Bulk production of the antiviral lectin griffithsin." Plant biotechnology journal.

Gaines, W. A. and W. R. Marcotte (2008). "Identification and characterization of multiple Spidroin 1 genes encoding major ampullate silk proteins in *Nephila clavipes*." Insect Molecular Biology **17**(5): 465-474.

Gaines, W. A., M. G. Sehorn and W. R. Marcotte (2010). "Spidroin N-terminal domain promotes a pH-dependent association of silk proteins during self-assembly." The Journal of Biological Chemistry **285**(52): 40745-40753.

Gao, Z., Z. Lin, W. Huang, C. C. Lai, J.-s. S. Fan and D. Yang (2013). "Structural characterization of minor ampullate spidroin domains and their distinct roles in fibroin solubility and fiber formation." PloS One **8**(2).

Gaskett, A. C. (2007). "Spider sex pheromones: emission, reception, structures, and functions." Biological reviews of the Cambridge Philosophical Society **82**(1): 27-48.

Gatesy, J., C. Hayashi, D. Motriuk, J. Woods and R. Lewis (2001). "Extreme diversity, conservation, and convergence of spider silk fibroin sequences." Science (New York, N.Y.) **291**(5513): 2603-2605.

Gellynck, K., P. C. Verdonk, E. Van Nimmen, K. F. Almqvist, T. Gheysens, G. Schoukens, L. Van Langenhove, P. Kiekens, J. Mertens and G. Verbruggen (2008). "Silkworm and spider silk scaffolds for chondrocyte support." Journal of Materials Science. Materials in Medicine **19**(11): 3399-3409.

Goddard, T. K., DG (2015). "Sparky 3." University of California, San Francisco.

Gosline JM, G. P., Ortlepp CS, Savage KN. (1999). "The mechanical design of spider silks: from fibroin sequence to mechanical function." J Exp Biol **202**: 9.

Gronau, G., Z. Qin and M. J. Buehler (2013). "Effect of sodium chloride on the structure and stability of spider silk's N-terminal protein domain." Biomaterials science **1**(3): 276-284.

Hagn, F., L. Eisoldt, J. G. Hardy, C. Vendrely, M. Coles, T. Scheibel and H. Kessler (2010). "A conserved spider silk domain acts as a molecular switch that controls fibre assembly." Nature **465**(7295): 239-242.

Hagn, F., C. Thamm, T. Scheibel and H. Kessler (2011). "pH-Dependent Dimerization and Salt-Dependent Stabilization of the N-terminal Domain of Spider Dragline Silk—Implications for Fiber Formation." Angewandte Chemie International Edition **50**(1): 310-313.

Hedhammar, M., A. Rising, S. Grip, A. S. Martinez, K. Nordling, C. Casals, M. Stark and J. Johansson (2008). "Structural properties of recombinant nonrepetitive and repetitive parts of major ampullate spidroin 1 from *Euprosthenops australis*: implications for fiber formation." Biochemistry **47**(11): 3407-3417.

Hijirida, D. H., K. G. Do, C. Michal, S. Wong, D. Zax and L. W. Jelinski (1996). "^{13}C NMR of *Nephila clavipes* major ampullate silk gland." Biophysical Journal **71**(6): 3442-3447.

Horan, R. L., K. Antle, A. L. Collette, Y. Wang, J. Huang, J. E. Moreau, V. Volloch, D. L. Kaplan and G. H. Altman (2005). "In vitro degradation of silk spidroin." Biomaterials **26**.

Ittah, S., S. Cohen, S. Garty, D. Cohn and U. Gat (2006). "An essential role for the C-terminal domain of a dragline spider silk protein in directing fiber formation." Biomacromolecules **7**(6): 1790-1795.

Ittah, S., A. Michaeli, A. Goldblum and U. Gat (2007). "A model for the structure of the C-terminal domain of dragline spider silk and the role of its conserved cysteine." Biomacromolecules **8**(9): 2768-2773.

Jaudzems, K., G. Askarieh, M. Landreh, K. Nordling, M. Hedhammar, H. Jörnvall, A. Rising, S. D. Knight and J. Johansson (2012). "pH-dependent dimerization of spider silk

N-terminal domain requires relocation of a wedged tryptophan side chain." Journal of Molecular Biology **422**(4): 477-487.

Kenney, J. M., D. Knight, M. J. Wise and F. Vollrath (2002). "Amyloidogenic nature of spider silk." European Journal of Biochemistry / FEBS **269**(16): 4159-4163.

Knight, D. and F. Vollrath (1999). "Hexagonal columnar liquid crystal in the cells secreting spider silk." Tissue & cell **31**(6): 617-620.

Knight, D. and F. Vollrath (2001). "Changes in element composition along the spinning duct in a *Nephila* spider." Naturwissenschaften **88**(4): 179-182.

Krichbaum, J. A. (2016). "Burn Incidence and Treatment in the United States: 2016." Retrieved 5/9/2016, from http://www.ameriburn.org/resources_factsheet.php.

Kronqvist, N., M. Otikovs, V. Chmyrov, G. Chen, M. Andersson, K. Nordling, M. Landreh, M. Sarr, H. Jörnvall, S. Wennmalm, J. Widengren, Q. Meng, A. Rising, D. Otzen, S. D. Knight, K. Jaudzems and J. Johansson (2014). "Sequential pH-driven dimerization and stabilization of the N-terminal domain enables rapid spider silk formation." Nature Communications **5**: 3254.

Kubik, S. (2002). "High-performance fibers from spider silk." Angewandte Chemie (International ed. in English) **41**(15): 2721-2723.

Landreh, M., G. Askarieh, K. Nordling, M. Hedhammar, A. Rising, C. Casals, J. Astorga-Wells, G. Alvelius, S. D. Knight, J. Johansson, H. Jörnvall and T. Bergman (2010). "A pH-dependent dimer lock in spider silk protein." Journal of Molecular Biology **404**(2): 328-336.

Lee, W., W. M. Westler, A. Bahrami, H. R. Eghbalnia and J. L. Markley (2009). "PINE-SPARKY: graphical interface for evaluating automated probabilistic peak assignments in protein NMR spectroscopy." Bioinformatics **25**(16): 2085-2087.

Lefèvre, T., J. Leclerc, J.-F. F. Rioux-Dubé, T. Buffeteau, M.-C. C. Paquin, M.-E. E. Rousseau, I. Cloutier, M. Auger, S. M. M. Gagné, S. Boudreault, C. Cloutier and M. Pézolet (2007). "In situ conformation of spider silk proteins in the intact major ampullate gland and in solution." Biomacromolecules **8**(8): 2342-2344.

Lewis, R. (2006). "Spider Silk: Ancient Ideas for New Biomaterials." Chem. Rev. **106**: 3762-3774.

Li, X., P. T. Eles and C. A. Michal (2009). "Water permeability of spider dragline silk." Biomacromolecules **10**(5): 1270-1275.

Liu, Y., Z. Shao and F. Vollrath (2008). "Elasticity of spider silks." Biomacromolecules **9**(7): 1782-1786.

Liu, Y., A. Sponner, D. Porter and F. Vollrath (2008). "Proline and processing of spider silks." Biomacromolecules **9**(1): 116-121.

Ma, Z., C. Gao, Y. Gong and J. Shen (2005). "Cartilage tissue engineering PLLA scaffold with surface immobilized collagen and basic fibroblast growth factor." Biomaterials **26**(11): 1253-1259.

Madison, K. C. (2003). "Barrier function of the skin: "la raison d'être" of the epidermis." The Journal of Investigative Dermatology **121**(2): 231-241.

Madsen, B., Z. Z. Shao and F. Vollrath (1999). "Variability in the mechanical properties of spider silks on three levels: interspecific, intraspecific and intraindividual." International Journal of Biological Macromolecules **24**(2-3): 301-306.

McCoy, A. J., R. W. Grosse-Kunstleve, P. D. Adams, M. D. Winn, L. C. Storoni and R. J. Read (2007). "Phaser crystallographic software." J Appl Crystallogr **40**(Pt 4): 658-674.

Miller, C., S. Jeftinija and S. Mallapragada (2002). "Synergistic effects of physical and chemical guidance cues on neurite alignment and outgrowth on biodegradable polymer substrates." Tissue Engineering **8**(3): 367-378.

Moran, J. M., D. Pazzano and L. J. Bonassar (2003). "Characterization of polylactic acid-polyglycolic acid composites for cartilage tissue engineering." Tissue Engineering **9**(1): 63-70.

Moura, R., L. Melo and V. de Freitas (2011). "Production of recombinant proteins in milk of transgenic and non-transgenic goats." Brazilian Archives of Biology and Technology **54**(5): 927-938.

Nectow, A. R., K. G. Marra and D. L. Kaplan (2012). "Biomaterials for the development of peripheral nerve guidance conduits." Tissue Eng Part B Rev **18**(1): 40-50.

Newman, J. and C. Newman (1995). "OH WHAT A TANGLED WEB: THE MEDICINAL USES OE SPIDER SILK." International Journal of Dermatology.

Otikovs, M., G. Chen, K. Nordling, M. Landreh, Q. Meng, H. Jörnvall, N. Kronqvist, A. Rising, J. Johansson and K. Jaudzems (2015). "Diversified Structural Basis of a Conserved Molecular Mechanism for pH-Dependent Dimerization in Spider Silk N-Terminal Domains." Chembiochem : A European Journal of Chemical Biology.

Otwinowski, Z. and W. Minor (1997). "Processing of X-ray Diffraction Data Collected in Oscillation Mode." Methods in Enzymology **276**.

Parkhe, A. D., S. K. Seeley, K. Gardner, L. Thompson and R. V. Lewis (1997). "Structural studies of spider silk proteins in the fiber." Journal of Molecular Recognition **10**(1): 1-6.

Parnham, S., W. A. Gaines, B. M. Duggan, W. R. Marcotte and M. Hennig (2011). "NMR assignments of the N-terminal domain of *Nephila clavipes* spidroin 1." Biomolecular NMR assignments **5**(2): 131-133.

Peng, C. A., J. Russo, C. Gravgaard, H. McCartney, W. Gaines and W. R. Marcotte (2016). "Spider silk-like proteins derived from transgenic Nicotiana tabacum." Transgenic Research.

Ries, J., S. Schwarze, C. M. Johnson and H. Neuweiler (2014). "Microsecond folding and domain motions of a spider silk protein structural switch." Journal of the American Chemical Society **136**(49): 17136-17144.

Rising, A., G. Hjälm, W. Engström and J. Johansson (2006). "N-terminal nonrepetitive domain common to dragline, flagelliform, and cylindriform spider silk proteins." Biomacromolecules **7**(11): 3120-3124.

Römer, L. and T. Scheibel (2008). "The elaborate structure of spider silk: structure and function of a natural high performance fiber." Prion **2**(4): 154-161.

Rousseau, M.-E. E., D. Hernández Cruz, M. M. West, A. P. Hitchcock and M. Pézolet (2007). "*Nephila clavipes* spider dragline silk microstructure studied by scanning transmission X-ray microscopy." Journal of the American Chemical Society **129**(13): 3897-3905.

Schrodinger, LLC (2015). The PyMOL Molecular Graphics System, Version 1.8.

Schulz, S. (2001). "Composition of the silk lipids of the spider *Nephila clavipes*." Lipids **36**(6): 637-647.

Schwarze, S., F. U. Zwettler, C. M. Johnson and H. Neuweiler (2013). "The N-terminal domains of spider silk proteins assemble ultrafast and protected from charge screening." Nature Communications **4**: 2815.

Scott, C., S. McCann, R. Gries, G. Khaskin and G. Gries (2015). "N-3-Methylbutanoyl-O-methylpropanoyl-L-serine Methyl Ester - Pheromone Component of Western Black Widow Females." Journal of Chemical Ecology **41**(5): 465-472.

Sen, C. K., G. M. Gordillo, S. Roy, R. Kirsner, L. Lambert, T. K. Hunt, F. Gottrup, G. C. Gurtner and M. T. Longaker (2009). "Human skin wounds: a major and snowballing threat to public health and the economy." Wound Repair Regen **17**(6): 763-771.

Shen, Z. L., A. Berger, R. Hierner, C. Allmeling, E. Ungewickell and G. F. Walter (2001). "A Schwann cell- seeded intrinsic framework and its satisfactory biocompatibility for a bioartificial nerve graft." Microsurgery **21**.

Simmons, A. H., C. A. Michal and L. W. Jelinski (1996). "Molecular orientation and two-component nature of the crystalline fraction of spider dragline silk." Science **271**.

Sponner, A., B. Schlott, F. Vollrath, E. Unger, F. Grosse and K. Weisshart (2005). "Characterization of the protein components of *Nephila clavipes* dragline silk." Biochemistry **44**(12): 4727-4736.

Sponner, A., E. Unger, F. Grosse and K. Weisshart (2004). "Conserved C-termini of Spidroins are secreted by the major ampullate glands and retained in the silk thread." Biomacromolecules **5**(3): 840-845.

Sponner, A., W. Vater, S. Monajembashi, E. Unger, F. Grosse and K. Weisshart (2007). "Composition and hierarchical organisation of a spider silk." PloS One **2**(10).

Sponner, A., W. Vater, W. Rommerskirch, F. Vollrath, E. Unger, F. Grosse and K. Weisshart (2005). "The conserved C-termini contribute to the properties of spider silk fibroins." Biochemical and Biophysical Research Communications **338**(2): 897902.

Stark, M., S. Grip, A. Rising, M. Hedhammar, W. Engström, G. Hjälm and J. Johansson (2007). "Macroscopic fibers self-assembled from recombinant miniature spider silk proteins." Biomacromolecules **8**(5): 1695-1701.

Turnbull, S. (2003). Mongol Warrior 1200-1500. Oxford, Osprey Publishing.

van Beek, J. D., S. Hess, F. Vollrath and B. H. Meier (2002). "The molecular structure of spider dragline silk: folding and orientation of the protein backbone." Proceedings of the National Academy of Sciences of the United States of America **99**(16): 10266-10271.

Vincent, J. F. (1982). "Structural Materials." Macmillan, London.

Vollrath, F. (2000). "Strength and structure of spiders' silks." Journal of Biotechnology **74**(2): 67-83.

Vollrath, F. and D. P. Knight (1999). "Structure and function of the silk production pathway in the spider *Nephila edulis*." International Journal of Biological Macromolecules **24**(2-3): 243-249.

Vollrath, F. and D. P. Knight (2001). "Liquid crystalline spinning of spider silk." Nature **410**(6828): 541-548.

Wallace, J. A. and J. K. Shen (2012). "Unraveling A Trap-and-Trigger Mechanism in the pH-Sensitive Self-Assembly of Spider Silk Proteins." The Journal of Physical Chemistry Letters **3**(5): 658-662.

Wang, S., W. Huang and D. Yang (2014). "Structure and function of C-terminal domain of aciniform spidroin." Biomacromolecules **15**(2): 468-477.

Wendt, H., A. Hillmer, K. Reimers, J. W. Kuhbier, F. Schäfer-Nolte, C. Allmeling, C. Kasper and P. M. Vogt (2011). "Artificial skin--culturing of different skin cell lines for generating an artificial skin substitute on cross-weaved spider silk fibres." PloS One **6**(7).

Winn, M. D., C. C. Ballard, K. D. Cowtan, E. J. Dodson, P. Emsley, P. R. Evans, R. M. Keegan, E. B. Krissinel, A. G. Leslie, A. McCoy, S. J. McNicholas, G. N. Murshudov, N. S. Pannu, E. A. Potterton, H. R. Powell, R. J. Read, A. Vagin and K. S. Wilson (2011). "Overview of the CCP4 suite and current developments." Acta Crystallogr D Biol Crystallogr **67**(Pt 4): 235-242.

Xia, X.-X. X., Z.-G. G. Qian, C. S. Ki, Y. H. Park, D. L. Kaplan and S. Y. Lee (2010). "Native-sized recombinant spider silk protein produced in metabolically engineered *Escherichia coli* results in a strong fiber." Proceedings of the National Academy of Sciences of the United States of America **107**(32): 14059-14063.

Xu, M. and R. V. Lewis (1990). "Structure of a protein superfiber: spider dragline silk." Proceedings of the National Academy of Sciences of the United States of America **87**(18): 7120-7124.

APPENDIX

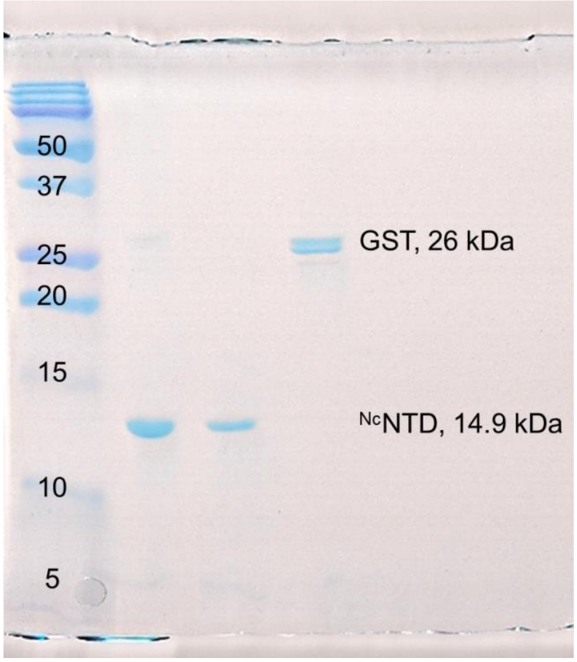

Figure A.1, Purified ^{Nc}NTD. The purity of ^{Nc}NTD samples was checked using SDS PAGE, and the gels were stained with Coomassie Blue staining. The ^{Nc}NTD monomer is 14.9 kDa and the cleaved GST tag is 26 kDa.